Department of Physics and Astronomy
University of Heidelberg

Diploma thesis
in Physics

submitted by
Felix Brezinski
born in Berlin

May 15, 2010

A General Relativistic Model for the Formation of Jets in μQuasars and AGN

This diploma thesis has been carried out by

Felix Brezinski

at the

ZAH, Landessternwarte Heidelberg-Königstuhl

under the supervision of

Prof. Max Camenzind

Statement:

This diploma thesis has been conducted under the supervision of Priv.-Doz. Dr. Ahmad A. Hujeirat at the Landessternwarte-Heidelberg and within the context of the GR-I-RMHD -Project 00.099.2006 funded by the Klaus-Tschira-Stiftung and which is devoted to the development of implicit general relativistic magnetohydrodynamical solvers in multi-dimensions.

Zusammenfassung:

Die vorliegende Arbeit behandelt ein Modell zur Entstehung und Beschleunigung von ultra-relativistischen Jets in der Umgebung rotierender Schwarzer Löcher. Das Modell basiert auf der Kombination von Teillösungen drei verschiedener Bereiche: die innere und äußere Region der Akkretionsscheibe, sowie der darüberliegende Transition Layer. Das ermöglicht die Konstruktion globaler Konfigurationen, die Jets enthalten. Zugrunde gelegt werden Lösungen der zeitunabhängigen, 3D achsensymmetrischen, allgemein-relativistischen, dissipativen und strahlenden Gleichungen der Magnetohydrodynamik. Aufgrund starker Verluste von Rotationsenergie durch magnetische Bremsung kollabiert der Plasmafluss im inneren Bereich der Scheibe dynamisch. Dort strahlt die Scheibe nicht im Röntgen- aber umso stärker im Radiobereich. Die starken Magnetfelder transportieren die Rotationsenergie in eine stark dissipative, dünne Schicht (Transition Layer) zwischen der Akkretionsscheibe und der darüberliegenden Korona. Dort rotiert das Plasma super-keplersch, wird nach außen beschleunigt und erreicht ultra-relativistische Geschwindigkeiten. Da in der unmittelbaren Nähe des Schwarzen Lochs die Zeitskala der Coulomb-Kopplung die dynamische Zeitskala überschreitet, entkoppeln die Protonen und Elektronen thermisch und Zwei-Temperatur-Jets entstehen. Das Modell wird auf den Jet des μQuasars GRS1915+105 angewandt und es stellt sich heraus, dass nur ein sehr schnell rotierendes Schwarzes Loch mit den Beobachtungsdaten verträglich ist.

Abstract:

In this thesis a model for the formation and acceleration of ultra-relativistic jets in the vicinity of rotating black holes is presented. The model is based on matching the solutions of three different regions, namely the outer and inner disk regions together with the overlying transition layer. This enables the construction of global jet-configurations, that rely on the reformulation of the time independent, general relativistic, radiative and dissipative magnetohydrodynamic equations in 3D axisymmetry. The plasma in the innermost region of the disk undergoes a dynamical collapse due to the extensive loss of rotational energy through magnetic breaking, where the disk ceases to radiate in the soft X-ray band, but extensively in the radio band. The strong magnetic fields deposit the rotational energy in a highly dissipative thin layer between the disk and the overlying corona, where the plasma is set to rotate super-Keplerian and starts to accelerate outwards to reach ultra-relativistic speeds. As the dynamical time scale in the vicinity of the black hole is much shorter than the Coulomb one, the protons decouple thermally from the electrons, giving rise to two-temperature jets. When applying the model to the jet in the μQuasar GRS1915+105, it is found that the accreting object must be a rapidly rotating black hole in order to agree with observations.

To Simone in Love

Acknowledgements

I would like to thank my supervisors Priv.-Doz. Dr. Ahmad A. Hujeirat and Prof. Dr. Max Camenzind for guiding me into the regime of general relativistic MHD and for their motivation and many inspiring discussions. I thank Prof. Dr. Matthias Bartelmann who agreed to be my second referee and Ahmad A. Hujeirat and Steffen Brinkmann for tips on how to improve my enunciation.
I wish to thank my parents Enno & Beate for their belief in me and for their culinary and mental support and my grandfather Norbert for supplying me with lots of astronomical journals.
Finally I wish to thank my beloved girlfriend Simone who stood by my side all the time and enriched my life.

Contents

Preface

Astrophysical jets have been observed to emanate from many astronomical systems such as around young stellar objects, in binary systems containing compact objects as well as in active galactic nuclei and quasars. Based on astronomical data and theoretical studies, the formation of jets in such systems is considered to be intimately connected to the accretion phenomena. These data reveal that the very collimated and fast propagating jets are found to emanate from systems containing black holes with some sort of correlation to their mass.
In fact a lot of theoretical effort has been made to explain the jet-disk or jet-black hole connections, while the nature of the interaction between the black hole, jet and disk is still not fully investigated. A conclusive understanding of this interaction would require carrying out full three-dimensional, general relativistic, time-dependent, radiative magnetohydrodynamic calculations of multi-component, dissipative plasmas and using the multi-temperature description, which is beyond the scope of the present thesis. Instead, this work is concerned with the extension of the Newtonian model of Hujeirat et al. (2002, 2003); Hujeirat (2003, 2004) into the general relativistic regime. Such an extension is necessary, since the concerned region of interaction is located in the vicinity of the event horizon, where general relativistic effects are most prominent. Having performed these modifications, the model is readily applicable for studying the formation and acceleration of ultra-relativistic jets in micro-quasars and in active galaxies. In this thesis, a particular attention will be given to the application of the modified model to the μQuasar GRS1915+105. This is a binary system containing an accreting stellar-mass black hole; the first source observed to launch jets with apparent superluminal motion in our galaxy.

The first chapter contains a general introduction to jets in astrophysics. One section is dedicated specifically to GRS1915+105. This object displays a very complicated behavior and will play a major role in the last chapter of this thesis. In the second chapter we give a short review of the standard disk model of Shakura and Sunyaev in its Newtonian formulation. It represents the environment, i.e. the boundary conditions of the inner region where jets are formed. Further, introducing the equations governing accretion flows in the relatively simple Newtonian form will be more convenient for the reader. The whole third

chapter is dedicated to the generalization of these equations to the general relativistic regime.
The fourth chapter is dedicated to the derivation of the new model. First, the equations derived at the end of the previous chapter are specified to the problem of an axisymmetric, time independent flow. Then we are ready to focus on the actual subject of this thesis. First the whole scenario is described qualitatively in order to point out what the model problem is and what assumptions we impose. A long section is dedicated to the quantitative derivation of the model. In the fifth and last chapter we give a discussion of the results we have obtained and of the general properties of the model. Furthermore, we apply the model to the μQuasar GRS1915+105 by fitting it to observational data. This allows for restrictions on the free parameters of the model.

Chapter 1

Introduction

In the first section of this chapter we give a short review of the existing models for jet formation. We point out why the formulation of a new model is necessary. The following section is dedicated to a general introduction of astrophysical jets, including their phenomenology and the basic conclusions about their origin. A specific emphasis is given to the μQuasar GRS1915+105 in the third section, since it will be subject to the application of our model.

1.1 The Necessity for a New Model

The aim of this diploma thesis is to present a model for the formation and acceleration of highly relativistic jets around black holes. The emphasis is on black hole accreting systems, although the model is also applicable to other systems such as accreting neutron stars, white dwarfs or YSO's. Several models for jet formation have been proposed in the past. They capture some partial aspects, while the whole scenario is not well described. Five representatives are discussed here in order to illustrate the problematics that one has to deal with:

The Blandford-Znajek process (BZ-process, 1977): The model describes the formation and acceleration of electron-positron pairs produced in a force-free magnetosphere of a rotating black hole. If poloidal magnetic fields of sufficient strength are generated in an accretion disk surrounding the black hole, the induced poloidal electric fields make the vacuum unstable to cascade pair production. These in turn produce a toroidal magnetic field by induced currents floating along the poloidal magnetic field lines and inside the accretion disk. The escaping particles are accelerated along the field lines and thus extract angular momentum from the disk. If field lines penetrate the event horizon of the black hole, the electric circuit is closed by an effective current floating on the horizon and angular momentum is extracted from the black hole itself. This is possible since a particle can have negative energy in the ergosphere of a rotating black

hole. The BZ-process is most efficient when the poloidal field lines rotate with half of the angular velocity of the horizon. Since the outflow is pair dominated in this model, the mass-loss is very low compared to the accretion rate. However, it has been argued that the contribution of the hole is unlikely to dominate over the contribution of the disk (Livio et al., 1999; Hujeirat, 2004). This is due to the fact that the strength of magnetic fields penetrating the disk should be of the same order as the fields penetrating the horizon while the disk matter is a much better conductor.
The model describes only pair dominated outflows whereas outflows consisting of disk matter would be proton dominated. Therefore the BZ-process only gives a complete picture when there is no contribution from the disk.

The Blandford and Payne model (1982): In this model energy is removed from an accretion disk by means of large-scale, poloidal magnetic fields that penetrate through the disk and extend to large distances. The disk is treated as a Keplerian rotating standard disk (see Section 2.2) and the magnetic field adopts the profile $B \propto r^{-\frac{5}{4}}$. If the angle between the field lines and the disk surfaces is less than 60°, centrifugal forces can drive an outflowing wind along the rigidly rotating field lines. The wind is associated with a magnetic field that is predominantly toroidal at infinity and collimates the outflow into a jet. However, the poloidal field will induce Lorentz-forces in the radial direction, causing the matter to rotate slightly sub-Keplerian. This makes it unlikely that plasma can be ejected by pure centrifugal forces. It has been argued that there is still a potential barrier that can only be overcome if the thermal energy of the plasma is sufficiently high (see Ogilvie and Livio, 2001, and references therein). Last but not least, the accretion disk is assumed to be a standard disk, while magnetic fields are in excess of thermal equipartition. The magnetic fields will likely suppress the generation of turbulence and viscous dissipation, changing the nature of the accretion flow significantly from a standard disk (see Hujeirat et al., 2003).

The X-wind model (Shu et al., 1994): This model is designed to describe the formation of jets around young stellar objects. Stellar magnetic fields are shielded by currents running through the surfaces of the accretion disk except for a small range of radii around the radius r_X, where the disk rotates with the same angular velocity as the star: $\Omega_X = \Omega_*$. For magnetospheres of typical T Tauri stars, r_X is of the order of several stellar radii. Interior to r_X matter is funneled down dynamically along the field lines onto the star. Exterior to r_X the field lines bow outward. Their rigid rotation makes matter attached to them rotate at super-Keplerian velocities (like in the Blandford and Payne model). The mass-loss rate $\dot{M}_w$ can become close to the accretion rate $\dot{M}_d$.
The magnetic fields responsible for the formation of the wind are not generated in the disk but inside the central star. Such a scenario is not applicable to AGN or

μQuasars, since black holes do not possess dynamically stable, poloidal magnetic fields. Further, the magnetic fields are in super-equipartition with the potential energy at r_X and therefore gravitationally unbound. It is therefore likely that they float to the surface of the star on the dynamical time scale (Hujeirat et al., 2003).

Advection-dominated inflow outflow solutions (Blandford and Begelman, 1999, ADIOS,): ADIOS are a special case of ADAF (advection-dominated accretion flows, see e.g. Narayan and Yi, 1995). The basic assumption of ADAF is that the cooling of electrons is ineffective. A large fraction of the energy is stored as entropy in the accreting plasma and advected with the flow. In such a scenario the plasma has positive energy and is potentially unbound. In ADIOS only a small fraction of the inflowing mass is actually accreted and the accretion rate adopts the profile $\dot{M} \propto r^p$, $p \in [0, 1]$. The restriction on p is chosen such that the accretion rate can decrease inwards, while the energy increases.
If there is efficient electron cooling, ADIOS as well as ADAF is not applicable. Since electrons cool very efficiently by synchrotron emission, this rules out the presence of strong magnetic fields. However, relativistic jets are associated with radio emission which is interpreted as synchrotron radiation. This indicates the presence of magnetic fields in the jet plasma. They are believed to play a major role in the collimation of the outflows into jets. Magnetic fields are not treated explicitly in this model but enter only implicitly through the α-parameter (see Shakura and Sunyaev, 1973).
The application of the model to the galactic center shows that ADIOS fits marginally, especially in the radio regime (Yuan et al., 2002). Further, there is the question where the transition between the standard disk and ADAF occurs. At large distance to the center, there is no heating mechanism that could turn the flow to ADAF, i.e. we expect it to be a cold standard disk. In the vicinity of the black hole, on the other hand, ADAF has been found to be thermally unstable (Hujeirat and Camenzind, 2000a).

Truncated disks - advective tori (TDAT Hujeirat and Camenzind, 2000b): This model relies on numerical calculation of radiative hydrodynamics. It investigates the importance of the two-temperature description of accretion flows around black holes. According to this model, the disk truncates close to the marginally stable orbit, where an ion-dominated, advective torus is formed. Thermally-induced, two-temperature outflows occur in a layer, the transition layer, between the disk and the overlying corona. Incorporating large-scale magnetic fields leads to a super-Keplerian rotating, highly diffusive transition layer, where a thermally dominated outflow of magnetized, virial heated ion-electron plasma is launched (Hujeirat et al., 2002). Based on 3D axisymmetric, quasi-stationary magnetohydrodynamic calculations, including magnetic and hydrodynamic diffusion, Hujeirat et al. (2002) have found that: 1.) The angular velocity in the transition layer adopts the profile $\Omega \propto r^{-\frac{5}{4}}$. 2.) Ions cool predominantly in fast outflows by adiabatic cooling. 3.) The generated toroidal field partially heats the transition layer by reconnection, while another part is advected with the outflow. An outflow rate of about 5% of the accretion rate has been obtained.

The model proposed in this diploma thesis is based on the models of Hujeirat et al. (2002, 2003) and Hujeirat (2003, 2004) which base on and are a further development of TDAT. It shares the main features (points 1-3) of TDAT, including a two-temperature description of the outflowing wind. Magnetic fields are explicitly taken into account. It gives a precise, analytic description of the processes that lead to the formation of the transition layer. This is achieved by solving the general relativistic, stationary and axisymmetric magnetohydrodynamic equations. The transition between the model and the SSD, governing the exterior, occurs at the radius r_{tr}. r_{tr} is taken to be the point where large-scale, poloidal magnetic fields are in equipartition with the thermal energy. The formation of strong, large-scale magnetic fields from weak, microscopic fields is a consequence of the interplay of the magnetorotational- and Parker instability in combination with reconnection and inwards motion due to accretion (Hujeirat et al., 2003).

1.2 Jets in Astrophysics

In astrophysics the term jet applies to collimated, roughly cone-shaped flows of hot plasma. Curtis (1918) discovered the first source to eject a jet. It was the giant elliptical galaxy M87 in the center of the virgo cluster (Fig. 1.1). At first this seemed to be extraordinary, but nowadays jets are found to be associated with a wide variety of astrophysical objects. First, there are active galactic nuclei (AGN) like quasars, radio galaxies, Seyfert-galaxies, blazars, etc... These systems contain super-massive black holes and the processes at work are most violent. However, jets are also found around young stellar objects (YSO), i.e. T-Tauri-stars (associated with Herbig-Haro-objects) and in stellar-mass binary systems, containing compact objects like white dwarfs, neutron stars or stellar black holes. In the latter case, the primary objects accrete mass from their companions or from the surrounding medium (like in planetary nebulae). Examples for these systems are super soft X-ray sources, low mass X-ray binaries, black hole X-ray transients, etc...
It is generally considered that ejections of winds or collimated jets are connected to accretion phenomena. This connection is supported by the observational fact that most stellar systems, launching jets, also feature an accretion disk (see Livio, 1999, and references therein).
YSO's are a good example for this connection, since a protostar is usually surrounded by an accretion disk, consisting of dust. The inflow of mass is ac-

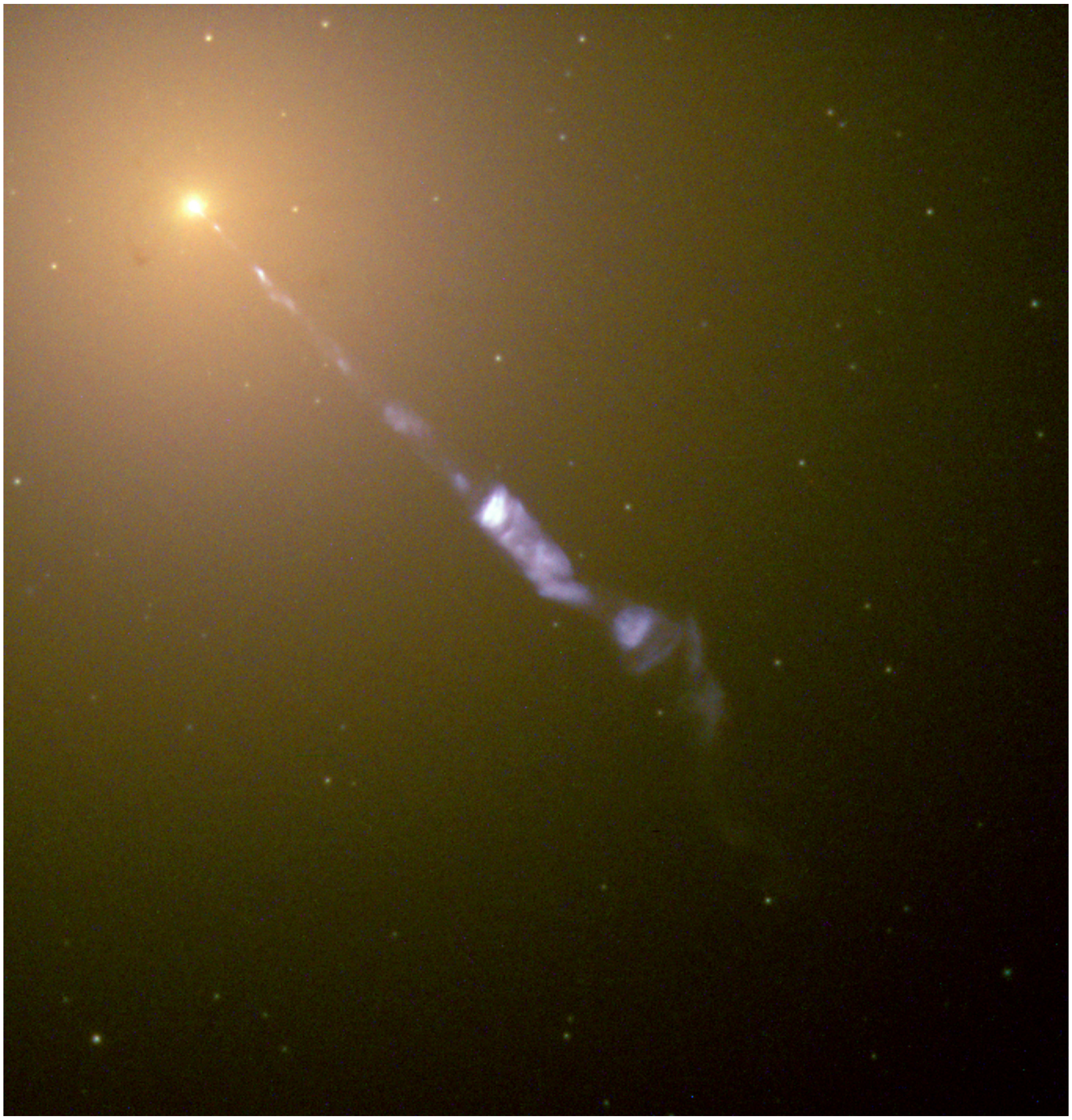

Figure 1.1: The optical jet of the giant elliptical galaxy M87

Credit: NASA and The Hubble Heritage Team (STScI/AURA)

companied with an outflowing, bipolar, cone-shaped wind that emanates perpendicular to the disk plane. The mass-loss rate due to the wind ranges from $10^{-8} - 10^{-5} M_{\odot} yr^{-1}$, where $M_{\odot}$ is the solar mass. There are weakly collimated, slow winds ($< 20\, km\, s^{-1}$) and strongly collimated, fast winds ($100 - 300\, km\, s^{-1}$), containing mass in the range of $10^{-2} - 10^{2} M_{\odot}$. Observations clearly show that these winds are formed in the inner region of the accretion disk (Fig. 1.2, see also Burrows et al. (1996)). They extend up to several parsecs and permeate the interstellar medium at supersonic velocities. At the terminal points, where the

jets end, hot spots are created: bright emission regions that are due to ionisation by shock-waves. The structure of these jets is clumpy, indicating instabilities in the outflowing plasma and irregularities in the ejection of mass.
The connection between accretion and jet formation is not so clear in the case of AGN, though, but the presence of accretion disks is still very likely. The underlying processes become much more violent in systems, containing compact objects. Their jets propagate with highly relativistic velocities and extend up to the parsec scale (X-ray binaries) or kiloparsec scale (AGN), thereby maintaining collimation. The jet of the radio galaxy NGC 6251, for example, maintains linear collimation up to $1\,Mpc$, indicating that the underlying mechanisms work effectively for the duration of $1-10\,Myr$.
The energetics associated with these phenomena are among the most powerful in the universe: A typical Seyfert galaxy has a bolometric luminosity of $10^{11}-5\cdot 10^{12}L_\odot$ while quasars even have $\geq 10^{13}L_\odot$, where $L_\odot$ is the solar luminosity (see e.g. Robson, 1996; Woo and Urry, 2002), making quasars the brightest systems in the universe.
This raises the question how this energy is generated. The gravitational energy released in an accretion flow onto a supermassive black hole appears to be the most likely source of energy. A particle at the radial distance r from an object of mass M has the potential energy per mass:

$$E_{pot} = -\frac{GM}{r}, \tag{1.1}$$

where G is Newton's constant. This amount of energy may be liberated in the form of radiation. The luminosity L associated with an accretion flow scales as:

$$L = \frac{GM\dot{M}}{r_{in}} = \eta \dot{M} c^2 \quad , \quad \eta = \frac{GM}{c^2 r_{in}}, \tag{1.2}$$

where $\dot{M}, c, \eta$ are the accretion rate, the speed of light and the accretion efficiency, respectively. η is a measure of how much gravitational energy is released. r_{in} is the minimal radius of emission from the accretion flow. For YSO's, white dwarfs and neutron stars this might be the stellar radius. For particles orbiting a black hole it is the radius of marginal stability r_{ms}. Interior to r_{ms} particles would very rapidly fall into hole without being able to distribute or radiate their energy. The maximal efficiency equals 0.08 for a Schwarzschild black hole and ranges from 0.06 to 0.42 for a Kerr black hole[1]. The accretion luminosity causes an outward oriented radiation pressure due to the liberated gravitational energy. For stationary flows, the radiation pressure can not exceed the gravitational pull of the central object. This sets an upper limit for the accretion rate, the Eddington

[1] These two values correspond to a maximally rotating black hole in the case that the matter is in counter-rotation or co-rotation, respectively.

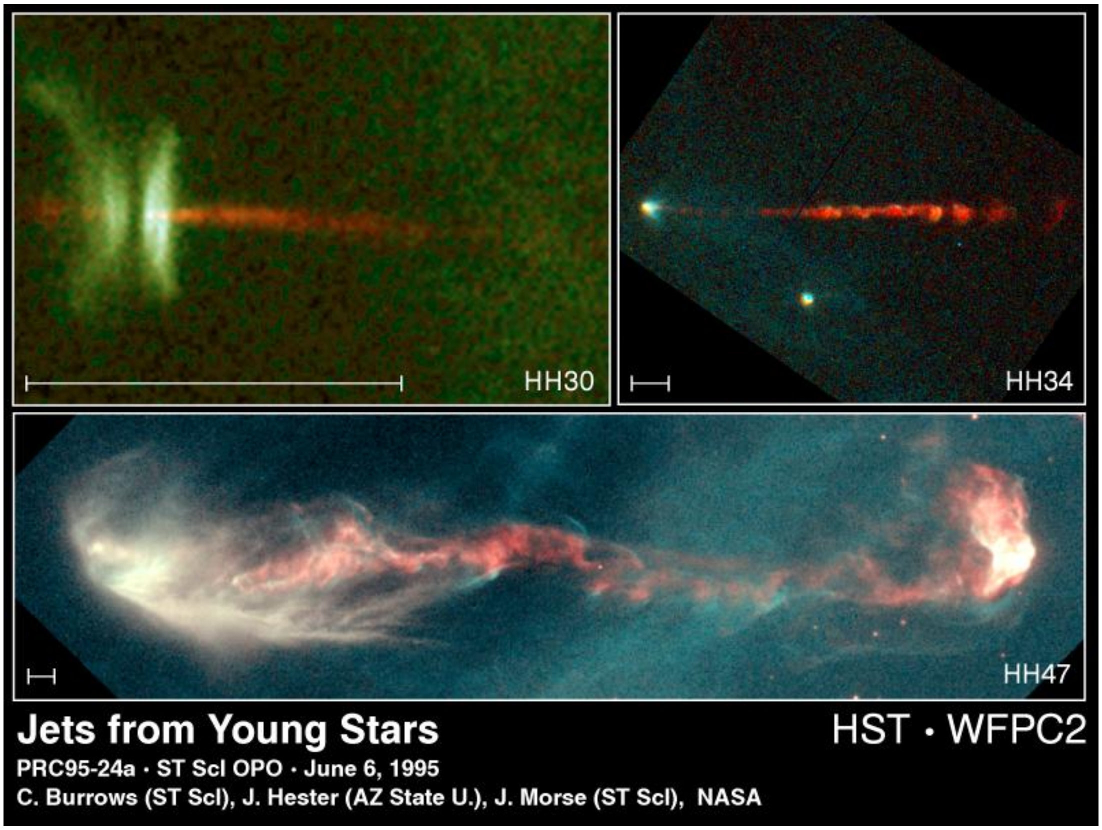

Figure 1.2: A collection of observations of Herbig-Haro objects

Upper Left Credit: C. Burrows (STScI & ESA), the WFPC 2 Investigation Definition Team, and NASA
Upper Right Credit: J. Hester (Arizona State University), the WFPC 2 Investigation Definition Team, and NASA
Bottom Credit: J. Morse/STScI, and NASA

limit. The corresponding luminosity is called the Eddington luminosity (see e.g. Camenzind, 2007):

$$L_{Edd} = \frac{4\pi G M m_p c}{\sigma_T} = 3.26 \cdot 10^4 \cdot L_\odot \frac{M}{M_\odot} = 1.26 \cdot 10^{38} erg\, s^{-1} \cdot \frac{M}{M_\odot}, \qquad (1.3)$$

where m_p and σ_T stand for the proton mass and the Thomson cross section, respectively. One should note that this is only a strict limit in the case of stationary, one dimensional flows. We can now estimate the accretion rate, necessary to produce the typical luminosities of Seyfert galaxies and quasars. For a rough estimate we use $\eta = 0.1$ and obtain:

$$\begin{array}{lll} \dot{M} \approx 4 \cdot 10^{24} g\, s^{-1} & \text{or} \quad \leq 0.1 M_\odot yr^{-1} & \text{for Seyfert galaxies,} \\ \dot{M} \geq 4 \cdot 10^{26} g\, s^{-1} & \text{or} \quad \geq 10 M_\odot yr^{-1} & \text{for quasars.} \end{array} \qquad (1.4)$$

Systems	v_{jet}	radius where $v_{jet} = v_{esc}$	Example
YSO	$200\,km\,s^{-1}$	$\approx 10\,R_\odot\,M/M_\odot$	HH30/34
SSXS	$3800\,km\,s^{-1}$	$\approx 3\,R_E\,M/M_\odot$	RXJ0513.9-6951
LMXB	$0.26\,c$	$\approx 30\,r_g$	SS433
BHXT	$0.9\,c$	$\approx 2.5\,r_g$	GRS1915+105
AGN	$\gamma \geq 3$	$\leq 2.25\,r_g$	M87

Table 1.1: Comparison between jet velocity and escape velocity

The radius where $v_{jet} = v_{esc}$ is expressed in typical units. These are solar radii $R_\odot$ for YSO's, earth radii R_E for SSXS (super soft X-ray sources, i.e. accreting white dwarfs) and gravitational radii r_g for LMXB (low mass X-ray binaries, i.e. accreting neutron stars), BHXT (black hole X-ray transients) and AGN. The gravitational radius r_g is given by $r_g = GM/c^2$.

We see that the accretion process can provide the necessary amount of energy to produce the observed luminosities.

Jets are expected to play a major role in the transport of energy and angular momentum from the accretion disk. In order to become so energetic, they have to be formed deep inside the potential well, in the immediate the vicinity of the central object. This is in fact supported by observation in cases where the central region is accessible (e.g. YSO's, see above). In the case of AGN and stellar mass X-ray binaries, one can rely on multi-wavelength observations. Another support is given by the fact that jet velocities are of the order of the escape velocity in the vicinity of the central object (see Table 1.1).

We will now further concentrate on jets from systems that contain compact objects. Jet-launching X-ray binaries are called μQuasars, since they share three important features with the original quasars: a compact object in its center, an accretion disk, the ejection of relativistic blobs and/or jets. The "μ" in μQuasars points to the fact that the compact objects in these systems usually have masses $M = O(1) - O(10)M_\odot$ while the super-massive black holes in quasars have $M = O(10^6) - O(10^9)M_\odot$. Simple scales of length and time are proportional to the mass of the compact object. Hence, processes that operate in quasars over several $10^3 yr$, say, operate over several days in the case of μQuasars. This makes them the ideal laboratory for the study of quasars, aside from the fact that they are already very interesting by themselves. The similarities in these systems, AGN and μQuasars, suggests that the physics of accretion onto black holes is the same over a large range of scales and that there is an underlying unity in the process of accretion and jet formation.

The jets of AGN and μQuasars feature relativistic effects namely apparent superluminal motion and relativistic beaming. Let us take a look at how this works: Let $S(\nu)$ be the frequency dependent flux density as measured in the comoving frame of the source. An observer moving with relative velocity parameter $\vec{\beta} = \vec{v}/c$

measures the flux density:

$$S_{ob}(\nu) = S(\nu) D(\beta,\theta)^{3+\alpha}, \tag{1.5}$$

$$D(\beta,\theta) = \frac{1}{\gamma\,(1-\beta\cos\theta)}, \tag{1.6}$$

where $\gamma = (1-\beta^2)^{-\frac{1}{2}}$ is the Lorentz factor, D the Doppler factor and θ the angle between the line of sight and the velocity of the observer. $\alpha = -d\ln S/d\ln\nu$ is the spectral index (see Blandford and Konigl, 1979). Hence, the intensity of measured flux depends on the angle enclosed with the line of sight. (1.6) achieves a maximum at $\theta = 0$ and a minimum at $\theta = \pi$. Thus the intensity is strongly amplified for the approaching and weakened for the receding component. This becomes more and more dramatic the closer β approaches 1. Writing $1-\beta = \delta \ll 1$, we obtain from (1.5):

$$\frac{1}{\gamma\,(1-\beta\cos\theta)} = \left\{ \begin{array}{ccc} \sqrt{2}/\delta & \gg 1 & , \quad \theta = 0 \\ \sqrt{2\delta} & \ll 1 & , \quad \theta = \pi/2 \\ \sqrt{\delta}/2 & \ll 1 & , \quad \theta = \pi \end{array} \right. . \tag{1.7}$$

Indeed in many cases relativistic ejecta are only detected on one side of the source. Theory, on the other hand, usually assumes symmetric systems that launch bipolar jets, propagating along the axis of rotation in opposite directions.

Of course, there is the possibility that there are some processes at work in the system that break symmetry and prefer one side. However, one usually explains the missing of the second jet by relativistic beaming. This interpretation is supported by the fact that measured brightness temperatures of jet plasma occasionally exceed $10^{12}K$. This clearly indicates relativistic beaming, since the plasma would rapidly cool via inverse Compton scattering at such temperatures.
Another relativistic effect occurring in astrophysical jets is apparent superluminal motion. Due to the finite velocity of light the observer moving relative to the source measures the velocity

$$\vec{\beta}_{ob} = \frac{\vec{n} \times \left(\vec{\beta} \times \vec{n}\right)}{1-\vec{\beta}\vec{n}} = \frac{\vec{\beta} - \vec{n}\beta\cos\theta}{1-\beta\cos\theta}, \tag{1.8}$$

where $\vec{n}$ is the tangent-vector to the line of sight (Blandford and Konigl, 1979). Hence, the magnitude of the observed velocity is equal to

$$\beta_{ob}(\theta) = \frac{\beta\sin\theta}{1-\vec{\beta}\cos\theta}. \tag{1.9}$$

This expression peaks at $\cos\theta = \beta$. Hence, we have:

$$\beta_{ob}(\arccos\beta) = \frac{\beta}{\sqrt{1-\beta^2}} \geq 1 \quad \text{for} \quad \beta \geq \frac{1}{\sqrt{2}}. \tag{1.10}$$

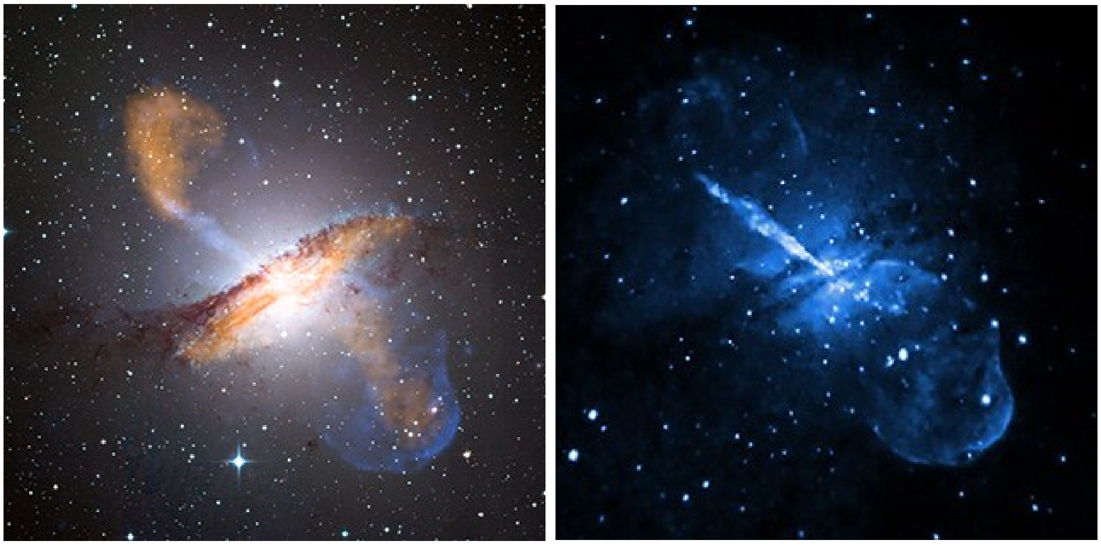

Figure 1.3: The radio galaxy Centaurus A

The left image shows Centaurus A in visible light (dust in the galactic plane and background stars), submillimeter wavelengths (orange color) and X-rays (blue color). The right image, which is purely in X-rays, displays a clean one-sided jet (the thin blue strip) emanating from the upper side. It propagates with $\approx 0.5\,c$ and extends over $\approx 4\,kpc$. It is visible in X-rays and radio-waves. There is a cloud like double structure on both sides of the galaxy emitting in the submillimeter regime. This feature occurs in most radio galaxies and is not to be confused with the actual jets. The clouds and the jet are a little bit bent. This might be due to perturbations from neighboring galaxies or the precession of the axis of rotation.
Credit: X-ray: NASA/CXC/CfA/R.Kraft et al.; Submillimeter: MPIfR/ESO/APEX/A.Weiss et al.; Optical: ESO/WFI

Thus jet plasma propagating at velocities $\geq 0.707\,c$ may appear superluminal. An example is the jet of the quasar 3C273 (Fig. 1.4).
Jets are associated with the emission of radio waves up to X-rays and γ-rays. The radiation is linearly polarized and their spectrum is nonthermal, obeying a power law:

$$S(\nu) \propto \nu^{-\alpha} \tag{1.11}$$

This is generally interpreted as synchrotron radiation from relativistic electrons and hints to the existence of magnetic fields in the jet plasma. Radiated power via synchrotron emission is of the order $10^{45} erg\, s^{-1}$ for AGN (Robson, 1996). The spectral index α usually adopts values from 0 to 1. The X-ray and γ-ray spectrum is also nonthermal and probably due to inverse Compton scattering of soft photons with relativistic electrons.
According to (C.4) a relativistic electron ($v \approx c$) moving in a magnetic field of

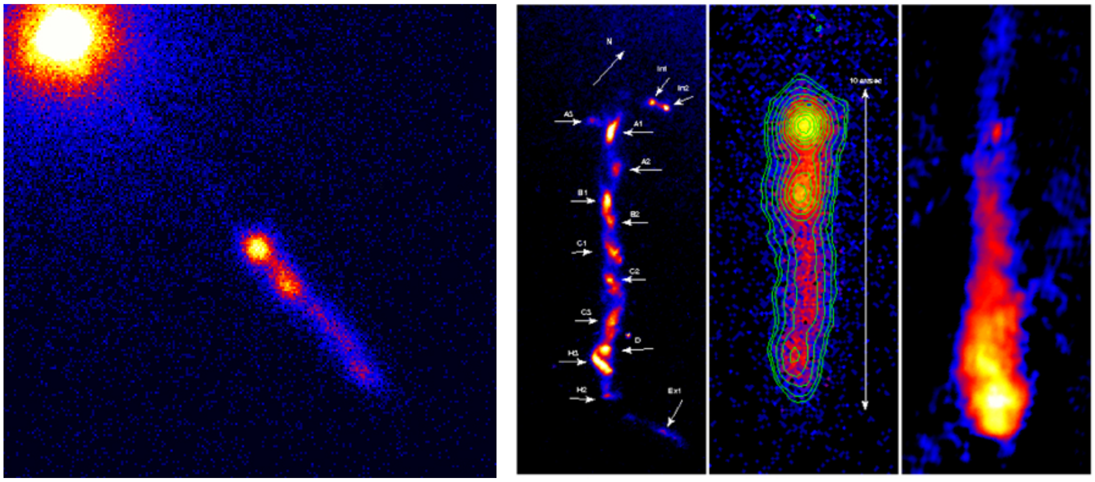

Figure 1.4: The quasar 3C273

The left panel shows the quasar 3C273 in X-rays. It was the first quasar to be discovered (1963).
Credit: NASA/CXC/SAO/H.Marshall et al.
The right panel shows close ups of the jet. The images are optical (left,HST), X-ray (middle,Chandra), and radio (right,MERLIN).
Credit: Optical: NASA/STScI X-ray: NASA/CXC Radio: MERLIN

strength B, perpendicular to its velocity, radiates with power:

$$-\frac{dE}{dt} \approx 1.6 \cdot 10^{-7} erg\, s^{-1} \cdot \gamma^2 B^2. \tag{1.12}$$

Hence, the time scale to radiate this energy is:

$$t_{sync} = \frac{E}{-dE/dt} \approx 5.2\, s \cdot \gamma^{-1} B^{-2}. \tag{1.13}$$

Regarding that a synchrotron source of electrons with energy $E = \gamma m_e c^2$ must satisfy $E = L t_{sync}$, we find that the minimal energy content is obtained when the magnetic energy is approximately in equipartition with the relativistic particle energy (see Frank et al., 1992, page 221). Polarisation measurements can also reveal the direction of the magnetic field. Near the origin of the jet, the field is predominantly parallel to its axis, while it becomes orthogonal at larger distances.

There is no consensus about the details of the formation, acceleration and collimation of jets. Yet, synchrotron emission is a clear sign of the importance of magnetic fields in the underlying mechanisms.
The model presented in this diploma thesis is based on the existence of strong, large-scale, poloidal magnetic fields in the vicinity of the central object. These

fields rapidly extract angular momentum from the disk thus powering a centrifugally driven wind. The collimation of the wind happens on much larger scales by means of advected, toroidal magnetic fields. However, the subject of this model is only the immediate vicinity of the central object where the formation of the jet takes place.

1.3 The μQuasar GRS1915+105

We will now introduce the X-ray source GRS1915+105. It is a typical μQuasar on one side but it also displays some exceptional features rendering it hard, but all the more interesting to interpret its behavior. In the last chapter we will apply our model to this exotic system. Thus, a whole section is dedicated to it, so the reader becomes familiar with its properties.

GRS1915+105 was discovered in 1992 by the X-ray probe GRANAT. It was the first galactic source discovered to launch jets of apparent superluminal speeds (Greiner et al., 1996a). GRS1915+105 is an X-ray binary system containing a compact component, namely a stellar mass black hole, and a main sequence star of spectral type K-M and luminosity class III (giant) that transfers mass to the black hole. GRS1915+105 has an orbital period of $33.5\,d$ and its velocity curve peaks at $145 \pm 15\,km\,s^{-1}$. Its distance from earth is estimated to $11 - 13\,kpc$ (Greiner, 2001). The system parameters indicate accretion via Roche-lobe overflow. Based on the observations of RXTE on 1996 June 19, September 27 and

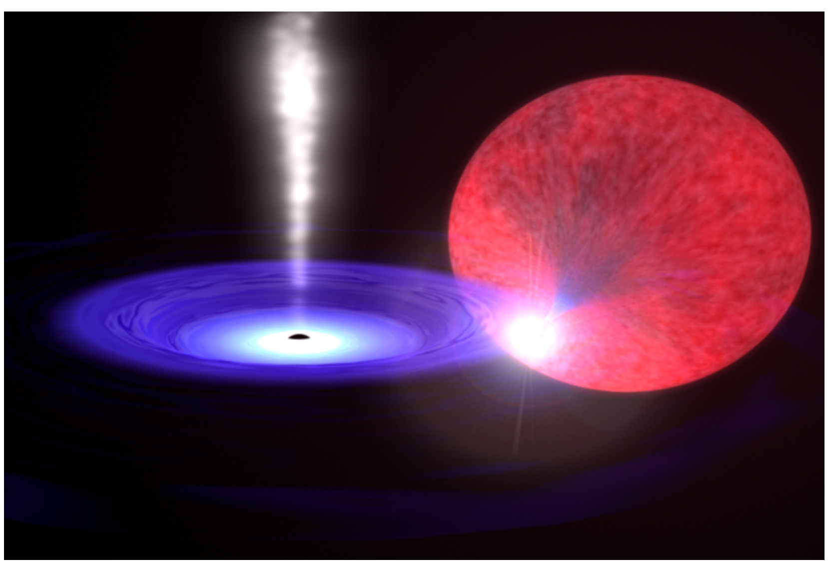

Figure 1.5: Still from an animation of GRS1915+105

Credit: NASA/CXC/A.Hobart

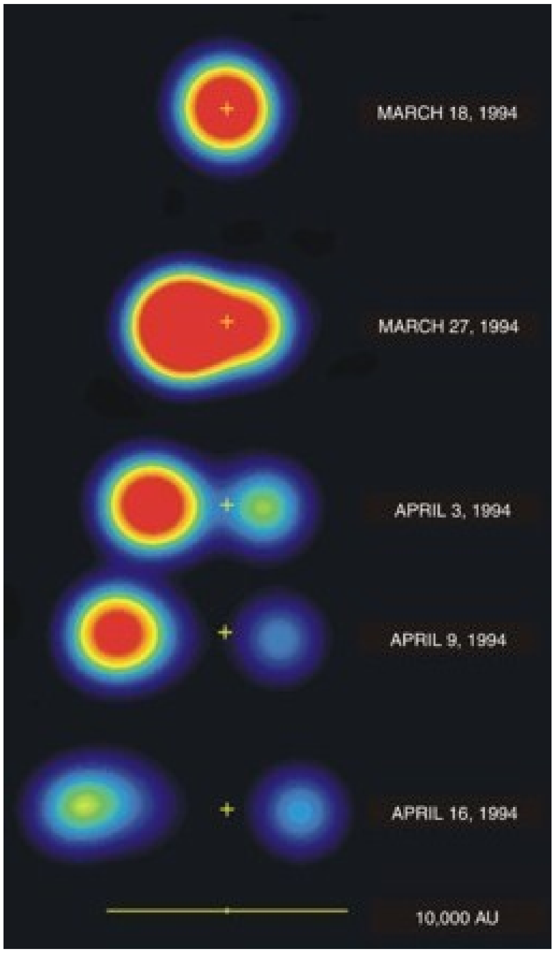

Figure 1.6: The ejection event in GRS1915+105 on 1996 March 19

This sequence of VLA images shows the propagation of two blobs of plasma, that were ejected in the outburst on 1994 March 19. The cross marks the position of GRS1915+105.
Credit: National Radio Astronomy Observatory / Associated Universities, Inc. / National Science Foundation

October 1 to 29, Belloni et al. (1997a) have estimated the accretion rate of GRS 1915+105 to $\dot{M} \approx 1.7 \cdot 10^{-8} M_{\odot} yr^{-1}$ during quiescence, for an extreme Kerr black hole. During outbursts the accretion rate is higher by a factor of 2 and variable (the terms "quiescence" and "outburst" are explained in the text below). For comparison: the Eddington accretion rate for an object of $14\,M_{\odot}$ is approximately $\dot{M}_{Edd} \approx L_{Edd}/c^2 = 3.1 \cdot 10^{-8} M_{\odot} yr^{-1}$. This is different from usual stellar black hole systems which accrete at a much lower rate, e.g. GRO J1655-40 with $\dot{M}/\dot{M}_{Edd} \approx 0.1 - 0.2$.
The system launches relativistic blobs and steady jets of plasma in a quasi periodic cycle of 20-30 days that propagate at an apparent velocity of $0.65 - 1.25\,c$ (like in the outburst on 1994 March 19, see Mirabel and Rodríguez (1994)). This corresponds to propagation with $0.92\,c$ under an inclination angle of $\theta \approx 70° \pm 2°$ to the line of sight, whereas the ejection angle changes within about 10° between different events (Mirabel and Rodríguez, 1999). Observations with MERLIN in 1997 and VLBA in 1998 detected speeds of $1.3 - 1.7\,c$ (Fender et al., 1999; Dhawan et al., 2000), corresponding to $0.98\,c$ and $\theta \approx 66°$. However, it is not clear whether this result is due to changes in the inclination angle, resolution effects or actual, faster intrinsic motion. The observations with VLBA show that the jets are already collimated on scales of $\approx 10\,AU$.

They have a stable axis at scales $\geq 500 - 1000\,AU$ over four years (Mirabel and Rodríguez, 1999; Dhawan et al., 2000).
If assumed to consist of equal numbers of electrons and protons, clouds of minimum mass $10^{19} g$ are ejected every few $10\,min$ during these events. However, the total mass expelled in such a cycle is $\approx 10^{21} g$ (Belloni et al., 1997a; Mirabel

et al., 1998). Additionally, the luminosity due to synchrotron emission has to be at least $10^{36} erg\, s^{-1}$ (comparable to the thermal X-ray luminosity, Sams et al. (1996)). Rodríguez and Mirabel (1999) have made some estimates on the mass and energy of the ejecta of the 1994 March 19 event (VLA images depicted in Fig. 1.6). They obtained a magnetic field strength of $5 \cdot 10^{-2} G$, an energy of about $4 \cdot 10^{43} erg$ in relativistic electrons and a total ejected mass of the order $10^{23} g$, assuming equal numbers of electrons and protons in the ejecta. The ejection event lasted for ≤ 3 days. Thus, a minimum power of $5 \cdot 10^{38} erg\, s^{-1}$ is required. This is comparable with the maximum observed, steady luminosity $\approx 3 \cdot 10^{38} erg\, s^{-1}$ (Mirabel and Rodríguez, 1994; Harmon et al., 1994). All this allows for the crude estimate that GRS1915+105 ejects mass of the order $10^{23} g\, yr^{-1}$ in the form of relativistic $(0.92 - 0.98\, c)$, collimated outflows corresponding to a power output of $10^3 L_\odot$ (Mirabel and Rodríguez, 1999).
The measurement of the inclination angle makes it possible to estimate the mass of the compact component to $14 \pm 4\, M_\odot$. Thus, GRS1915+105 harbors the most massive stellar black hole, so far discovered in the milky way. It might even be more massive, since the donor's mass might be underestimated to due to modifications of the light curve by loss of mass (Greiner, 2001).
Systems containing stellar mass black holes often have different states of intensity and spectral distribution. There are high intensity states with a strong thermal component and a soft X-ray component that is described by a steeply falling power law. These are the high/soft or outburst states. Then there are low/hard or quiescent states with low intensity, negligible thermal contribution and a flat power law component. GRS1915+105 also displays flaring states with rapid oscillations between the high/soft and the low/hard state. Its intensity and spectrum display strong variations. The luminosity ranges from $10^{38} erg\, s^{-1}$ during quiescence (Rau and Greiner, 2003) to $10^{39} erg\, s^{-1}$ in the $1 - 25\, keV$ range during outbursts (Greiner et al., 1996a). Thus GRS1915+105 is the most energetic object in the milky way.
The spectrum has a thermal component that is interpreted as an accretion disk and a power law component that is considered to be connected to jet formation. The power law index assumes values in the range 2.3-3.9. Around $6\, keV$ one also has to include an iron line plus absorption edge when fitting the spectrum (Belloni et al., 1997a).
An accretion disk surrounding a black hole is unstable interior to r_{ms}, the radius of marginal stability. r_{ms}, on the other hand, is a decreasing function of the black hole spin. Hence, a disk surrounding a rotating black hole achieves higher temperatures since its inner boundary is closer to the event horizon. In GRS1915+105 the temperature of the disk component switches between two values at the inner edge, one constant and one more variable. The higher value indicates an inner radius of $\approx 20\, km$ $(2.2\, keV)$ and the lower $50 - 90\, km$ $(\approx 1\, keV)$, respectively (see Belloni et al., 1997a,b). In any case the inner radius was observed to be below $\approx 300\, km$.

Such a low value for the minimal inner radius of the accretion disk leads to the assumption that the compact component of GRS1915+105 is very rapidly rotating, since $r_{ms} = 20.7\,km$ for a $14\,M_{\odot}$ black hole in maximal rotation. However, it should be noted that $r_{ms} = 25.4\,km$ for $M = 14\,M_{\odot}$ and $a = 0.9982$, which is the maximum spin of an accreting black hole (see Thorne, 1974). This means that the black hole in GRS1915+105 is either spinning with $a > 0.9982$ or has mass $M < 14\,M_{\odot}$. Together with GRO J1655-40 it is the only galactic source that is believed to contain a maximally rotating black hole (Belloni et al., 1997a; Morgan et al., 1997; Zhang et al., 1997).

Belloni et al. (2000) have analyzed the observations of GRS1915+105, performed by RXTE between January 1996 and December 1997. They divided the spectrum into three energy intervals:

$$\begin{aligned} "0" &: \; 2 - 5\,keV \\ "1" &: \; 5 - 13\,keV \\ "2" &: \; 13 - 60\,keV. \end{aligned} \tag{1.14}$$

Then they defined the hardness ratios:

$$HR_1 = \frac{"1"}{"0"} \quad \text{and} \quad HR_2 = \frac{"2"}{"0"}. \tag{1.15}$$

Based on count rate and hardness ratios the variability of the source could be separated into twelve classes. Fitting the data with a sum of black-body and power law spectrum they identified three basic states A,B and C, defined as (sect. 3.3 of Belloni et al., 2000):

- A: low rate, low HR_1 and HR_2
- B: high rate, high HR_1
- C: low rate, low HR_1, variable HR_2 depending of the length of the interval

State A is dominated by the disk component and shows little variability. State B is the typical high/soft state of black hole transients with a strong accretion disk component reaching down to the innermost stable orbit. In the state C, the power law component is strong while the disk component is very weak. The system does not switch between these states at random. There are periods where the source is in state A and also long periods (about 40-50% of the time) where it remains in state C only, indicating that the system is in equilibrium in these states. Then there are phases where the system oscillates between the states C and A or between states B and A. Additionally there are quasiperiodic sequences where the sources follows the pattern B-C-A-B. The behavior is described in much more detail in Belloni et al. (2000). Fig. 1.7 shows a schematic sketch of the position of these states in the hardness ratio-diagram and the observed

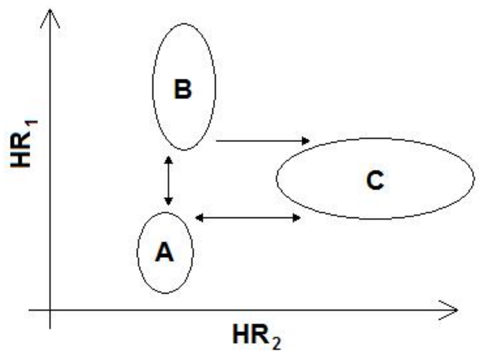

Figure 1.7: The three basic states of intensity/spectrum of GRS1915+105

A schematic illustration that shows the three basic states of GRS1915+105 and the transitions between them in a hardness ratio-diagram. For further information see Belloni et al. (2000).

transitions between them. Various quasi periodic oscillations of the light curve are observed with frequencies ranging from $10^{-3} - 67Hz$ (Greiner et al., 1996b). In the range from $1 - 15\,Hz$ they are correlated to the inner disk radius and are clearly connected to state C. Belloni et al. (2000) propose a model where the inner part of the accretion disk is removed during state C and, at least partially, channeled into an outflowing wind or jet. However, it can be shown that such a configuration can not be stationary, contradictious to the system appearing to be in an equilibrium during state C (Papaloizou and Pringle, 1985).
Jet ejection is associated with radio and X-ray emission. The ejection of relativistic blobs and jets is preceded by unusual activities in X-rays, but not all unusual X-ray activity is followed by an ejection. Yet, there is a positive correlation between the radio emission and the power law slope. Also there is a positive correlation between the radio flux and the X-ray flux: Large amplitude variations within seconds in the X-ray spectrum are accompanied with variations at minute-scale in radio (see Mirabel and Rodríguez, 1999; Rau and Greiner, 2003). Furthermore, superluminal blobs of radio emitting material are ejected when the system is passing over from a quiescent to a flaring phase (Mirabel et al., 1998). All this leads to the conclusion that there is steady jet emission during state C and abrupt emission during the "A/C"-oscillations and the "B-A-C-B"-cycle.
Livio et al. (2003) propose a model where small scale magnetic fields are generated in the accretion disk by a dynamo process during states A/B. Energy liberated by viscous dissipation is locally radiated away in the accretion disk and in the corona. In state C, however, a global poloidal magnetic field has formed in the inner part of the disk. The energy in this region is then released in the form of a magnetically driven jet or wind. Thus the disk appears to be truncated since it does not radiate locally. The jet power is supposed to be a substantial fraction of the accretion luminosity.
Indeed the model of Livio et al. (2003) is based on the models of Hujeirat et al. (2002, 2003); Hujeirat (2003, 2004) which are the subject of this thesis. In the latter it is assumed that small scale magnetic fields are amplified by the magneto-rotational instability (see Balbus and Hawley, 1991). Magnetic flux tubes recon-

nect and subsequently form a large-scale poloidal magnetic field in the inner region of the disk. The field suppresses the generation of turbulence and rapidly extracts angular momentum from the disk matter. This process creates a strong toroidal field in a geometrically thin layer above the disk where the matter is forced to rotate with super-Keplerian velocities. The jet is then driven by centrifugal acceleration of the matter in this layer while a large part of the toroidal field is advected outwards.

Chapter 2

Magnetohydrodynamics and the Standard Disk

In order to study jet formation in accretion flows onto compact objects we have to go to the innermost boundary layer of the accretion disk. We will have to deal with a lot of difficulties there. They arise from the complicated dynamics of the flow which includes the action of magnetic fields. Furthermore, general relativistic effects due to the geometry of spacetime are of great importance in the vicinity of a compact object. It will be useful, however, to introduce the governing equations in the Newtonian regime first. This way the equations will be much simpler and their overall structure will already be familiar when we proceed to the general relativistic regime.
The second goal of this chapter is to introduce the standard disk model of Shakura and Sunyaev (1973). It describes the nature of the accretion flow at sufficiently large distance to the center and sets the boundary conditions for the flow in the inner region. Novikov and Thorne (1973) have derived a general relativistic version of the standard disk model. However, we want to introduce just the basic ideas and the general properties of the standard disk so it will suffice to describe the accretion flow by means of the Newtonian theory of gravity.
Thereafter, we are ready to proceed to the general relativistic regime and subsequently derive the model that is the subject of this diploma thesis.

2.1 The Magnetohydrodynamic Equations

The description of an accretion flow around a compact object is a problem that falls in the domain hydrodynamics. In hydrodynamics the governing equations are the Navier-Stokes equations. They consist of the continuity equation, the momentum equations and the energy equation. In the case of vanishing viscosity the Navier-Stokes equations reduce to the Euler equations. Including contributions of electromagnetic fields yields the magnetohydrodynamic equations.

The continuity equation describes the conservation of mass. It reads:

$$\partial_t \rho + \vec{\nabla} (\rho \vec{v}) = 0, \tag{2.1}$$

where $\rho, \vec{v}$ are the density and fluid velocity, respectively. Vividly this equation says: The amount of mass inside a given volume can only change in time (first term) when there is a mass flow through its surface (second term). Together with the conservation of mass we need equations describing the conservation of the three components of momentum. In their conservative form these equations read:

$$\partial_t (\rho \vec{v}) + \vec{\nabla} (\rho \vec{v} \otimes \vec{v} + P) = \vec{f}. \tag{2.2}$$

$\rho\vec{v}, P$ and $\vec{f}$ correspond to momentum density, pressure and force density, respectively. The second term on the left-hand side represents convection of momentum by fluid and pressure gradients. $\vec{f}$ contains all sorts of yet unspecified forces that might act on the accretion flow. One possible external force is gravity, of course. In the case of the standard disk we will have to deal with viscous flows. Shearing viscosity will be represented by the term $2\vec{\nabla} (\nu\rho\sigma)$ on the right-hand side of (2.2). ν, σ are the coefficient of kinematic viscosity and the shear tensor, respectively[1]. We will have to include it later when we derive the standard disk solution of Shakura and Sunyaev (1973). Using (2.1) we can rewrite (2.2) to yield:

$$\rho \left(\partial_t + \vec{v}\vec{\nabla} \right) \vec{v} = -\vec{\nabla} P + \vec{f}. \tag{2.3}$$

One should note that the left-hand side can be rewritten as $\rho d\vec{v}/dt$. Now it is manifest that these equations have the form:

$$\text{"mass density"} \times \text{"acceleration"} = \text{"force density"}.$$

Hence the momentum equations are nothing but the continuous version of Newton's second law of motion.
The energy equation describes the flux of energy in the flow, caused by various effects. In conservative form it reads:

$$\partial_t \left(\frac{1}{2}\rho\vec{v}^2 + \rho\mathcal{E} \right) + \vec{\nabla} \left(\left(\frac{1}{2}\rho\vec{v}^2 + \rho\mathcal{E} + P \right) \vec{v} \right) = \vec{v}\vec{f} - \vec{\nabla}\vec{q}. \tag{2.4}$$

The first term on the left-hand side represents the conserved quantity, namely the total energy density, consisting of the kinetic energy density $\frac{1}{2}\rho\vec{v}^2$ and the internal energy density $\rho\mathcal{E}$. $\mathcal{E}$ is then the internal energy per unit mass. On the right-hand side there is a new quantity, the heat flux vector $\vec{q}$. It describes energy fluxes caused by various sorts of processes. These can be divided into two main categories: radiative fluxes, represented by the radiative flux vector $\vec{F}_{rad}$ and heat

[1] A detailed derivation of this term can be found in Novikov and Thorne (1973); Klessen (2008, page 12).

conduction, represented by the conductive flux vector $\vec{q}_C$, i.e.: $\vec{q} = \vec{F}_{rad} + \vec{q}_C$. The former is given by:

$$\vec{F}_{rad} = \int d\nu \int d\Omega \, \vec{n} I_\nu, \tag{2.5}$$

where I_ν is the intensity per unit frequency. In most cases we do not have to worry about further equations for the intensity but can work with approximations for $\vec{F}_{rad}$ (Frank et al., 1992). The transport of energy by radiation and heat conduction is given by $\vec{\nabla}\vec{F}_{rad}$ and $\vec{\nabla}\vec{q}_C$, respectively. Heat conduction is due to redistribution of thermal energy by turbulent motion. In many cases, though, $\vec{\nabla}\vec{q}_C$ can be dropped because temperature gradients are small enough (Frank et al., 1992). Hence, we approximate $\vec{q}$ as:

$$\vec{q} \approx \vec{F}_{rad}.$$

Just like for the momentum equations it is possible to use (2.1) and (2.2) to rewrite (2.4) to yield:

$$\rho \left(\partial_t + \vec{v}\vec{\nabla} \right) \mathcal{E} = -P\Theta - \vec{\nabla}\vec{q}, \tag{2.6}$$

where we have defined the volume expansion[2] $\Theta = \vec{\nabla}\vec{v}$. (2.6) has now the form of an evolution equation for $\mathcal{E}$. This will be most useful for analytic calculations. Just like we had to modify the momentum equations to include viscosity, we will have to add a term on the right-hand side of the energy equation describing heat generation by viscous dissipation. This will be the total contraction of the viscous shear tensor:

$$2\nu\rho \, Tr \, \sigma^2. \tag{2.7}$$

So far we have deduced the hydrodynamic (HD) equations. This will be sufficient in the case of the standard disk. To be able to deal with electromagnetic fields, though, we have to introduce Maxwell's equations. They read:

$$\begin{aligned} \vec{\nabla}\vec{E} &= \frac{q}{\varepsilon_0} && (2.8) \\ -\frac{1}{c^2}\partial_t \vec{E} + \vec{\nabla} \times \vec{B} &= \mu_0 \vec{j} && (2.9) \\ \vec{\nabla}\vec{B} &= 0 && (2.10) \\ \partial_t \vec{B} + \vec{\nabla} \times \vec{E} &= 0, && (2.11) \end{aligned}$$

where q is the charge density and $\vec{E}, \vec{B}, \vec{j}$ are the 3-vectors of the electric field, magnetic field and current density, respectively. Further, we have the speed of light c, the vacuum permeability μ_0 and the vacuum permittivity $\varepsilon_0 = (\mu_0 c^2)^{-1}$.

[2]The name "volume expansion" comes from the fact that one can show that $d(\ln V)/dt = \Theta$ (Misner et al., 1973, page 565).

In order to arrive at the magnetohydrodynamic (MHD) equations we also have to include Ohm's law. In the Newtonian regime it simply reads:

$$\vec{j} = \sigma \left(\vec{E} + \vec{v} \times \vec{B} \right), \tag{2.12}$$

where σ is the electric conductivity. It will be convenient to define the magnetic diffusivity η_M. It is connected to the electric conductivity σ by:

$$\eta_M = \frac{1}{\mu_0 \sigma}. \tag{2.13}$$

Acting with $\vec{\nabla}\times$ on (2.12) and inserting (2.9) and (2.11) yields:

$$\partial_t \vec{B} = \vec{\nabla} \times \left(\vec{v} \times \vec{B} \right) - \vec{\nabla} \times \left(\eta_M \left(\vec{\nabla} \times \vec{B} - \frac{1}{c^2} \partial_t \vec{E} \right) \right) \tag{2.14}$$

$$\Leftrightarrow$$

$$\left(\partial_t + \vec{v}\vec{\nabla} \right) \vec{B} = \left(\vec{B} \cdot \vec{\nabla} \right) \vec{v} - \vec{B}\Theta - \vec{\nabla} \times \left(\eta_M \left(\vec{\nabla} \times \vec{B} - \frac{1}{c^2} \partial_t \vec{E} \right) \right). \tag{2.15}$$

Now we have obtained an evolution equation for the magnetic field - the induction equation. The first term is called the advection term. It describes the deformation of the magnetic field by motion of the plasma. In the limit $\sigma \to \infty$ (ideal MHD) this would be the only term on the right-hand side. In this case magnetic field lines are "frozen" into the plasma. The second term is called the diffusion term. It plays an important role in the theory of reconnection: large currents occur within a small region making the diffusion term significant even in the case of large σ. In the Newtonian regime perturbations in the field topology propagate with velocities much smaller than the speed of light. Therefore one can usually neglect the displacement current in the diffusion term. The induction equation then reads:

$$\left(\partial_t + \vec{v}\vec{\nabla} \right) \vec{B} = \left(\vec{B} \cdot \vec{\nabla} \right) \vec{v} - \vec{B}\Theta - \vec{\nabla} \times \left(\eta_M \vec{\nabla} \times \vec{B} \right). \tag{2.16}$$

Now we have augmented the HD equations by the induction equation in order to obtain the MHD equations. Our intention is accomplished by modifying the momentum equations and the energy equation by electromagnetic contributions:

$$\rho \left(\partial_t + \vec{v}\vec{\nabla} \right) \vec{v} = -\vec{\nabla} \left(P + \frac{\vec{B}^2}{2\mu_0} \right) + \frac{1}{\mu_0} \left(\vec{B} \cdot \vec{\nabla} \right) \vec{B} + \vec{f} \tag{2.17}$$

$$\rho \left(\partial_t + \vec{v}\vec{\nabla} \right) \mathcal{E} = -P\Theta + \mu_0 \eta_M \vec{j}^2 - \vec{\nabla}\vec{q}. \tag{2.18}$$

The first magnetic term on the right-hand side of the momentum equations is called the magnetic pressure and the second corresponds to magnetic tension of the lines of force. Their origin lies in the Lorentz force density:

$$\vec{f}_L = q\vec{E} + \vec{j} \times \vec{B}. \tag{2.19}$$

One obtains the magnetic pressure- and tension terms by substituting (2.9) for $\vec{j}$ and neglecting the electric term. The ladder is usually a good approximation for a plasma in astrophysics since the time scale for establishing charge neutrality is of the order $10^{-9}\,s$ for reasonable parameters (see Frank et al., 1992).
The new term on the right-hand side of the energy equation describes heat generation by ohmic heating. This term is absent in the ideal MHD approximation. Further, it is the only term where electric fields appear explicitly in the MHD equations. There is no contribution of electric fields in the evolution of the magnetic fields or the Euler equations anymore. Yet they can be recovered by use of (2.12) and (2.9):

$$\vec{E} = -\vec{v} \times \vec{B} + \eta_M \vec{\nabla} \times \vec{B}. \tag{2.20}$$

Now we have derived the governing equations of magnetized, hydrodynamic flows using the Newtonian description of the gravitational field. In the following we will derive the standard disk solution from these equations. In Chapter 3 we will generalize the MHD equations to the relativistic regime.

2.2 The Standard Disk Solution

Consider an accretion flow around a central object. If there was no interaction between different gas particles, there could be no accretion at all.
All particles would just stay on elliptical orbits forever, since there would be no angular momentum transfer. There has to be some sort of interaction between the particles that exerts a torque and thus redistributes angular momentum. Molecular viscosity can not account for this torque, since its effect is too small by several orders of magnitude (see Frank et al., 1992). Turbulence in the accretion disk, on the other hand, might be able to act like an effective viscosity of sufficient magnitude. Therefore we will try to describe this interaction as by means of an anomalous viscosity with kinematic viscosity coefficient ν. The way this viscosity is generated remains undetermined within the standard disk model. Yet, it seems likely that the magnetorotational instability (MRI) is responsible for shearing in this flow (for further information see Balbus and Hawley, 1991).
The kinematic coefficient of viscosity is given by $\nu = v_t l_t$, where v_t and l_t are the typical velocity and length scale for the turbulent motion, respectively. Even though there is no sophisticated description of these two quantities, we can make two simple estimates that make it possible to parameterize our ignorance. We realize that turbulent eddies cannot exceed the disk height H. Also the typical turbulent velocity will not exceed the sound speed c_S. If it did, shocks would develop that dissipate this turbulent kinetic energy into thermal energy. Therefore we have $l_t \leq H$ and $v_t \leq c_S$, respectively. Correspondingly, Shakura and Sunyaev (1973) have parameterized the viscosity by:

$$\nu = \alpha c_S H. \tag{2.21}$$

Our whole ignorance has been concentrated into the parameter α. The only thing we can expect it to approximately satisfy is: $\alpha < 1$.
Consider now a close binary system where the secondary feeds the accretion flow onto the primary by Roche lobe overflow. The flow will have a sufficient amount of angular momentum to form an accretion disk instead of falling directly onto the primary (Frank et al., 1992). The dynamical time scale $t_{dyn} = r/v^{\varphi}$ will be very short. In order to be accreted the fluid particles have to move in the radial direction towards then central object thereby releasing gravitational energy. Viscous dissipation will convert rotational energy into thermal energy that can be radiated away. One can see that for the orbiting matter it is no problem energetically to move towards the center. But in order to move inwards it is not enough to loose rotational energy. The matter has to loose angular momentum, too. Viscous shearing forces act on the time scale $t_{vis} = r^2/\nu = r/v^r$. The dynamical time scale will usually be much shorter than the viscous time scale. We will therefore obtain a disk where the matter slowly spirals inwards. Motion in the φ-direction we will be close to the lowest energy orbits. These are circular orbits with the Keplerian angular velocity:

$$\Omega = \sqrt{\frac{GM}{r^3}}. \tag{2.22}$$

The disk will be compressed by centrifugal forces. Hence, we assume the disk to be geometrically thin, i.e. the thickness H of the disk satisfies $H/r \ll 1$. The thinness implies that all quantities depend very weakly on the vertical position within the disk. We will therefore use vertically averaged quantities. We define the surface density Σ by integrating the density over z in the disk region:

$$\Sigma = \int_{-\frac{H}{2}}^{\frac{H}{2}} dz\ \rho \approx H\rho. \tag{2.23}$$

In the second part we have exerted the assumption that quantities do not vary much within the disk. We will also use a mass-averaged radial velocity that is defined by:

$$\langle v^r \rangle = \frac{1}{\Sigma} \int_{-\frac{H}{2}}^{\frac{H}{2}} dz\ \rho v^r \approx v^r. \tag{2.24}$$

It is negligible compared to the orbital velocity: $\langle v^r \rangle \ll v^{\varphi} = r\Omega$. In our approximation we have a vertical velocity that is zero on average: $\langle v^z \rangle = 0$. We will also assume that the disk is stationary, $\partial_t = 0$, and perfectly axisymmetric, $\partial_{\varphi} = 0$. In order to write down the equations for the standard disk we have to quote the expression for the viscous force density that exerts the torque on the disk annuli.

This force density has a φ-component, only. It is given by[3]:

$$f_\varphi = \frac{1}{r}\partial_r\left(\nu\rho r^3\partial_r\Omega\right). \tag{2.25}$$

Now we turn to the energy equation (2.6): From the assumption that the disk is thin we conclude that most of the heat generated by viscous dissipation is directly radiated in the z-direction and does not go into internal forms. Hence, the contribution of $\mathcal{E}$ to the energy equation is negligible (Novikov and Thorne, 1973). Correspondingly there will be only small temperature gradients so we can approximate $\vec{\nabla}\vec{q} \approx \vec{\nabla}\vec{F}_{rad}$. Finally there will not be any strong compression of the flow so we can drop the $P\vec{\nabla}\vec{v}$-term. However, we have a significant amount of viscous heating. Thus we add the expression (2.7) on the right-hand side, leaving us with:

$$0 = -\vec{\nabla}\vec{F}_{rad} + 2\nu\rho r^2\cdot 2\sigma^{r\varphi 2}\ , \quad \text{where } \sigma^{r\varphi} = \frac{1}{2}\partial_r\Omega. \tag{2.26}$$

Since the flux of radiation is mainly in the vertical direction we can approximate $\vec{F} \approx F^z\vec{e}_z$. We then have $2F = \int_{-H/2}^{H/2} dz\ \partial_z F^z$ where $F = \pm F^z(z = \pm H)$ is the radiation flux from the disk surface.

Now we have all ingredients to quote the equations for the standard disk:

The continuity Equation:

$$\frac{1}{r}\partial_r\left(r\Sigma\left\langle v^r\right\rangle\right) = 0 \tag{2.27}$$

The momentum equations:

$$0 = \Sigma\left(r\Omega^2 - \frac{GM}{r^2}\right) \tag{2.28}$$

$$\Sigma\left\langle v^r\right\rangle\partial_r\left(r^2\Omega\right) = \frac{1}{r}\partial_r\left(\nu\Sigma r^3\partial_r\Omega\right) \tag{2.29}$$

$$0 = -\partial_z P - \rho\frac{GMz}{r^3} \tag{2.30}$$

The energy equation:

$$0 = -2F + \nu\Sigma r^2\left(\partial_r\Omega\right)^2 \tag{2.31}$$

It is not necessary to do the averaging in the vertical momentum equation. Before we can solve this set of equations we need to augmented it by an equation of state, the definition of the sound speed, a description of opacity and optical depth and an expression for the radiative flux.

[3] For a detailed derivation of this expression Frank et al. (see 1992, page 58).

To put the last thing first: we assume that the disk is optically thick, indicating that the radiated flux can be approximated that of a blackbody:

$$F = -\frac{16b}{3\kappa_R\rho}T^3\partial_z T. \tag{2.32}$$

where b and κ_r are the Stefan-Boltzmann constant the Rosseland mean opacity, respectively. The ladder is an average over the frequency dependent opacity. It is given by:

$$\frac{1}{\kappa_R} = \frac{\int d\nu \; \frac{1}{\kappa_\nu}\partial_T B_\nu}{\int d\nu \; \partial_T B_\nu}, \tag{2.33}$$

where $\partial_T B_\nu$ is the derivative of the normalized Planck distribution with respect to temperature. Electron scattering and free-free absorption are the two main contributions (Shakura and Sunyaev, 1973; Frank et al., 1992):

$$\kappa_{ff} = 6.6 \cdot 10^{22}\frac{cm^2}{g} \cdot \rho\left[\frac{g}{cm^3}\right](T_c[K])^{-\frac{7}{2}} \quad , \quad \kappa_{es} = 0.4\frac{cm^2}{g}. \tag{2.34}$$

To make this assumption self consistent we have to check that the optical depth τ indeed satisfies $\tau \gg 1$. Therefore we will evaluate:

$$\tau = \rho H \kappa_R(T_c) = \Sigma\kappa_R, \tag{2.35}$$

Provided that the disk is optically thick we approximate $\partial_z \approx -1/H$ in (2.32) to obtain:

$$F \approx \frac{4b}{3\tau}{T_c}^4. \tag{2.36}$$

In writing this we have assumed that the central temperature T_c greatly exceeds the surface temperature. The last two things that we add are the definition of the sound speed and the equation of state for an ideal gas and a radiation field, respectively:

$$\begin{aligned} {c_S}^2 &= \frac{P}{\rho}, \quad P = P_{gas} + P_{rad} && (2.37)\\ P_{gas} &= \frac{\rho k T_c}{\mu m_H} && (2.38)\\ P_{rad} &= \frac{4b}{3c}{T_c}^4, && (2.39) \end{aligned}$$

where m_H is the mass of the hydrogen atom, μ the mean molecular weight measured in units of m_H and c is the speed of light. We will divide the accretion disk into three parts. In the outer part, gas pressure dominates and the opacity is mainly due to free-free absorption. In the middle part, however, electron scattering becomes the main contribution to the opacity. The inner part is dominated by radiation pressure.

$$\begin{array}{lll} \text{outer region:} & P \approx P_{gas}\ , & \kappa_R \approx \kappa_{ff} \\ \text{middle region:} & P \approx P_{gas}\ , & \kappa_R \approx \kappa_{es} \\ \text{outer region:} & P \approx P_{rad}\ , & \kappa_R \approx \kappa_{es}. \end{array} \tag{2.40}$$

We have collected everything we need. It is now a simple matter of substitution to arrive at the standard disk solution (for a detailed derivation see Shakura and Sunyaev, 1973; Frank et al., 1992). In terms of the non-dimensional variables

$$\alpha,\ \dot{m} = \frac{\dot{M}}{10^{17}\, g\, s^{-1}},\ m = \frac{M}{M_\odot}\ \text{ and }\ x = \frac{r}{r_g}, \tag{2.41}$$

where $M_\odot$ is the solar mass and $r_g = GM/c^2$ is the gravitational radius, we obtain:

The outer solution:

$$\begin{aligned} \Sigma &= 1.7 \cdot 10^5\, g\, cm^{-2} \cdot \mu^{\frac{3}{4}}\, \alpha^{-\frac{4}{5}}\, \dot{m}^{\frac{7}{10}}\, m^{-\frac{1}{2}} x^{-\frac{3}{4}}\, f^{\frac{7}{10}} \\ H &= 3.7 \cdot 10^{-3}\, r_g \cdot \mu^{-\frac{3}{8}}\, \alpha^{-\frac{1}{10}}\, \dot{m}^{\frac{3}{20}}\, m^{-\frac{1}{4}}\, x^{\frac{9}{8}}\, f^{\frac{3}{20}} \\ \rho &= 3.1 \cdot 10^2\, g\, cm^{-3} \cdot \mu^{\frac{9}{8}}\, \alpha^{-\frac{7}{10}}\, \dot{m}^{\frac{11}{20}}\, m^{-\frac{5}{4}}\, x^{-\frac{15}{8}}\, f^{\frac{11}{20}} \\ T_c &= 1.5 \cdot 10^8\, K \cdot \mu^{\frac{1}{4}}\, \alpha^{-\frac{1}{5}}\, \dot{m}^{\frac{3}{10}}\, m^{-\frac{1}{2}}\, x^{-\frac{3}{4}}\, f^{\frac{3}{10}} \\ \tau_{ff} &= 8.2 \cdot 10^1 \cdot \mu\ \alpha^{-\frac{4}{5}}\, \dot{m}^{\frac{1}{5}}\, f^{\frac{1}{5}} \\ \nu &= 6.2 \cdot 10^{10}\, cm^2 s^{-1} \cdot \mu^{-\frac{3}{4}}\, \alpha^{\frac{4}{5}}\, \dot{m}^{\frac{3}{10}}\, m^{\frac{1}{2}}\, x^{\frac{3}{4}}\, f^{\frac{3}{10}} \\ \langle v^r \rangle &= -6.3 \cdot 10^5\, cm\, s^{-1} \cdot \mu^{-\frac{3}{4}}\, \alpha^{\frac{4}{5}}\, \dot{m}^{\frac{3}{10}}\, m^{-\frac{1}{2}}\, x^{-\frac{1}{4}}\, f^{-\frac{7}{10}} \\ c_S &= 1.1 \cdot 10^8\, cm\, s^{-1} \cdot \mu^{-\frac{3}{8}}\, \alpha^{-\frac{1}{10}}\, \dot{m}^{\frac{3}{20}}\, m^{-\frac{1}{4}}\, x^{-\frac{3}{8}}\, f^{\frac{3}{20}}, \end{aligned} \tag{2.42}$$

The middle solution:

$$\begin{aligned} \Sigma &= 4.5 \cdot 10^4\, g\, cm^{-2} \cdot \mu^{\frac{4}{5}}\, \alpha^{-\frac{4}{5}}\, \dot{m}^{\frac{3}{5}}\, m^{-\frac{2}{5}}\, x^{-\frac{3}{5}}\, f^{\frac{3}{5}} \\ H &= 7.3 \cdot 10^{-3}\, r_g \cdot \mu^{-\frac{2}{5}}\, \alpha^{-\frac{1}{10}}\, \dot{m}^{\frac{1}{5}}\, m^{-\frac{3}{10}}\, x^{\frac{21}{20}}\, f^{\frac{1}{5}} \\ \rho &= 4.1 \cdot 10^1\, g\, cm^{-3} \cdot \mu^{\frac{6}{5}}\, \alpha^{-\frac{7}{10}}\, \dot{m}^{\frac{2}{5}}\, m^{-\frac{11}{10}}\, x^{-\frac{33}{20}}\, f^{\frac{2}{5}} \\ T_c &= 5.8 \cdot 10^8\, K \cdot \mu^{\frac{1}{5}}\, \alpha^{-\frac{1}{5}}\, \dot{m}^{\frac{2}{5}}\, m^{-\frac{3}{5}}\, x^{-\frac{9}{10}}\, f^{\frac{2}{5}} \\ \tau_{es} &= 1.8 \cdot 10^4 \cdot \mu^{\frac{4}{5}}\, \alpha^{-\frac{4}{5}}\, \dot{m}^{\frac{3}{5}}\, m^{-\frac{2}{5}}\, x^{-\frac{3}{5}}\, f^{\frac{3}{5}} \\ \nu &= 2.4 \cdot 10^{11}\, cm^2 s^{-1} \cdot \mu^{-\frac{4}{5}}\, \alpha^{\frac{4}{5}}\, \dot{m}^{\frac{2}{5}}\, m^{\frac{2}{5}}\, x^{\frac{3}{5}}\, f^{\frac{2}{5}} \\ \langle v^r \rangle &= -2.4 \cdot 10^6\, cm\, s^{-1} \cdot \mu^{-\frac{4}{5}}\, \alpha^{\frac{4}{5}}\, \dot{m}^{\frac{2}{5}}\, m^{-\frac{3}{5}}\, x^{-\frac{2}{5}}\, f^{-\frac{3}{5}} \\ c_S &= 2.2 \cdot 10^8\, cm\, s^{-1} \cdot \mu^{-\frac{2}{5}}\, \alpha^{-\frac{1}{10}}\, \dot{m}^{\frac{1}{5}}\, m^{-\frac{3}{10}}\, x^{-\frac{9}{20}}\, f^{\frac{1}{5}}, \end{aligned} \tag{2.43}$$

The inner solution:

$$\begin{aligned}
\Sigma &= 2.1\, g\, cm^{-2} \cdot \alpha^{-1}\, \dot{m}^{-1}\, m\, x^{-\frac{3}{2}}\, f^{-1} && (2.44)\\
H &= 1.1\, r_g \cdot \dot{m}\, m^{-1}\, f && (2.45)\\
\rho &= 1.3 \cdot 10^{-5}\, g\, cm^{-3} \cdot \alpha^{-1}\, \dot{m}^{-2}\, m\, x^{-\frac{3}{2}}\, f^{-2} && (2.46)\\
T_c &= 4.8 \cdot 10^{7}\, K \cdot \alpha^{-\frac{1}{4}}\, m^{-\frac{1}{4}}\, x^{-\frac{3}{8}} && (2.47)\\
\tau_{es} &= 8.2 \cdot 10^{-1} \cdot \alpha^{-1}\, \dot{m}^{-1}\, m\, x^{-\frac{3}{2}}\, f^{-1} && (2.48)\\
\nu &= 5.1 \cdot 10^{15}\, cm^2 s^{-1} \cdot \alpha\, \dot{m}^{2}\, m^{-1}\, x^{-\frac{3}{2}}\, f^{2} && (2.49)\\
\langle v^r \rangle &= -5.2 \cdot 10^{10}\, cm\, s^{-1} \cdot \alpha\, \dot{m}^{2} m^{-2}\, x^{-\frac{5}{2}}\, f\\
c_S &= 3.2 \cdot 10^{10}\, cm\, s^{-1} \cdot \dot{m}\, m^{-1}\, x^{-\frac{3}{2}}\, f, && (2.50)
\end{aligned}$$

where $f = 1 - \sqrt{r_*/r}$ and r_* is an integration constant that is interpreted as the inner boundary of the disk (star surface or innermost stable orbit). The transition between the outer- and middle region and between the middle- and inner region is located at (Shakura and Sunyaev, 1973):

$$\begin{aligned}
\text{outer-middle:} \quad x f^{-\frac{2}{3}} &= 5.3 \cdot 10^{3} \cdot \dot{m}^{\frac{2}{3}}\, m^{-\frac{2}{3}}\\
\text{middle-inner:} \quad x f^{-\frac{16}{21}} &= 96 \cdot \alpha^{\frac{2}{21}}\, \dot{m}^{\frac{16}{21}}\, m^{-\frac{2}{3}}
\end{aligned} \qquad (2.51)$$

We will briefly review the assumptions we have made in order to verify that the solution is indeed self-consistent. Since the standard disk solution is not the main subject of this work, we will restrict ourselves to the outer solution. See Shakura and Sunyaev (1973); Frank et al. (1992) for a more detailed discussion.
Our assumptions have been that:

- the disk is geometrically thin
- the disk is optically thick
- the surface temperature T_s can be approximated by the central temperature T_c
- self-gravity of the disk matter can be neglected

We can now insert typical values for the outer disk region in stellar accreting systems, i.e.: $\mu = 0.615$, $\dot{m} = 0.1$, $m = 1$, $r = 10^{10}\,cm$:

$$\begin{aligned}
\frac{H}{r} &= 1.3 \cdot 10^{-2} \alpha^{-\frac{1}{10}} f^{\frac{3}{20}} \\
\tau_{ff} &= 32\,\alpha^{-\frac{4}{5}} f^{\frac{4}{5}} \\
\frac{T_s}{T_c} &\propto \tau^{\frac{1}{4}} \approx 2 \\
M_{disk} &< 10^{-10} M_{\odot} \alpha^{-\frac{4}{5}} \\
\langle v^r \rangle &\approx .3\,\frac{km}{s} \\
c_S &\approx 10\,\frac{km}{s} \\
v^{\varphi} &\approx 1000\,\frac{km}{s}.
\end{aligned}$$

One can see that if the standard disk solution holds, the disk will be geometrically thin. A further support is given by the fact that the radial drift is indeed very subsonic and the orbital velocity highly supersonic. The second assumption is also self-consistent since the disk is optically thick for all reasonable parameter values. The third assumption was that the surface temperature of the disk could be well approximated by the central temperature so one would not have to worry about its vertical profile. Since a ratio of about 2 is not too bad we can still consider this approximation roughly satisfied. Finally the integration of the surface density over the disk yields the result of the fourth line. Unless α is very small ($< 10^{-10}$) the total mass of the matter in the disk is still negligible compared to the mass of the central object.

Principally, there is no reason to believe that one should experience any problems extending this model to small radii. Yet the standard disk model has a fundamental flaw: the source of viscosity remains undetermined within the model. One might try to explain viscosity by MRI. In this case small scale magnetic fields would exert a torque on the annuli of the accretion disk and thus act as an effective viscosity. However, MRI also amplifies the magnetic fields. Therefore we should have a strong increase of the magnetic energy when we approach the inner region. It is likely that these strong magnetic fields will then undergo a topological change and become of large-scale structure. Once that happens, these fields can not be described by an effective viscosity anymore. They will significantly influence the accretion flow and we will have to face the fact that the standard disk model becomes invalid.

The goal of the next chapter will be the derivation of the general relativistic MHD (GRMHD) equations. In Chapter 4, we establish a model of the accretion flow in the close vicinity of the central object to explain the formation of relativistic outflows or jets. It is based on the GRMHD equations and includes magnetic fields explicitly.

Chapter 3

General Relativistic Magnetohydrodynamic Equations

For the sake of completeness we derive in this chapter the general relativistic magnetohydrodynamic (GRMHD) equations, adopting the two-temperature description. We will first introduce the stress-energy tensor and then, by means of the conservation of energy, derive the GRMHD equations, suitable to describe the accretion flow in the vicinity of a compact object. We will neglect viscous contributions to the stress-energy tensor, since magnetic fields suppress the generation of turbulence (see Hujeirat, 2004). In this case the equations governing the accretion flow are the Euler equations and Maxwell's equations instead of the Navier-Stokes equations.
Thereafter the GRMHD equations will be reduced to the case of a stationary, axisymmetric flow in the equatorial plane of the Kerr-spacetime. The components of velocity and electromagnetic field will be expressed in the basis of the ZAMO tetrad.

In the following we will make use of the Einstein summation convention, i.e. an implicit sum over spacetime coordinates is understood for repeated upper and lower indices. In the case of coordinates (x^0, x^1, x^2, x^3), say, a term of the form $a^\mu b_\mu$ corresponds to:

$$a^\mu b_\mu = a^0 b_0 + a^1 b_1 + a^2 b_2 + a^3 b_3. \tag{3.1}$$

3.1 The Stress-Energy Tensor

The stress-energy tensor takes a central role in the general theory of relativity, since it represents all sources of mass and energy that determine the geometry of spacetime in Einstein's equations[1]. These equations read:

$$\mathcal{G} = \frac{8\pi G}{c^4} T, \tag{3.2}$$

where $\mathcal{G}$ is the Einstein tensor, G is Newton's constant of gravitation and c is the speed of light. The Einstein Tensor is completely determined by the geometry of spacetime. Further, it is compatible with the conservation of energy which is given by:

$$\nabla \cdot T = 0 \quad \Leftrightarrow \quad \nabla \cdot \mathcal{G} = 0. \tag{3.3}$$

Hence, the Einstein tensor is given by the unique, divergence-free combination of the Ricci tensor $\mathcal{R}$, Ricci scalar R and metric g,

$$\mathcal{G} = \mathcal{R} - \frac{1}{2} g R. \tag{3.4}$$

The Ricci tensor and scalar are derived from the Riemann tensor which describes the curvature of spacetime (see e.g. Misner et al., 1973, for further details).
We assume that the total mass in the accretion disk is much smaller than the mass of the central black hole and thus self-gravitation of the flow is negligible. This means that we do not have to solve Einstein's equations for the complete system consisting of black hole plus accretion flow. Instead we choose the Kerr metric to describe spacetime. It is an axisymmetric vacuum solution of Einstein's equations, i.e. $\mathcal{G} = 0$.
The equations determining the motion of the plasma will be derived by means of the energy conservation condition $\nabla \cdot T = 0$. In order to write down these equations, though, we first need to know the stress-energy tensor. There are four forms of energy that contribute to it:

1. the stress-energy tensor for a perfect fluid containing the rest-mass- and internal energy density and pressure
2. viscous stresses caused by compression (bulk viscosity) and heat generation by differential rotation (shear viscosity)
3. heat fluxes that move energy through the fluid by heating and cooling
4. electric and magnetic fields generated by the motion of charged particles

In our model the inner region of the accretion disk is threaded by large-scale magnetic fields that are in excess of thermal equipartition. These fields will be strong enough to suppress the generation of turbulence and hence the source of viscous dissipation. We will therefore neglect the contributions of viscosity. The stress-energy tensor then consists of the three parts:

$$T = T_P + T_H + T_{EM}. \tag{3.5}$$

[1]The cosmological constant is assumed to equal zero.

T_P, the stress-energy tensor of a perfect fluid, is given by:

$$T_P{}^\mu{}_\nu = \rho \frac{\mathcal{H}}{c^2} \dot{x}^\mu \dot{x}_\nu + \delta^\mu{}_\nu P, \tag{3.6}$$

where ρ, $\mathcal{H}$ and P are the density, specific enthalpy and pressure, respectively. $\dot{x} = dx/d\tau$ is the four-velocity of the plasma and τ is its proper time. The specific enthalpy is given by:

$$\mathcal{H} = c^2 + \mathcal{E} + \frac{P}{\rho}, \tag{3.7}$$

where $\mathcal{E}$ is the internal energy per mass. The rest-mass density is simply given by the particle number density n times particle mass m: $\rho = nm^2$. P comprises gas, radiation and turbulent pressure but not magnetic pressure. The latter is contained in the electromagnetic stress-energy tensor.
Heating and cooling enters the stress-energy tensor by:

$$T_H{}^\mu{}_\nu = q^\mu \frac{\dot{x}_\nu}{c^2} + \frac{\dot{x}^\mu}{c^2} q_\nu, \tag{3.8}$$

where q is the heat flux vector which describes energy fluxes caused by various heating and cooling processes. q is purely spatial i.e. perpendicular to the fluid worldlines: $\dot{x} \cdot T_H = 0$. The most relevant processes in accretion flows are cooling by bremsstrahlung, comptonization and synchrotron radiation as well as heating by viscous dissipation and magnetic diffusivity. Other processes that cause heat flux are Coulomb coupling between the electrons and ions, adiabatic compression and heat conduction (Hujeirat, 2004).
The electromagnetic stress-energy tensor accounts for the energy content of the electromagnetic field, stresses exerted on the fluid by Lorentz forces and ohmic heating caused by electric currents running through a resistive plasma. This part is given in terms of the electromagnetic field strength tensor F that contains the components of the electric and magnetic fields. It will be defined properly in the next section and discussed together with Maxwell's equations.
The electromagnetic part is given by:

$$T_{EM}{}^\mu{}_\nu = \frac{1}{\mu_0} \left(F^{\mu\rho} F_{\nu\rho} - \frac{1}{4} \delta^\mu{}_\nu F^{\alpha\beta} F_{\alpha\beta} \right). \tag{3.9}$$

For completeness we quote now the full stress-energy tensor:

$$T^\mu{}_\nu = \rho \frac{\mathcal{H}}{c^2} \dot{x}^\mu \dot{x}_\nu + \delta^\mu{}_\nu P + q^\mu \frac{\dot{x}_\nu}{c^2} + \frac{\dot{x}^\mu}{c^2} q_\nu + \frac{1}{\mu_0} \left(F^{\mu\rho} F_{\nu\rho} - \frac{1}{4} \delta^\mu{}_\nu F^{\alpha\beta} F_{\alpha\beta} \right). \tag{3.10}$$

[2] In the case of a multi-component fluid one simply has $\rho = \sum_i n_i m_i$.

3.2 Derivation of the GRMHD Equations

The governing equations of the accretion flow are the GRMHD equations. The Euler equations can be derived by means of the vanishing divergence of the stress-energy tensor (3.3). It is a set of four independent equations. One can take the projection parallel and orthogonal to the timelike four-velocity $\dot{x}$ to obtain the internal energy equation and the momentum equations, respectively:

$$\dot{x} \cdot (\nabla \cdot T) = 0, \tag{3.11}$$
$$h \cdot (\nabla \cdot T) = 0, \tag{3.12}$$

where $h^{\mu\nu} = g^{\mu\nu} + \dot{x}^\mu \dot{x}^\nu / c^2$ is the projection tensor on the hypersurface orthogonal to $\dot{x}$. Instead of $h \cdot (\nabla \cdot T)$, it is also possible to directly take the three spatial components of $\nabla \cdot T$ as momentum equations. It will be more convenient in our case to make use of this possibility.

We assume that in the innermost part of the accretion disk there is a boundary layer of thickness $\approx 10 - 20$ Schwarzschild radii where magnetic fields are in excess of thermal equipartition. The jet launching region, on the other hand, is supposed to be a geometrically thin transition layer above the disk surfaces where the magnetic diffusivity is very large. Hence, we will have to describe the evolution of the magnetic fields to get a complete picture of accretion flow. Therefore we will derive the general relativistic version of the resistive induction equations.

The electromagnetic field strength tensor already appeared in the stress-energy tensor and will be defined properly in this section. We start with Maxwell's equations: their Newtonian form has been quoted in Section 2.1, page 35. We will confine ourselves to special relativity for a moment and introduce the four-vector potential $A = (A^0, \vec{A})$ by:

$$\frac{\vec{E}}{c} = -\partial_0 \vec{A} - \vec{\nabla} A^0 \tag{3.13}$$
$$\vec{B} = \vec{\nabla} \times \vec{A}, \tag{3.14}$$

where $\partial_0 = 1/c\, \partial_t$ in special relativity. One can now define the electromagnetic field strength tensor by:

$$F_{\mu\nu} = \partial_\mu A_\nu - \partial_\nu A_\mu, \tag{3.15}$$

where the greek indices adopt the values $(0, 1, 2, 3)$. The antisymmetry of the field strength tensor is manifest. One can also see that in the rest frame of the fluid the magnetic and electric field components are given by:

$$F^{0i} = \frac{E^i}{c}\,, \qquad F_{jk} = \varepsilon_{0jki} B^i, \tag{3.16}$$

or in matrix notation:

$$(F_{\mu\nu}) = \begin{pmatrix} 0 & -\frac{E^1}{c} & -\frac{E^2}{c} & -\frac{E^3}{c} \\ \frac{E^1}{c} & 0 & B^3 & -B^2 \\ \frac{E^2}{c} & -B^3 & 0 & B^1 \\ \frac{E^3}{c} & B^2 & -B^1 & 0 \end{pmatrix}. \tag{3.17}$$

We move directly to curved spacetime and rewrite the special relativistic expression (3.15) in an equivalent, yet general relativistic manner[3]:

$$F_{\mu\nu} = \nabla_\mu A_\nu - \nabla_\nu A_\mu, \tag{3.18}$$

where ∇ indicates covariant differentiation. We define the four-vector of the current density by $j = (c\rho, \vec{j})$. The general relativistic version of Maxwell's equations then becomes:

$$\begin{aligned} \nabla_\mu F^{\mu\nu} &= -\mu_0 j^\nu & (3.19) \\ \varepsilon^{\mu\nu\rho\sigma} \nabla_\nu F_{\rho\sigma} &= 0, & (3.20) \end{aligned}$$

where ε is the totally antisymmetric Levi-Civita symbol. Analogous to the Newtonian case we want to introduce Ohm's law now. Unfortunately it can be very complicated in general relativity (for a detailed treatment see Meier, 2004). In order to have any hope to obtain an analytic solution to the GRMHD equations, we have to settle for its most simple version. Hence, we make the approximation that:

$$\mu_0 \eta_M j^\nu = -\dot{x}_\mu F^{\mu\nu}. \tag{3.21}$$

This is the natural generalization of the Newtonian version (2.12). We will now write down the resistive induction equations in the form of an evolution equation for the field strength tensor. Using (3.20) we obtain:

$$\begin{aligned} \frac{dF_{\mu\nu}}{d\tau} &= \nabla_{\dot{x}} F_{\mu\nu} \\ &= \dot{x}^\rho \nabla_\rho F_{\mu\nu} \\ &= -\dot{x}^\rho \nabla_\nu F_{\rho\mu} - \dot{x}^\rho \nabla_\mu F_{\nu\rho} \\ &= F_{\rho\mu} \nabla_\nu \dot{x}^\rho + F_{\nu\rho} \nabla_\mu \dot{x}^\rho - \nabla_\nu \left(\dot{x}^\rho F_{\rho\mu}\right) - \nabla_\mu \left(\dot{x}^\rho F_{\nu\rho}\right) \\ &= 2F_{\rho[\mu} \nabla_{\nu]} \dot{x}^\rho - 2\nabla_{[\mu} \left(\dot{x}^\rho F_{\nu]\rho}\right), & (3.22) \end{aligned}$$

where [] indicates antisymmetrisation. Using (3.21), we arrive at the final expression:

$$\frac{1}{c}\frac{dF_{\mu\nu}}{d\tau} = 2F_{\rho[\mu} \nabla_{\nu]} \dot{x}^\rho - 2\nabla_{[\mu} \left(g_{\nu]\alpha} \mu_0 \eta_M j^\alpha\right). \tag{3.23}$$

[3]Due to the antisymmetry of the field strength tensor this expression is equivalent to its special relativistic version (3.15).

All Christoffel symbols cancel out if a coordinate basis is used. This becomes obvious if one derives this equation using the language of differential forms. Only ordinary partial derivatives are left and (3.23) takes the following form:

$$\dot{x}^\rho \partial_\rho F_{\mu\nu} = F_{\rho\mu}\partial_\nu \dot{x}^\rho - F_{\rho\nu}\partial_\mu \dot{x}^\rho - \partial_\mu \left(g_{\nu\alpha}\mu_0\eta_M j^\alpha\right) + \partial_\nu \left(g_{\mu\alpha}\mu_0\eta_M j^\alpha\right). \tag{3.24}$$

This is the general relativistic version of the resistive induction equations. One can check that this reduces to the ordinary classical version of the induction equations (2.16) if one uses the relation (3.16) for the electric and magnetic fields and sets all electric field components to vanish. (3.24) contains three additional equations determining the evolution of the electric field components. Yet it will be much simpler to use (3.21) to recover the electric fields:

$$\dot{x}_t F^{t\nu} = -\dot{x}_i F^{i\nu} - \mu_0\eta_M j^\nu. \tag{3.25}$$

Now we turn to the other five equations determining the evolution of the fluid[4]. One equation that can be quoted immediately is the continuity equation:

$$\nabla_\mu \left(\rho \dot{x}^\mu\right) = 0. \tag{3.26}$$

Since the rest mass density ρ equals particle mass times particle number density $\rho = mn$ the continuity equation states that the particle number density in a given volume is conserved. This is the case as long as we do not take nuclear reactions into account.

The stress-energy tensor is given by (3.10). Before we proceed further we will take a look at the divergence of its electromagnetic part $\nabla_\mu {T_{EM}}^\mu{}_\nu$ alone:

$$\begin{aligned}
\nabla_\mu {T_{EM}}^\mu{}_\nu &= \frac{1}{\mu_0}\nabla_\mu \left(F^{\mu\rho}F_{\nu\rho} - \frac{1}{4}\delta^\mu{}_\nu F^{\alpha\beta}F_{\alpha\beta}\right) \\
&= \frac{1}{\mu_0}F_{\nu\rho}\nabla_\mu F^{\mu\rho} + \frac{1}{\mu_0}\underbrace{F^{\mu\rho}\left(\nabla_\mu F_{\nu\rho} - \frac{1}{2}\nabla_\nu F_{\mu\rho}\right)}_{=\frac{1}{2}F^{\mu\rho}\cdot(3.20)=0} \\
&= \frac{1}{\mu_0}F_{\nu\rho}\nabla_\mu F^{\mu\rho} \\
&= -F_{\nu\rho}j^\rho.
\end{aligned} \tag{3.27}$$

The second term in the second line vanishes because it can be reformulated to equal (3.20), the homogeneous part of Maxwell's equations. In the last line we have used (3.19). The divergence of the full stress-energy tensor then becomes:

$$\nabla_\mu T^\mu{}_\nu = \nabla_\mu \left(\rho\frac{\mathcal{H}}{c^2}\dot{x}^\mu \dot{x}_\nu\right) + \nabla_\nu P + \nabla_\mu \left(q^\mu \dot{x}_\nu + \dot{x}^\mu q_\nu\right) - F_{\nu\rho}j^\rho = 0. \tag{3.28}$$

[4]Like in Section 2.2 this set of equations should be closed by additional constraints, i.e. an equation of state or a model of the fluid.

Making use of (3.21), (3.26) and of

$$\dot{x}^\nu \nabla_\mu x_\nu = \frac{1}{2}\nabla_\mu \dot{x}^2 = \frac{1}{2}\nabla_\mu(-1) = 0$$

we can quote the energy equation (3.11):

$$\rho \nabla_{\dot{x}} \mathcal{E} = -P\Theta + \mu_0 \eta_M j^2 + \sum_i (\pm\Lambda_i)\,, \tag{3.29}$$

where $\Theta = \nabla \cdot \dot{x}$ is the volume expansion in four-dimensional spacetime. The first term on the right-hand side of (3.29) accounts for heat generation by compression while the second term describes ohmic heating by electric currents running through the fluid. The Λ_i are heating- and cooling functions that represent all terms containing the heat flux vector q, namely:

$$\begin{array}{lcl} \Lambda_{con} & \hat{=} & \text{heat conduction} \\ \Lambda_{ie} & \hat{=} & \text{Coulomb coupling between electrons and ions} \\ \Lambda_{syn} & \hat{=} & \text{cooling by synchrotron emission} \\ \Lambda_B & \hat{=} & \text{Bremsstrahlung-cooling} \\ \Lambda_C & \hat{=} & \text{cooling by inverse Compton scattering} \end{array} \tag{3.30}$$

The term $\eta_M j^2$ in (3.29) will also be captured by a heating function, Λ_{Ohm}, in regions where we the ideal MHD approximation is invalid.

The three spacelike components of (3.28) yield the momentum equations. In the vicinity of the central object gravity is the most dominant force. We will therefore neglect thermal contributions to the equations of motion, i.e. we set $\mathcal{H} = c^2$ and $q = 0$ in the momentum equations (similar to the condition of negligible specific heat in Novikov and Thorne, 1973; Page and Thorne, 1974). Using (3.26) we obtain:

$$\rho \nabla_{\dot{x}} \dot{x}_\nu = -\nabla_\nu P + F_{\nu\rho} j^\rho. \tag{3.31}$$

Now we have derived the complete set of the GRMHD equations. To recapitulate we will quote the results again:

$$\begin{array}{lrcl} \text{The Continuity Equation:} & \nabla_\mu\left(\rho\dot{x}^\mu\right) & = & 0 \\ \text{The Energy Equation:} & \rho\nabla_{\dot{x}}\mathcal{E} & = & -P\Theta + \mu_0\eta_M j^2 + \sum_i (\pm\Lambda_i) \\ \text{The Momentum Equations:} & \rho\nabla_{\dot{x}}\dot{x}_\mu & = & -\nabla_\mu P + F_{\mu\nu} j^\nu \\ \text{The MHD Equations:} & \partial_{\dot{x}} F_{\mu\nu} & = & 2F_{\rho[\mu}\partial_{\nu]}\dot{x}^\rho - 2\partial_{[\mu}\left(g_{\nu]\rho}\mu_0\eta_M j^\rho\right) \end{array} \tag{3.32}$$

We have written these equations in a very compact form that allows for general manipulations in a very simple manner. In order to perform any specific calculations, however, we will have to rewrite them into a more explicit form. Let g be the determinant of the metric and

$$\begin{array}{rcl} \Theta & = & \frac{1}{\sqrt{|g|}}\partial_\mu\left(\sqrt{|g|}\dot{x}^\mu\right) \\ j^\rho & = & -\frac{1}{\mu_0\sqrt{|g|}}\partial_\mu\left(\sqrt{|g|}F^{\mu\rho}\right) \end{array} \tag{3.33}$$

the volume expansion and electric current density, respectively, then the GRMHD equations read:

The Continuity Equation:

$$\frac{1}{\sqrt{|g|}}\partial_\mu\left(\sqrt{|g|}\rho\dot{x}^\mu\right)=0 \tag{3.34}$$

The Momentum Equations:

$$\rho\dot{x}^\mu\partial_\mu\dot{x}_\alpha=-\partial_\alpha P+\frac{1}{2}\rho\dot{x}^\mu\dot{x}^\nu\partial_\alpha g_{\mu\nu}+F_{\alpha\rho}j^\rho \tag{3.35}$$

The Energy Equation:

$$\rho\dot{x}^\mu\partial_\mu\mathcal{E}=-P\Theta+\sum_i\left(\pm\Lambda_i\right) \tag{3.36}$$

The Induction Equations:

$$\dot{x}^\rho\partial_\rho F_{\mu\nu}=F_{\rho\mu}\partial_\nu\dot{x}^\rho-F_{\rho\nu}\partial_\mu\dot{x}^\rho-\partial_\mu\left(g_{\nu\alpha}\mu_0\eta_M j^\alpha\right)+\partial_\nu\left(g_{\mu\alpha}\mu_0\eta_M j^\alpha\right) \tag{3.37}$$

The Electric Field Equations (Ohm's Law):

$$\dot{x}_t F^{t\nu}=-\dot{x}_i F^{i\nu}-\mu_0\eta_M j^\nu \tag{3.38}$$

Now the GRMHD equations have been rewritten into a form that can be readily applied to any specific model. We have included (3.25) for later use.

3.3 The Governing Equations

In the last section we have presented the GRMHD equations. Now we want to reduce them to a form appropriate to elaborate the new model. In the following we will assume that the central object is a rotating black hole since the most energetic jets are believed to originate from their vicinity. This is not a requirement of the model, though. The basic assumptions of the model are independent of the central object. We assume that the mass of the black hole greatly exceeds the total mass of the accretion disk so the spacetime can be approximately described by the Kerr metric. Further, we assume that the disk lies in the equatorial plane and the system is reflection-symmetric. In the Newtonian model the domain of interest was geometrically thin (Hujeirat, 2004) thus we stay close to the equatorial plane: $\theta-\pi/2\approx 0$. Since we expect this assumption to hold in the general relativistic regime we approximate the Kerr-metric by:

$$g=-\alpha^2c^2dt^2+\varpi^2\left(d\varphi-\omega dt\right)^2+\frac{r^2}{\Delta}dr^2+r^2d\theta^2, \tag{3.39}$$

where the metric functions in the equatorial plane, correct up to order $(\theta - \pi/2)^2$, read:

$$\begin{aligned}
\alpha &= \frac{\sqrt{\Delta}}{\varpi} && (3.40)\\
\varpi &= \frac{\Sigma}{r} && (3.41)\\
\omega &= \frac{2r_g^2 car}{\Sigma^2} && (3.42)\\
\Sigma &= \sqrt{r^4 + r_g^2 a^2 r^2 + 2r_g^3 a^2 r} && (3.43)\\
\Delta &= r^2 - 2r_g r + r_g^2 a^2, && (3.44)
\end{aligned}$$

where $r_g = GM/c^2$ is the gravitational radius, M is the mass of the central object and $a \in [-1, 1]$ is the non-dimensional Kerr-parameter.
We want to study time independent, axisymmetric accretion flows. Hence, we have $\partial_t = \partial_\varphi = 0$. We use the tetrad system of the zero angular momentum observer (ZAMO, see e.g. Camenzind, 2007). In the case of the Kerr metric (3.39) the sets of basis one-forms e^a and vectors e_a read:

$$\begin{aligned}
e^0 &= \alpha c dt & e_0 &= \frac{1}{\alpha c}\left(\partial_t + \omega \partial_\varphi\right)\\
e^1 &= \frac{r}{\sqrt{\Delta}} dr & e_1 &= \frac{\sqrt{\Delta}}{r}\partial_r\\
e^2 &= r d\theta & e_2 &= \frac{1}{r}\partial_\theta\\
e^3 &= \varpi\left(d\varphi - \omega dt\right) & e_3 &= \frac{1}{\varpi}\partial_\varphi.
\end{aligned} \tag{3.45}$$

We will distinguish between the ZAMO frame and the coordinate frame by using the numbers $(0, 1, 2, 3)$ for the former and letters (t, r, θ, φ) for the latter. By means of the ZAMO frame we can define the components of the electric and magnetic fields as:

$$\begin{aligned}
E^r &= cF^{01} & B^r &= F_{23}\\
E^\theta &= cF^{02} & B^\theta &= F_{31}\\
0 &= F^{03} & B^\varphi &= F_{12}.
\end{aligned} \tag{3.46}$$

The vanishing of F^{03} for arbitrary r, θ is equivalent to the vanishing of $F_{t\varphi}$. The latter can be made manifest by writing $F_{t\varphi}$ in terms of the four-vector potential (3.18):

$$F_{t\varphi} = \frac{1}{c}\partial_t A_\varphi - \partial_\varphi A_t. \tag{3.47}$$

In the case of stationarity and axisymmetry this automatically yields $F_{t\varphi} = 0$. Now we can express the components of the field-strength tensor in the coordinate frame in terms of the electric and magnetic field components:

$$
\begin{aligned}
F_{tr} &= -\frac{r}{\varpi c}E^r - \frac{\omega r}{\alpha c}B^\theta & F^{tr} &= \frac{\varpi}{rc}E^r \\
F_{t\theta} &= -\frac{\alpha r}{c}E^\theta + \frac{\omega\varpi r}{c}B^r & F^{t\theta} &= \frac{1}{\alpha rc}E^\theta \\
F_{r\theta} &= \frac{r^2}{\sqrt{\Delta}}B^\varphi & F^{r\theta} &= \frac{\sqrt{\Delta}}{r^2}B^\varphi \\
F_{\varphi r} &= \frac{r}{\alpha}B^\theta & F^{\varphi r} &= \frac{\omega\varpi}{rc^2}E^r + \frac{\alpha}{r}B^\theta \\
F_{\theta\varphi} &= r\varpi B^r & F^{\theta\varphi} &= -\frac{\omega}{\alpha rc^2}E^\theta + \frac{1}{r\varpi}B^r .
\end{aligned}
\tag{3.48}
$$

The electric current density j then becomes:

$$j^t = \frac{1}{\mu_0 cr^2}\partial_r\left(r\varpi E^r\right) + \frac{1}{\mu_0 c\alpha r}\partial_\theta E^\theta \tag{3.49}$$

$$j^r = \frac{\sqrt{\Delta}}{\mu_0 r^2}\partial_\theta B^\varphi \tag{3.50}$$

$$j^\theta = -\frac{1}{\mu_0 r^2}\partial_r\left(\sqrt{\Delta}B^\varphi\right) \tag{3.51}$$

$$j^\varphi = \frac{1}{\mu_0 r^2}\partial_r\left(\frac{r\omega\varpi}{c^2}E^r + \alpha r B^\theta\right) + \frac{1}{\mu_0}\partial_\theta\left(\frac{\omega}{\alpha rc^2}E^\theta - \frac{1}{r\varpi}B^r\right). \tag{3.52}$$

Next we turn to the four-velocity of the plasma:

$$
\begin{aligned}
\dot{x} &= \dot{t}\partial_t + \dot{r}\partial_r + \dot{\theta}\partial_\theta + \dot{\varphi}\partial_\varphi \\
&= \gamma\left(ce_0 + v^r e_1 + v^\theta e_2 + v^\varphi e_3\right).
\end{aligned}
\tag{3.53}
$$

The v^i in the second line are the velocities that a ZAMO would measure. On the contrary to the standard disk solution we have to include a small vertical drift $v^\theta \ll v^r, v^\varphi$. We will neglect this vertical drift wherever possible.
The new model will be explained in detail in the next chapter. So far it should only be said that Alfvén waves propagating along the lines of a strong, poloidal magnetic field serve as mechanism for transport of angular momentum in the vertical direction. If the magnetic field energy is in excess of thermal equipartition this process can operate on the dynamical time scale or even faster (Hujeirat, 2004). Hence, we expect the orbital velocity of the disk matter to be strongly reduced, causing it to fall very rapidly towards the central object. Calculations show that the accreted material passes the event horizon in the radial direction, traveling with the speed of light (Camenzind and Mueller, 2004). Thus we do not expect the radial velocity v^r to maintain negligible compared to the orbital

velocity v^{φ}.
The velocity components and Lorentz-factor are given by:

$$\begin{aligned}
v^r &= \frac{r}{\alpha\sqrt{\Delta}}\frac{dr}{dt} \\
v^\theta &= \frac{r}{\alpha}\frac{d\theta}{dt} \\
v^\varphi &= \frac{\varpi}{\alpha}\left(\Omega-\omega\right)\ , \quad \Omega=\frac{d\varphi}{dt} \\
\gamma &= \alpha\frac{dt}{d\tau} \approx \frac{1}{\sqrt{1-\frac{v^{r2}}{c^2}-\frac{v^{\varphi 2}}{c^2}}}.
\end{aligned} \tag{3.54}$$

Now we are ready to quote the full set of axisymmetric, time independent equations governing the accretion flow:

The Continuity Equation:

$$\frac{1}{r^2}\partial_r\left(r\rho\sqrt{\Delta}\gamma v^r\right)+\frac{1}{r}\partial_\theta\left(\rho\gamma v^\theta\right)=0 \tag{3.55}$$

The Radial Momentum Equation:

$$\begin{aligned}
\rho\gamma v^r\partial_r\left(\gamma v^r\right) &= -\partial_r P+\frac{1}{2}\rho\left\{c^2\dot{t}^2\partial_r g_{tt}+2c\dot{t}\dot{\varphi}\partial_r g_{t\varphi}+\dot{\varphi}^2\partial_r g_{\varphi\varphi}\right\}- \\
&-\frac{B^\varphi}{\mu_0\sqrt{\Delta}}\partial_r\left(\sqrt{\Delta}B^\varphi\right)-\frac{B^\theta}{\mu_0\sqrt{\Delta}}\partial_\theta\left(\frac{\omega\varpi}{\alpha c^2}E^\theta-B^r\right)- \\
&-\frac{B^\theta}{\mu_0\alpha r}\partial_r\left(\frac{r\omega\varpi}{c^2}E^r+\frac{r}{\alpha}B^\theta\right)+ \\
&+\frac{1}{\mu_0 c^2}\left(E^r+\frac{\omega\varpi}{\alpha}B^\theta\right)\left(\frac{1}{r\varpi}\partial_r\left(r\varpi E^r\right)+\frac{1}{\sqrt{\Delta}}\partial_\theta E^\theta\right)
\end{aligned} \tag{3.56}$$

The Vertical Momentum Equation:

$$\begin{aligned}
0 &= -\partial_\theta P+\theta\gamma^2\rho\left(\frac{r_g^2 a^2}{r^2}v^{r2}-\frac{v^{\varphi 2}}{\mathcal{S}^2}\right)-\frac{B^\varphi}{\mu_0}\partial_\theta B^\varphi+ \\
&+\frac{B^r}{\mu_0}\partial_\theta\left(\frac{\omega\varpi}{\alpha c^2}E^\theta-B^r\right)+\frac{\varpi}{\mu_0 r}B^r\partial_r\left(\frac{r\omega\varpi}{c^2}E^r+\frac{r}{\alpha}B^\theta\right)+ \\
&+\frac{1}{\mu_0 c^2}\left(E^\theta-\frac{\omega\varpi}{\alpha}B^r\right)\left(\frac{\alpha}{r}\partial_r\left(r\varpi E^r\right)+\partial_\theta E^\theta\right)
\end{aligned} \tag{3.57}$$

The Angular Momentum Equation:

$$\rho\gamma v^r \frac{\sqrt{\Delta}}{r}\partial_r l = \frac{\varpi}{\mu_0 r}\left(B^r\partial_r\sqrt{\Delta} + B^\theta\partial_\theta\right)B^\varphi \tag{3.58}$$

The Energy Equation for the Electrons:

$$\rho\gamma v^r \frac{\sqrt{\Delta}}{r}\partial_r \mathcal{E}_e = -\frac{P_e}{r^2}\partial_r\left(r\sqrt{\Delta}\gamma v^r\right) + \Lambda_{con} + \Lambda_{Ohm} + \Lambda_{ie} - \Lambda_{syn} - \Lambda_B - \Lambda_C \tag{3.59}$$

The Energy Equation for the Ions:

$$\rho\gamma v^r \frac{\sqrt{\Delta}}{r}\partial_r \mathcal{E}_i = -\frac{P_i}{r^2}\partial_r\left(r\sqrt{\Delta}\gamma v^r\right) + \Lambda_{con} + \Lambda_{Ohm} - \Lambda_{ie} \tag{3.60}$$

The Radial Induction Equation:

$$0 = \partial_\theta\left(\varpi\gamma v^r B^\theta\right) + \partial_\theta\left(\eta_M\left(\frac{\varpi^3}{rc^2}E^r\partial_r\omega + \frac{\varpi^2}{r^2}\partial_r\left(\alpha r B^\theta\right) - \frac{\varpi}{r}\partial_\theta B^r\right)\right) \tag{3.61}$$

The Vertical Induction Equation:

$$0 = -\partial_r\left(\varpi\gamma v^r B^\theta\right) - \partial_r\left(\eta_M\left(\frac{\varpi^3}{rc^2}E^r\partial_r\omega + \frac{\varpi^2}{r^2}\partial_r\left(\alpha r B^\theta\right) - \frac{\varpi}{r}\partial_\theta B^r\right)\right) \tag{3.62}$$

The Toroidal Induction Equation:

$$\begin{aligned}\frac{r}{\sqrt{\Delta}}\partial_t B^\varphi \;=\;& \frac{1}{r}\partial_r\left(r\alpha\left(v^\varphi B^r - v^r B^\varphi\right)\right) + \frac{1}{\varpi}\partial_\theta\left(v^\varphi B^\theta\right) + \varpi B^r\partial_r\omega + \\ & + \frac{1}{r}\partial_r\left(\frac{\alpha\eta_M}{\gamma}\partial_r\left(\sqrt{\Delta}B^\varphi\right)\right) + \frac{1}{r\varpi}\partial_\theta\left(\frac{\eta_M}{\gamma}\partial_\theta B^\varphi\right)\end{aligned} \tag{3.63}$$

The Equation for the Radial Electric Field:

$$E^r = v^\varphi B^\theta + \frac{\eta_M}{\gamma}\frac{1}{r}\partial_\theta B^\varphi \tag{3.64}$$

The Equation for the Vertical Electric Field:

$$E^\theta = v^r B^\varphi - v^\varphi B^r - \frac{\eta_M}{\gamma}\frac{1}{r}\partial_r\left(\sqrt{\Delta}B^\varphi\right) \tag{3.65}$$

Additionally, we also include one component of the homogeneous Maxwell equations. It will be needed for two-dimensional plots of the poloidal magnetic-field:

$$\partial_r\left(r\varpi B^r\right) + \partial_\theta\left(\frac{r}{\alpha}B^\theta\right) = 0. \tag{3.66}$$

We want to consider stationary, i.e. time independent scenarios. Yet we have included a partial derivative with respect to time in equation (3.63). This will be useful when we estimate the time scale on which this field component is generated. In the vertical momentum equation we have made the substitution:

$$\mathcal{S} := \left(1 + \frac{r_g a}{r^2}\frac{\omega}{c}\left(\left(r^2 + r_g^2 a^2\right)\left(1 + \frac{c^2}{v^{\varphi 2}}\right) - 2 r_g a \sqrt{\Delta}\frac{c}{v^{\varphi}}\right)\right)^{-\frac{1}{2}}. \tag{3.67}$$

Chapter 4

A General Relativistic Model for Jet Formation

We have discussed the standard disk solution in Chapter 2 and derived and simplified accordingly the GRMHD equations in Chapter 3. In this chapter we discuss the new model for the inner region of the accretion disk. Before we proceed to solve the reduced GRMHD equations, though, the reader should have a clear picture of the model. Therefore the first section of this chapter is dedicated to a complete qualitative description.
In principal the model can be applied to accretion flows around black holes, neutron stars, white dwarfs or YSO's. In this work the emphasis is on jet formation around black holes, especially rotating black holes, since their vicinity lies in the deepest gravitational potential well where the most energetic outflows can be launched. A black hole is different from other accretors because it has no surface and does not radiate. If one includes effects due to a hard surface as well as heating by radiation from the central object, the model proposed in this work can be readily applied to different types of accretors.

4.1 A qualitative Description of the Model

Consider an accretion disk around a central black hole. The black hole dominates the dynamics in the disk gravitationally. At large distance from the center the flow is well described by the standard disk solution that was discussed in Section 2.2. Small scale magnetic fields cause turbulent motion thus generating an effective viscosity via the MRI (Balbus and Hawley, 1991). Suppose that at one point the magnetic energy is below equipartition with the thermal energy of the flow. In this case the ratio of magnetic- to gas pressure satisfies $\beta = P_{mag}/P_{gas} \ll 1$. The flow radiates by viscous dissipation due to turbulent motion in the plasma. MRI amplifies magnetic fields on the dynamical time scale, though. Hence the magnetic energy increases rapidly. Reconnection of magnetic flux tubes will probably

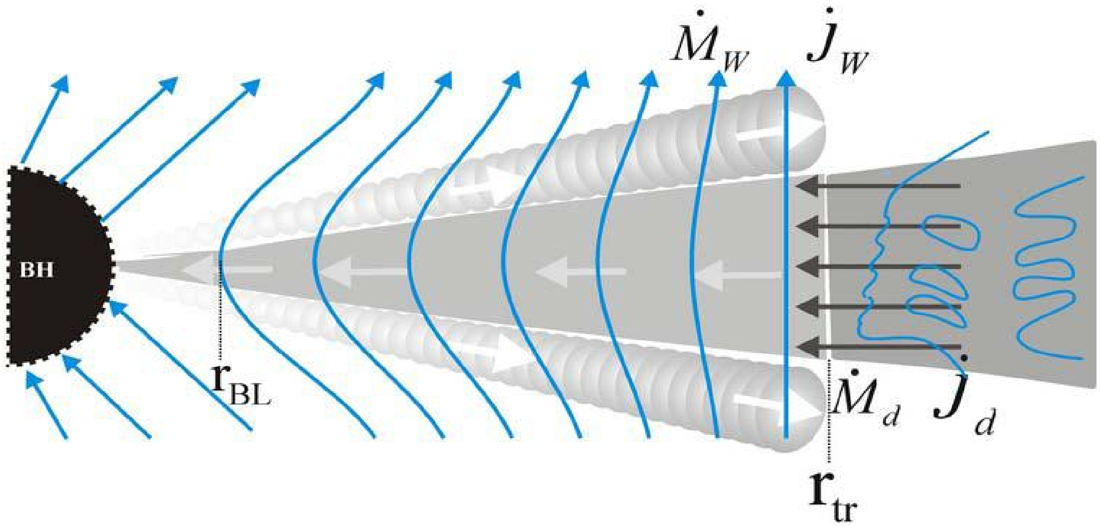

Figure 4.1: Schematic illustration of the model

Ideal MHD is assumed within the disk so magnetic lines of force are dragged with the accretion flow. A geometrically thin, super-Keplerian rotating and highly diffusive transition layer forms on the surfaces of the disk. The matter in the transition layer is centrifugally accelerated outwards, advecting a part of the toroidal magnetic field component. Thus a wind is formed that, at large radii, can be collimated to a jet by Lorentz forces.
Credit: Hujeirat (2004)

ensure that $\beta < 1$. However, there is no reason to expect that $\beta < 1$ is strictly valid in the whole accretion flow. MRI in combination with Parker instability, reconnection and inward motion results in large-scale, poloidal magnetic fields with magnetic energy around thermal equipartition (Hujeirat et al., 2003). The conductivity of the fluid particles is expected to be very high, hence we assume the ideal MHD approximation to hold in the disk. "Freezing" of the magnetic field lines into the disk plasma will further increase the magnetic energy as the central black hole is approached. Super equipartition magnetic fields will suppress the generation of turbulence which is the quintessence of the standard α-disk. In the absence of turbulence there is no viscous torque and also no source of local radiation. Therefore the disk will become much fainter than a standard disk. The question to be answered is: what is the nature of an accretion flow that proceeds under $\beta \geq 1$ and includes a highly energetic outflow?
Let r_{tr} be the radius where magnetic fields are in equipartition with the thermal energy. Exterior to r_{tr} we approximate the flow by the standard α-disk model. Interior to r_{tr} magnetic fields are predominantly poloidal and of large-scale topology and the ideal MHD approximation holds. In this case the magnetic lines of force will be dragged with the motion of the plasma particles. This leads to deformation of the field lines and causes torsional Alfvén waves. Alfvén waves transport

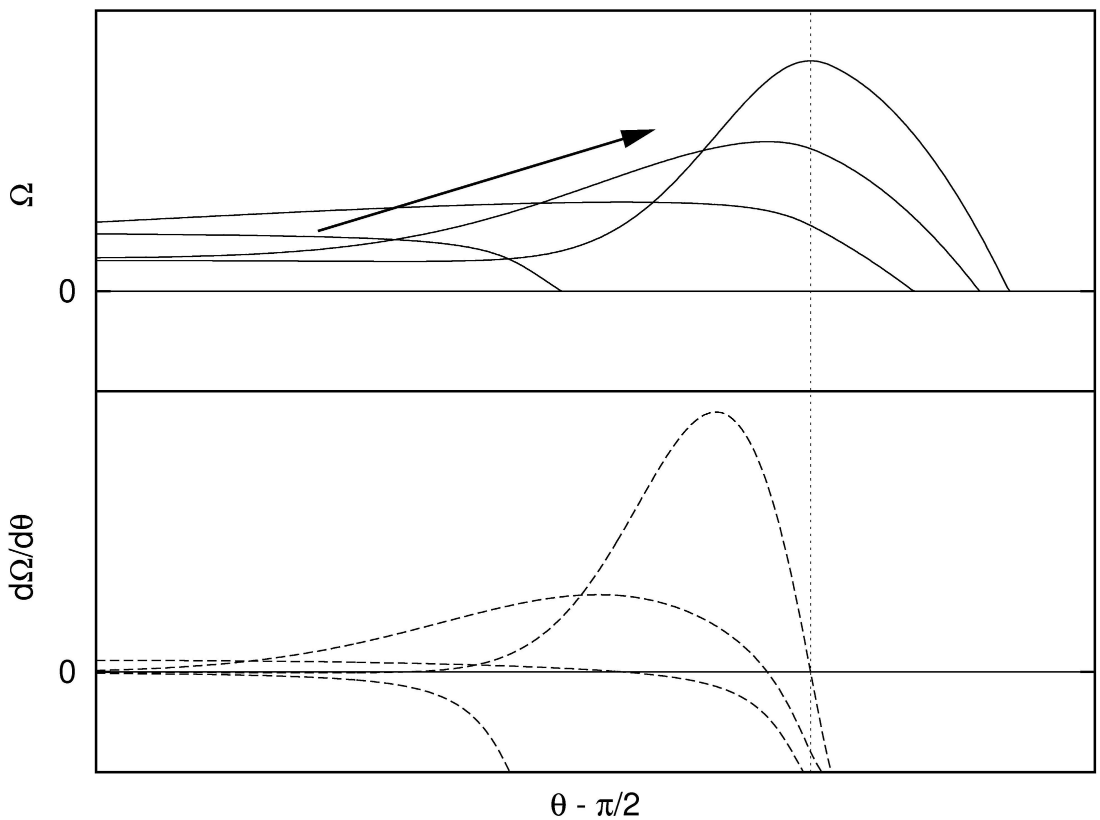

Figure 4.2: The vertical profile of Ω and $\partial_\theta \Omega$

Angular momentum from the disk deforms the vertical profile of Ω leading to a strong gradient $\partial_\theta \Omega$. A toroidal magnetic field B^φ is induced that undergoes a sign change where Ω achieves a maximum. This leads to the intersection and subsequent reconnection of flux tubes of opposite sign. In the following the vertical gradient of Ω is strengthened even further.

angular momentum in the vertical direction on the time scale $t_A = H_d/v_A^\theta$ where H_d is the disk half-thickness and v_A is the Alfvén velocity along poloidal field lines (properly defined in (4.40), page 71). Since magnetic fields are in excess of thermal equipartition, t_A is of the same order as the dynamical time scale $t_{dyn} = r/v^\varphi$ making Alfvén waves the dominant angular momentum carrier. The larger the value of r_{tr} the more rotational energy is extracted from the disk. If r_{tr} is too large, on the other hand, magnetic fields will become strong enough to terminate accretion by magnetic pressure. Hence, it is estimated that $r_{tr} = O(10 - 20\, r_S)$, where r_S is the Schwarzschild radius (Hujeirat et al., 2003; Hujeirat, 2004).
Supplied with angular momentum from the disk, the matter in higher latitudes will start to rotate faster inducing a vertical gradient $\partial_\theta \Omega$ of the angular velocity of the kind depicted in Fig. 4.2. At a certain latitude Ω achieves a maximum so $\partial_\theta \Omega$ changes sign. Inspection of the toroidal induction equation (3.63) reveals that, due to the geometrical thinness of the accretion disk, the dominant term in

the advective part is the one containing $B^\theta v^\varphi \propto \partial_\theta \Omega$. Hence, the vertical gradient $\partial_\theta \Omega$ induces a toroidal magnetic field. Where $\partial_\theta \Omega$ changes sign toroidal flux tubes of opposite sign are induced. These flux tubes will frequently intersect and subsequently reconnect the magnetic field lines. Thus reconnection terminates the propagation of Alfvén waves and traps angular momentum transported with them at this latitude. However, this will supply the matter with even more angular momentum leading to even faster rotation and a stronger vertical gradient $\partial_\theta \Omega$. Reconnection of the toroidal field will become even more frequent and the trapping of Alfvén waves even more efficient. Consequently, Alfvén waves can not deposit angular momentum in the corona or the interstellar medium but in a geometrically thin layer, the transition layer (TL), on the surfaces of the accretion disk.

The matter in the TL will rotate with super-Keplerian velocities and become potentially unbound.

An accretion flow can not maintain Keplerian rotation if threaded by strong magnetic fields that extract angular momentum on a time scale comparable to t_{dyn}. Let us suppose that $\Omega = c\,\Omega_K \propto r^{-\frac{3}{2}}$, where Ω_K is the Keplerian angular velocity and c a constant. If $c = 1$ the matter is in Keplerian rotation implying that the accretion process operates very slowly. Consequently the cooling time scales will be shorter than the dynamical time scale. In this case the accretion flow turns into a cool disk, threaded by super-equipartition magnetic fields which are likely to terminate accretion. If $c < 1$ the matter is in sub-Keplerian rotation but able to maintain $\Omega \propto r^{-\frac{3}{2}}$. Hence, the amount of rotational energy extracted per annulus from the disk can not be too large so r_{tr} must move to larger radii which was already excluded above (Hujeirat, 2004). Calculations with the implicit solver IRMHD3 show that the angular velocity in TL obeys the power law $\Omega \propto r^{-\frac{5}{4}}$ (Hujeirat et al., 2002, 2003). In this model we make the basic assumption that the angular velocity adopts the profile $\Omega \propto r^{-\frac{5}{4}}$ in the disk and in the TL.

So far we have established the formation of a diffusive, geometrically thin, super-Keplerian rotating transition layer on the surfaces of the disk. The matter in the TL is provided by the disk by means of a slow vertical drift. Due to the high reconnection rate and inefficient cooling the ions the TL will achieve very high temperatures. The super-Keplerian rotating plasma will be accelerated by centrifugal forces, forming a radial wind that is dominated by virial-hot ions. A fraction of the toroidal magnetic field in the TL is advected with the wind. At large distances the flow ceases to be diffusive and the magnetic field redirects and collimates the outflow into a jet (see Fig. 4.3).

Numerical calculations of Hujeirat et al. (2002) have shown that a fraction of roughly $\dot{M}_w/\dot{M}_d \approx 1/20$ of the inflowing matter reappears in the wind.

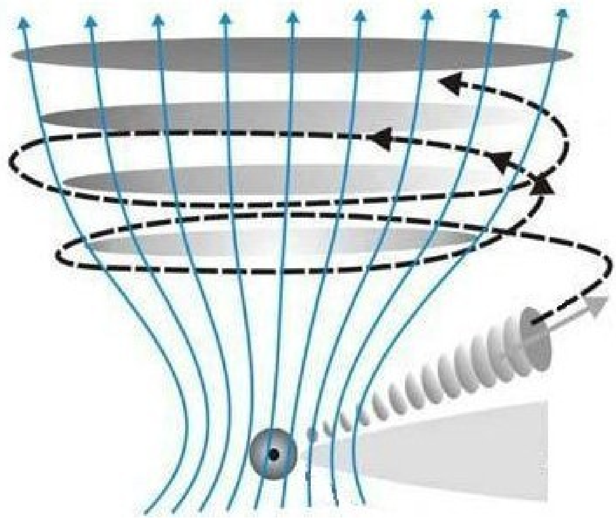

Figure 4.3: Collimation of the outflowing wind on large scales

An outflowing wind is launched in the transition layer. It advects a fraction of the toroidal magnetic field. At large radii the flow is no longer diffusive. The toroidal magnetic field exerts Lorentz-forces on the plasma and thus redirects the wind to form a collimated jet on large scales.
Credit: Hujeirat (2004)

Let us summarize the properties of the accretion flow in the close vicinity of the central object:

- large-scale, (super-) equipartition, poloidal magnetic fields that extract angular momentum on the dynamical time scale
- this implies sub-Keplerian rotation in the disk and an Ω-profile like the one depicted in Fig. 4.2
- a highly diffusive, geometrically thin, super-Keplerian rotating transition layer where outflows are launched

These properties are the foundation of the model. The subject of the next two sections will be to deliver an analytic description of it.

4.2 Preparations

In this section we will discuss two basic assumptions of the model, namely the radial profiles of the poloidal magnetic field (B^r, B^θ) and the angular velocity Ω. First we have to make some useful definitions, though.
Let H_d be the disk half thickness. At larger radii, the accretion disk is well described by a standard α-disk. Interior to a transition radius r_{tr} the accretion flow changes corresponding to the model described in Section 4.1. In the standard disk model we had $H_{sd} \propto r^{\frac{9}{8}} \approx r$ for the outer solution, $H_{sd} \propto r^{\frac{21}{20}} \approx r$ for the middle solution and $H_{sd} \approx const.$ for the inner solution (see Section 2.2). Since we stay close to the central object, we can safely set $H_d \propto r$. If the inner solution does not exist this will surely be justified. However, $H_d \propto r$ appears to be a reasonable continuation even if the inner solution does exist since, due to the

lack of viscous dissipation, the disk will be colder and therefore thinner than a standard disk.
Let H_w be the thickness of the transition layer (TL). We define H_d and H_w via:

$$
\begin{aligned}
H_d &= r \sin\theta_d \approx \theta_d \, r && (4.1)\\
H_w &= r\left(\sin\theta_w(r) - \sin\theta_d\right) \approx \left(\theta_w(r) - \theta_d\right) r := \delta\theta(r)\, r, && (4.2)
\end{aligned}
$$

where θ_d is a constant while θ_w is an unspecified function of r. Both the disk as well as the TL are assumed to be geometrically thin, i.e. $H_{d/w} \ll r$. Analogous to the Newtonian case we define the surface densities Σ_d and Σ_w

$$
\begin{aligned}
\Sigma_d &= \int\limits_{\frac{\pi}{2}-\theta_d}^{\frac{\pi}{2}+\theta_d} e^2 \rho \approx \int\limits_{\frac{\pi}{2}-\theta_d}^{\frac{\pi}{2}+\theta_d} d\theta \, r\rho \approx 2H_d\rho && (4.3)\\
\Sigma_w &= \int\limits_{\frac{\pi}{2}+\theta_d}^{\frac{\pi}{2}+\theta_w} e^2 \rho \approx \left(\theta_w - \theta_d\right) r\rho \approx H_w \rho && (4.4)
\end{aligned}
$$

and mass averaged radial velocities

$$
\begin{aligned}
< \gamma v^r >_d &= \frac{1}{\Sigma_d} \int\limits_{\frac{\pi}{2}-\theta_d}^{\frac{\pi}{2}+\theta_d} e^2 \rho\gamma v^r \approx \frac{1}{\Sigma_d} \int\limits_{\frac{\pi}{2}-\theta_d}^{\frac{\pi}{2}+\theta_d} d\theta \, r\rho\gamma v^r \approx \gamma_d v_d^r && (4.5)\\
< \gamma v^r >_w &= \frac{1}{\Sigma_w} \int\limits_{\frac{\pi}{2}+\theta_d}^{\frac{\pi}{2}+\theta_w} e^2 \rho\gamma v^r \approx \gamma_w v_w^r. && (4.6)
\end{aligned}
$$

Next we turn to the continuity equation to derive the accretion rate $\dot{M}$:

$$
0 = \partial_t \left(\rho \frac{\gamma}{\alpha}\right) + \frac{1}{r^2} \partial_r \left(r\sqrt{\Delta}\rho\gamma v^r\right) + \frac{1}{r} \partial_\theta \left(\rho\gamma v^\theta\right). \quad (4.7)
$$

We will now integrate over the three-dimensional hypersurface that makes up the accretion disk while averaging over an infinitesimal time slice δt, i.e. we act on (4.7) with the operator:

$$
\frac{1}{\delta t} \int\limits_{t}^{t+\delta t} dt \int\limits_{Disk} dr d\theta d\varphi \sqrt{|g|}, \quad (4.8)
$$

where δt is chosen such that it is smaller than the time scale for relevant changes in the mass-accretion rate[1]. This allows us to approximate that

$$\frac{1}{\delta t}\int\limits_t^{t+\delta t} dt \approx 1 \quad \text{and hence} \quad \frac{1}{\delta t}\int\limits_t^{t+\delta t} dt\, \partial_t \approx \partial_t. \tag{4.9}$$

Defining the total mass inside a given three-dimensional, spacelike hypersurface V, averaged of the time slice δt, by

$$M := \frac{1}{\delta t}\int\limits_t^{t+\delta t} dt \int\limits_V drd\theta d\varphi\, r^2\, \rho\frac{\gamma}{\alpha}, \tag{4.10}$$

we obtain from (4.7):

$$\begin{aligned} 0 &= \frac{1}{\delta t}\int\limits_t^{t+\delta t} dt \int\limits_{Disk} drd\theta d\varphi\, r^2 \left(\partial_t\left(\rho\frac{\gamma}{\alpha}\right) + \frac{1}{r^2}\partial_r\left(r\sqrt{\Delta}\rho\gamma v^r\right) + \frac{1}{r}\partial_\theta\left(\rho\gamma v^\theta\right)\right) \\ &\approx \underbrace{\partial_t M}_{=:\dot{M}} + 2\pi \int\limits_{\frac{\pi}{2}-\theta_d}^{\frac{\pi}{2}+\theta_d} d\theta\, r\sqrt{\Delta}\rho\gamma v^r + 4\pi\int^r dr\, r\rho\gamma v^\theta\Big|_{\theta=\frac{\pi}{2}+\theta_d} \qquad (4.11) \\ \Leftrightarrow \dot{M} &\approx \underbrace{-2\pi\sqrt{\Delta}\Sigma_d < \gamma v^r >_d}_{=\dot{M}_d} \underbrace{-4\pi\int^r dr\, r\rho_d\gamma_d v^\theta}_{=2\dot{M}_w}, \qquad (4.12) \end{aligned}$$

In the second term of the last line we have approximated ρ and γ by their the disk-average. Further, v^θ corresponds to the vertical drift at the interface between the disk and the TL ($\theta = \pi/2 \pm \theta_d$). We arrive at an expression for the total (constant) accretion rate in terms of the accreting mass flux within the disk and the outflowing wind in the TL above and below:

$$\dot{M} = \dot{M}_d + 2\dot{M}_w = const. \tag{4.13}$$

The wind in the TL is also in the radial direction. Hence, we can find a more simple expression for $\dot{M}_w$ in terms of the radial velocity and surface density in the TL:

$$\begin{aligned} \dot{M}_d &= -2\pi\sqrt{\Delta}\Sigma_d < \gamma v^r >_d \qquad (4.14) \\ \dot{M}_w &= -2\pi\sqrt{\Delta}\Sigma_w < \gamma v^r >_w . \qquad (4.15) \end{aligned}$$

[1]This averaging process is necessary, since $\sqrt{|g|} = r^2$ for a four-dimensional spacetime volume element but $\sqrt{|g|} = r^2/\alpha$ for a three-dimensional, spacelike hypersurface.

Now we turn to the basic assumptions that Hujeirat made for his Newtonian model. The first assumption is that the ideal MHD approximation holds inside the accretion disk. In this case, the poloidal induction equations reduce to:

$$\begin{aligned} 0 &= \partial_\theta \left(\varpi\gamma v^r B^\theta\right) && (4.16)\\ 0 &= -\partial_r \left(\varpi\gamma v^r B^\theta\right). && (4.17)\end{aligned}$$

Hence, we have found the conserved quantity:

$$\varpi\gamma v^r B^\theta =: \mathcal{B}_0 = const. \tag{4.18}$$

Correspondingly, we can derive the profile of B^θ:

$$B^\theta = \frac{\mathcal{B}_0}{\varpi\gamma v^r}\ , \quad \text{where} \ \ \mathcal{B}_0 = \varpi\gamma v^r B^\theta\big|_{r=r_{tr}}\ . \tag{4.19}$$

Thermal equipartition of the poloidal magnetic field at r_{tr} serves as boundary condition:

$$B^\theta(r_{tr}) = \sqrt{f\mu_0 \frac{k}{\mu m_p}\rho_{sd}(r_{tr})T_{sd}(r_{tr})} \tag{4.20}$$

where f is the number of degrees of freedom and μ the mean molecular weight of the plasma particles. $\rho_{sd}(r_{tr})$, $T_{sd}(r_{tr})$ correspond to the values of density and temperature of the standard disk at r_{tr}.
The radial component B^r can be derived by means of the vanishing divergence of the magnetic field (3.66):

$$\partial_r \left(r\varpi B^r\right) + \partial_\theta \left(\frac{r}{\alpha}B^\theta\right) = 0. \tag{4.21}$$

Integrating over r yields:

$$r\varpi B^r = -\int_{r_{tr}}^{r} dr\, \frac{r}{\alpha}\partial_\theta B^\theta, \tag{4.22}$$

where we have assumed that the poloidal field is vertical in the beginning: $B^r_{tr} = 0$. The poloidal field is dominated by B^θ in the disk whereas it is predominantly radial in the TL. However, the detailed profile is of B^r is not going to be important for the model, since B^φ is the most dominant magnetic field component in the TL (see Section 4.3). Hence, it suffices to make a crude approximation for B^r:

$$B^r \approx \frac{1}{r\varpi}\left(\frac{r}{H_d}\right)^2 \left(\theta - \frac{\pi}{2}\right)\left(\frac{{r_{tr}}^2}{\alpha_{tr}}B^\theta_{tr} - \frac{r^2}{\alpha}B^\theta\right). \tag{4.23}$$

The second assumption that Hujeirat made was that, considering that Alfvén waves remove angular momentum from the disk on the dynamical time scale, the disk matter can not maintain Keplerian rotation. Interior to r_{tr} strong, large-scale, poloidal magnetic fields will cause a significant deviation from the standard disk and force the matter to rotate sub-Keplerian. For the angular velocity he adopted the power law:

$$\Omega = \Omega_{K,tr} \left(\frac{r}{r_{tr}}\right)^{-\frac{5}{4}}, \tag{4.24}$$

where the Keplerian angular velocity at the transition radius $\Omega_{K,tr}$ serves as boundary condition. In the case of a Schwarzschild black hole we can just mimic this procedure. For a Kerr black hole, however, we will have to find a suitable generalization of (4.24). There is in principle an infinite set of profiles that meet this requirement. In the following we will consider the accretion flow to be in co-rotation with the black hole since then the radius of marginal stability moves closer to the event horizon giving rise to more energetic outflows. The modification to a flow in counter-rotation is very straight forward, though. We quote three very straight forward possibilities:

$$\Omega_1 = \frac{\sqrt{GM}}{r^{\frac{5}{4}} {r_{tr}}^{\frac{1}{4}} + {r_g}^{\frac{3}{2}} a} \tag{4.25}$$

$$\Omega_2 = \Omega_K \left(\frac{r}{r_{tr}}\right)^{\frac{1}{4}} \tag{4.26}$$

$$\Omega_3 = \Omega_K(r_{tr}) \left(\frac{r}{r_{tr}}\right)^{-\frac{5}{4}}. \tag{4.27}$$

All three versions satisfy $\Omega(r_{tr}) = \Omega_K(r_{tr})$, where Ω_K corresponds to the Keplerian angular velocity for co-rotating (direct) orbits:

$$\Omega_K = \frac{\sqrt{GM}}{r^{\frac{3}{2}} + {r_g}^{\frac{3}{2}} a}. \tag{4.28}$$

In the TL the matter is supplied with rotational energy from the disk and starts rotating with super-Keplerian angular velocity adopting the same radial profile as in the disk. At the inner boundary r_B of the TL centrifugal and gravitational acceleration are balanced and the effective gravity vanishes. As a result the matter will rotate with the Keplerian angular velocity at this point: $\Omega(r_B) = \Omega_K(r_B)$. This allows us to discard (4.27) since it becomes sub-Keplerian for fast rotating black holes and small r (see Fig. 4.4).

The relative difference between (4.25) and (4.26) peaks at 5% for $a = 1$ and $r_B = r_{ms}$ in the TL and diverges in the limit $r \to 0$ in the disk. 10% deviation are obtained for $r = 2.5\, r_g$ for a maximally rotating black hole and $r_{tr} = 40\, r_g$. The deviation decreases rapidly for deacresing a. Hence, we have free choice between (4.25) and (4.26) for slowly rotating black holes.

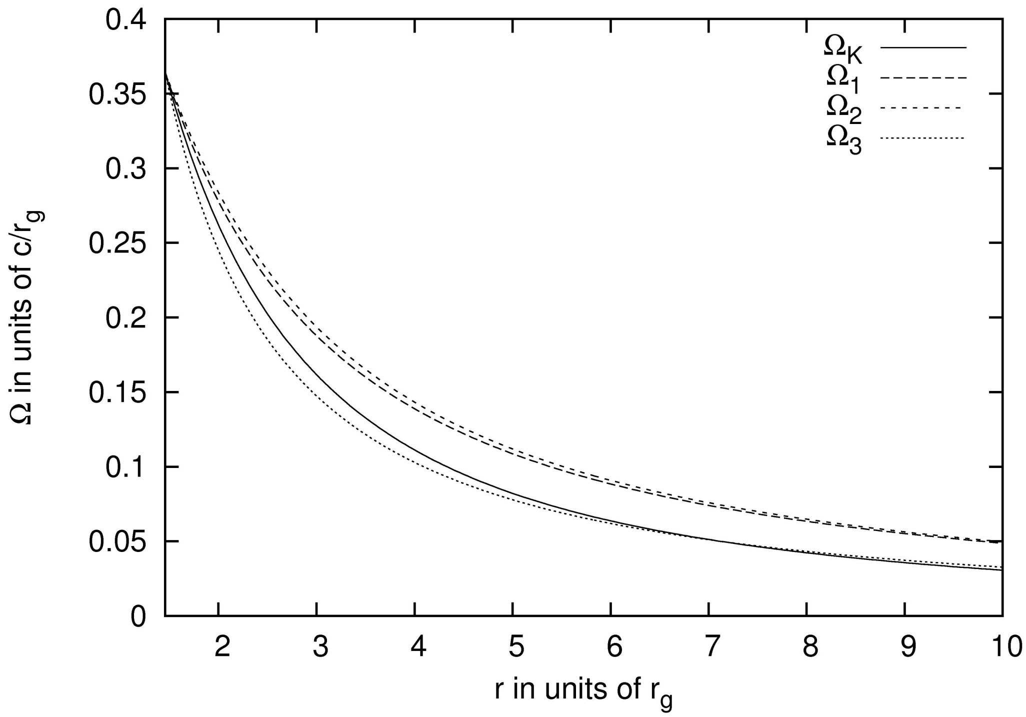

Figure 4.4: The three possible profiles for Ω from equations (4.25)-(4.27)

The profiles are plotted for the TL, using $a = 0.99$ and $r_B = r_{ms}$, where r_{ms} is the marginally stable orbit. One can see that Ω_3 is sub-Keplerian for small r. The deviation between Ω_1 and Ω_2 is below 10% for most of the parameter space.

For fast rotating black holes, on the other hand, we note that the Boyer-Lindquist-coordinate frame is a static frame describing a stationary spacetime that rotates with angular velocity ω. As a consequence freely falling matter is rotating with ω relative to the coordinate frame. A ZAMO measures then the angular velocity:

$$\tilde{\Omega} = \Omega - \omega. \tag{4.29}$$

For large a there will be a radius r_* where the matter is non-rotating with respect to ZAMO:

$$\Omega(r_*) = \omega(r_*) \quad \Leftrightarrow \quad \tilde{\Omega}(r_*) = 0, \tag{4.30}$$

i.e. r_* is the largest, rational root of the equation:

$$\frac{r^2}{{r_g}^2} + a^2 - 2a\left(\frac{r_{tr}r}{{r_g}^2}\right)^{\frac{1}{4}} = \begin{cases} 0 & \text{, if } \ \Omega = \Omega_1 \\ \frac{2r_g a^2}{r}\left(\left(\frac{r_{tr}}{r}\right)^{\frac{1}{4}} - 1\right) & \text{, if } \ \Omega = \Omega_2. \end{cases} \tag{4.31}$$

Our assumption is that, interior to r_*, the matter is in free fall:

$$\Omega \equiv \omega \quad \text{for} \quad r \leq r_*. \tag{4.32}$$

This means that the disk matter keeps rotating with the frame-dragging frequency ω, relative to the coordinate frame, while Alfvén waves are still extracting angular momentum. The rotational energy, powering the jet, is then extracted directly from the central black hole. Yet, the total energy extracted in this way will be negligible compared to the total rotational energy of the black hole so no spin-down is taken into account. Instead we treat the frame-dragging potential as an infinite reservoir of rotational energy.
r_* increases with increasing a and r_{tr}: If $r_{tr} = 40\,r_g$, the radius r_* is located in the immediate vicinity of the event horizon for $a = 0.6$ and it equals $2.3\,r_g$ and $2.5\,r_g$ for Ω_1 and Ω_2, respectively, for a maximally rotating black hole. For $r_{tr} = 400\,r_g$, $a = 1$ it is roughly equal to $3.3\,r_g$ and $3.6\,r_g$, respectively. In this case, the point of 10% percent deviation between (4.25) and (4.26) is also located at $3.3\,r_g$. Hence, we conclude that for $r \geq r_*$ we have free choice between (4.25) and (4.26) for fast rotating black holes as well.
We choose (4.25), since it appears to be the most reasonable profile. To sum up, we quote the angular velocity for the disk and the transition layer:

$$\Omega_d = \begin{cases} \Omega_K & r_{tr} \leq r \\ \sqrt{GM}\left(r^{\frac{5}{4}} {r_{tr}}^{\frac{1}{4}} + {r_g}^{\frac{3}{2}} a\right)^{-1} & r_* \leq r \leq r_{tr} \\ \omega & r \leq r_* \end{cases} \tag{4.33}$$

$$\Omega_w = \sqrt{GM}\left(r^{\frac{5}{4}} {r_B}^{\frac{1}{4}} + {r_g}^{\frac{3}{2}} a\right)^{-1} \qquad r_B \leq r. \tag{4.34}$$

4.3 Constructing the Combined Solution

We have collected everything we need in order elaborate a quantitative formulation of the model. The aim of this section is to find a solution that describes both the disk and the TL in the vicinity of the central object.
We will proceed in the following four steps to keep things as neat as possible:

- the radial momentum equation
- the continuity- and angular momentum equation
- the vertical momentum equation
- the energy equations

We will derive the profiles of the radial velocity in the first step and the profiles of the toroidal magnetic field, density and vertical drift velocity in the second step. Step three is dedicated to the vertical structure of the TL. We will inspect the geometrical thickness and the magnetic diffusivity. In step four we derive the profiles of temperature. The discussion and application of the solution is dedicated to Chapter 5.

All equations are constrained by the induction equations, of course. The radial momentum equation will be the only serious differential equation to solve. All other equations will be merely a matter of algebraic manipulation.

4.3.1 The Radial Momentum Equation

The radial momentum equation was presented in Section 3.56, page 55. For convenience we quote it again:

$$\begin{aligned}
\rho\gamma v^r \partial_r \left(\gamma v^r\right) &= -\partial_r P + \frac{1}{2}\rho\left\{c^2\dot{t}^2\partial_r g_{tt} + 2c\dot{t}\dot{\varphi}\partial_r g_{t\varphi} + \dot{\varphi}^2\partial_r g_{\varphi\varphi}\right\} - \\
&\quad - \frac{B^\varphi}{\mu_0\sqrt{\Delta}}\partial_r\left(\sqrt{\Delta}B^\varphi\right) - \frac{B^\theta}{\mu_0\sqrt{\Delta}}\partial_\theta\left(\frac{\omega\varpi}{\alpha c^2}E^\theta - B^r\right) - \\
&\quad - \frac{B^\theta}{\mu_0\alpha r}\partial_r\left(\frac{r\omega\varpi}{c^2}E^r + \frac{r}{\alpha}B^\theta\right) + \\
&\quad + \frac{1}{\mu_0 c^2}\left(E^r + \frac{\omega\varpi}{\alpha}B^\theta\right)\left(\frac{1}{r\varpi}\partial_r\left(r\varpi E^r\right) + \frac{1}{\sqrt{\Delta}}\partial_\theta E^\theta\right).
\end{aligned} \tag{4.35}$$

First we observe that the flow is highly super-sonic. As a consequence we can drop the $\partial_r P$-term since it is of order $\rho {c_S}^2/r$. Next we show that B^θ and B^φ are the most dominant components of the electromagnetic field in the disk and in the TL, respectively:
According to (3.64) and (3.65) the electric field components are of the order

$$E^r \approx v^\varphi B^\theta + v^{tur} B^\varphi \tag{4.36}$$

$$E^\theta \approx v^r B^\varphi - v^\varphi B^r + \frac{H_w}{r}\frac{\sqrt{\Delta}}{r} v^{tur} B^\varphi, \tag{4.37}$$

where we have approximated $\eta_M \approx H_w \gamma v_{tur}$ with H_w the typical vertical length-scale and v_{tur} the typical velocity of turbulent motion due to reconnection in the TL.
The last two terms in both expressions can be neglected within the disk (ideal MHD). B^φ is a small quantity there regarding the small vertical gradient of Ω in the equatorial plane (see Section 4.1, page 61). The poloidal magnetic field is dominated by B^θ. All contributions from electric fields in (4.35) are accompanied with a factor c^{-2}. Therefore it is save to say that $E^r/c^2 \approx v^\varphi B^\theta/c^2 \ll B^\theta$, rendering terms containing E^r negligible. We can neglect E^θ as well, since B^r is supposed to vanish in the equatorial plane anyway.
In the TL we have the additional contribution of the diffusive terms. Yet, the same argument is valid for the disk, namely that $E^r/c^2 \approx v^{tur} B^\varphi/c^2 \ll B^\varphi$ and analogous for E^θ. In the TL the poloidal field is supposed to be predominantly radial. Yet, B^φ will be the strongest magnetic field component due to the steep vertical gradient of Ω.

Thus we drop all electromagnetic terms that do not contain B^θ or B^φ if we do calculations in the disk or TL, respectively.
Inside the disk Alfvén waves transport angular momentum along the poloidal magnetic field lines on the dynamical time scale, i.e.:

$$t_{dyn} = \frac{r}{v_d^\varphi} = \frac{H_d}{v_A} = t_A \tag{4.38}$$

$$\Rightarrow v_A = \frac{H_d}{r} v_d^\varphi \ll v_d^\varphi, \tag{4.39}$$

where v_A is the Alfén speed and t_A is the time scale for vertical propagation of Alfén waves. In non-relativistic MHD we have $v_A := B^2/\sqrt{\mu_0 \rho}$. Gedalin (1993) has derived the corresponding relativistic formula:

$$v_A{}^2 = \frac{\frac{B^2}{\mu_0}}{\rho\mathcal{H} + \frac{B^2}{\mu_0}} \tag{4.40}$$

$$\Leftrightarrow \gamma_A{}^2 v_A{}^2 = \frac{B^2}{\mu_0 \rho \mathcal{H}}, \quad \text{where } \gamma_A := \frac{1}{\sqrt{1 - \frac{v_A{}^2}{c^2}}}. \tag{4.41}$$

In the disk we can approximate this by:

$$\gamma_A{}^2 v_A{}^2 \approx \frac{B^{\theta 2}}{\mu_0 \rho_d}. \tag{4.42}$$

Inserting (4.39) yields:

$$\frac{B^\theta}{\mu_0 \rho_d} = \frac{\left(\frac{H_d}{r}\right)^2 v^{\varphi 2}}{1 - \left(\frac{H_d}{r}\right)^2 \frac{v^{\varphi 2}}{c^2}} \ll v^{\varphi 2}. \tag{4.43}$$

The braces in (4.35) contain terms of order $v^{\varphi 2}$. Hence, we can neglect all electromagnetic terms on the right-hand side within the disk region.
We turn to the TL: the most dominant field component is B^φ. Thus we drop all terms that do not contain B^φ. Concerning the toroidal magnetic field we observe that the stationarity condition in the TL requires $\gamma_A v_A^\varphi = \gamma_w v_w^\varphi \gg v_{esc}$ (Hujeirat, 2004). Yet, the toroidal field is unlikely to be the main driving force since it has turning points in its vertical profile. The centrifugal and gravitational forces on the other hand remain strong throughout the disk and the TL. So we drop the toroidal field-term as well. Again we have only acceleration terms due to gravity and centrifugal forces left on the right-hand side of (4.35). We make use of the definitions (3.54) to write:

$$\begin{aligned} \dot{t} &= \frac{\gamma}{\alpha} \\ \dot{r} &= \frac{\sqrt{\Delta}}{r} \gamma v^r \\ \dot{\varphi} &= \frac{\gamma}{\alpha} \Omega. \end{aligned} \tag{4.44}$$

Inserting into (4.35) and rewriting yields:

$$\partial_r \left(\gamma v^r\right)^2 = \frac{\gamma^2}{\alpha^2}\left(c^2\partial_r g_{tt} + 2c\Omega\partial_r g_{t\varphi} + \Omega^2\partial_r g_{\varphi\varphi}\right). \tag{4.45}$$

Regarding further that $g_{t\varphi} = -\omega g_{\varphi\varphi}/c$ and $g_{tt}g_{\varphi\varphi} - g_{t\varphi}^2 = -\Delta$ we obtain:

$$\partial_r \left(\gamma v^r\right)^2 = \frac{\gamma^2}{\alpha^2}\left(-c^2\partial_r\alpha^2 - 2\tilde{\Omega}\varpi^2\partial_r\omega + \tilde{\Omega}^2\partial_r\varpi^2\right), \tag{4.46}$$

where $\tilde{\Omega} = \Omega - \omega$ is the angular velocity that a ZAMO measures.
We note that

$$\begin{aligned}\partial_r v^{\varphi 2} \quad &= \quad \frac{1}{\alpha^2}\left(-c^2\partial_r\alpha^2 - 2\tilde{\Omega}\varpi^2\partial_r\omega + \tilde{\Omega}^2\partial_r\varpi^2\right) + \\ &\quad + 2v^{\varphi 2}\frac{\partial_r\Omega}{\tilde{\Omega}} + \left(c^2 - v^{\varphi 2}\right)\partial_r \ln\alpha^2. \end{aligned} \tag{4.47}$$

Inserting this expression into (4.46) and writing out the γ-factors explicitly yields:

$$\partial_r \frac{v^{r2}}{c^2 - v^{r2} - v^{\varphi 2}} = \frac{\partial_r v^{\varphi 2} - 2v^{\varphi 2}\frac{\partial_r\Omega}{\tilde{\Omega}} - \left(c^2 - v^{\varphi 2}\right)\partial_r\ln\alpha^2}{c^2 - v^{r2} - v^{\varphi 2}}. \tag{4.48}$$

We can further rewrite this equation to obtain a more convenient expression:

$$\begin{aligned}\partial_r v^{r2} \quad &= \quad v^{r2}\left(\frac{-2\partial_r v^{\varphi 2} + 2v^{\varphi 2}\frac{\partial_r\Omega}{\tilde{\Omega}}}{c^2 - v^{\varphi 2}} + \partial_r\ln\alpha^2\right) + \\ &\quad + \partial_r v^{\varphi 2} - 2v^{\varphi 2}\frac{\partial_r\Omega}{\tilde{\Omega}} - \left(c^2 - v^{\varphi 2}\right)\partial_r\ln\alpha^2. \end{aligned} \tag{4.49}$$

Thus we have obtained a first order ordinary differential equation for v^{r2}. We define the auxiliary function $\mathcal{F}$ by:

$$\partial_r \ln\mathcal{F} = \frac{2v^{\varphi 2}\frac{\partial_r\Omega}{\tilde{\Omega}}}{c^2 - v^{\varphi 2}}. \tag{4.50}$$

Now we can rewrite (4.49) to yield:

$$\partial_r v^{r2} = v^{r2}\partial_r\ln\left(\alpha^2\mathcal{F}\left(1 - \frac{v^{\varphi 2}}{c^2}\right)^2\right) - \left(c^2 - v^{\varphi 2}\right)\partial_r\ln\left(\alpha^2\mathcal{F}\left(1 - \frac{v^{\varphi 2}}{c^2}\right)\right). \tag{4.51}$$

Normalizing the function $\mathcal{F}$ by $\mathcal{F}_0 = 1$, where the index "0" indicates that the quantity is to be taken at radius $r_0 = r_{tr/B}$ in the disk or TL, respectively, we obtain the general solution for v^{r2}:

$$v^{r2} = c^2 - v^{\varphi 2} - \frac{c^2}{\gamma_0^2}\frac{\alpha^2}{\alpha_0^2}\mathcal{F}\left(\frac{c^2 - v^{\varphi 2}}{c^2 - v_0^{\varphi 2}}\right)^2. \tag{4.52}$$

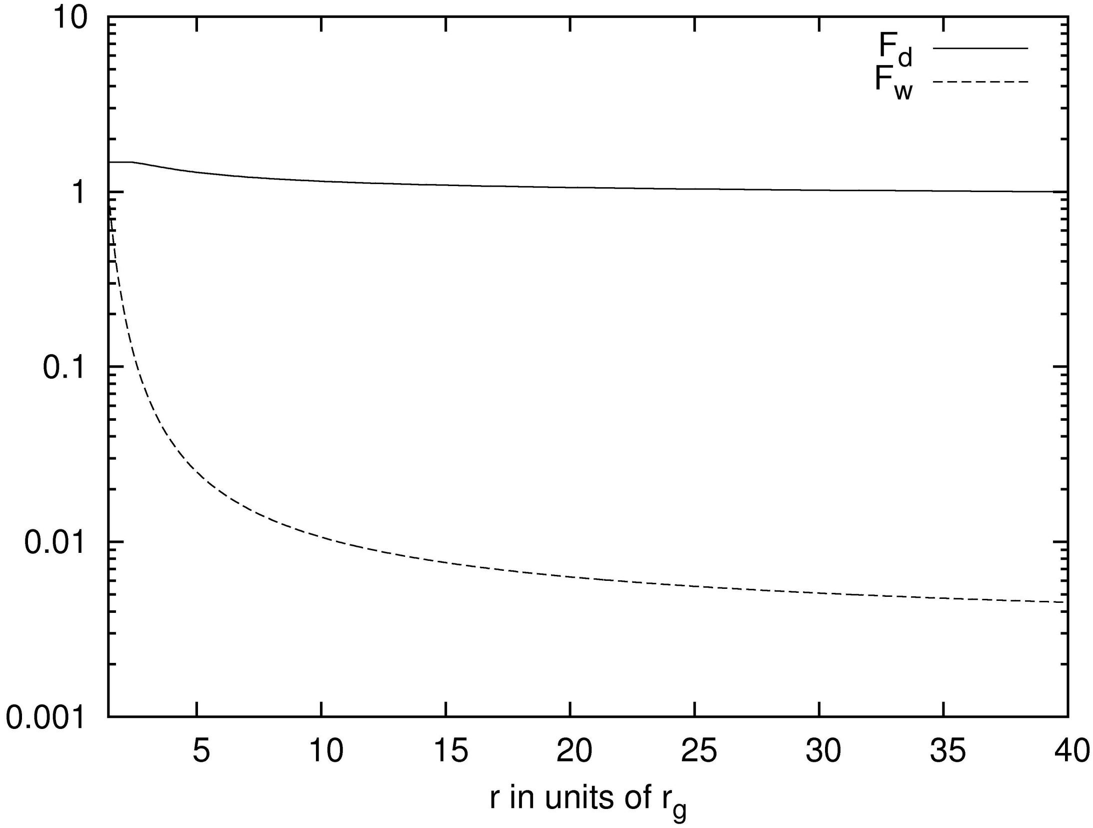

Figure 4.5: $\mathcal{F}_d$ and $\mathcal{F}_w$ for $a = 0.998$ and $r_{tr} = 40\, r_g$

In the disk $\mathcal{F}_d$ is always of order unity for reasonable parameter values while $\mathcal{F}_w$ can even reach $10^{-3} - 10^{-4}$ for very rapidly rotating black holes ($a \approx 0.998$).

Thus, (4.49) is solved, once we have found the solution for $\mathcal{F}$. In terms of the variable $y = (r/r_g)^{\frac{1}{4}}$, (4.50) can be expressed as

$$\partial_y \ln \mathcal{F} = -\frac{10}{{y_0}^2} \cdot \frac{1}{y} \cdot \frac{1}{y^5 + a{y_0}^{-1}} \cdot \frac{y^8 - 2ay_0 y + a^2}{y^5 - {y_0}^{-2} y^3 - 2y + 2a{y_0}^{-1}}. \tag{4.53}$$

Making use of the identity

$$\prod_{i=1}^{n} \frac{1}{y - y_i} = \sum_{i=1}^{n} \frac{1}{y - y_i} \prod_{\substack{j=1 \\ i \neq j}}^{n} \frac{1}{y_i - y_j}, \tag{4.54}$$

(4.53) can be readily integrated once the roots y_i of the polynomials in the denominator are known. In the case of a Schwarzschild black hole ($a = 0$), the full analytic solution to (4.53) is relatively simple[2]:

$$\mathcal{F} = \left(\frac{2y^2{y_0}^2 - 1 + \sqrt{1+8{y_0}^4}}{2{y_0}^4 - 1 + \sqrt{1+8{y_0}^4}} \cdot \frac{2{y_0}^4 - 1 - \sqrt{1+8{y_0}^4}}{2y^2{y_0}^2 - 1 - \sqrt{1+8{y_0}^4}} \right)^{\frac{5}{\sqrt{1+8{y_0}^4}}} . \qquad (4.56)$$

For $a \neq 0$ we obtain:

$$\begin{aligned} \mathcal{F} &= \exp\Bigg[-\frac{10}{{y_0}^2} \sum_{i=1}^{10} \prod_{\substack{j=1\\ i\neq j}}^{10} \frac{1}{y_i - y_j} \cdot \qquad (4.57) \\ &\cdot \left(\sum_{k=1}^{7} \frac{y^k - {y_0}^k}{k} {y_i}^{7-k} + \left({y_i}^7 - 2ay_0 + \frac{a^2}{y_0} \right) \ln \frac{y - y_i}{y_0 - y_i} - \frac{a^2}{y_i} \ln \frac{y}{y_0} \right) \Bigg], \end{aligned}$$

where y_1, y_2, y_3 are the three real roots of the equation

$$y^5 - {y_0}^{-2} y^3 - 2y + 2a{y_0}^{-1} = 0 \qquad (4.58)$$

and

$$\begin{aligned} y_4 &= -\frac{y_1 + y_2 + y_3}{2} + \sqrt{{y_0}^{-2} - \frac{{y_1}^2 + {y_2}^2 + {y_3}^2}{2} - \frac{(y_1 + y_2 + y_3)^2}{4}} \\ y_5 &= -\frac{y_1 + y_2 + y_3}{2} - \sqrt{{y_0}^{-2} - \frac{{y_1}^2 + {y_2}^2 + {y_3}^2}{2} - \frac{(y_1 + y_2 + y_3)^2}{4}} \\ y_n &= -\left(\frac{a}{y_0} \right)^{\frac{1}{5}} e^{2\pi i \frac{n}{5}} , \quad n \in \{6, 7, 8, 9, 10\}. \end{aligned} \qquad (4.59)$$

For all reasonable parameter values we have $y_1, y_2, y_3 \in [-2 : 1.5]$. There exist analytic expressions for the roots of (4.58). In all cases where $a \neq 0$, however, these expressions are so complicated that the numerical calculation of y_1, y_2, y_3 appears to be the appropriate procedure.

In Section 4.2, page 68 we found that, inside the disk, the matter is in free fall interior to a radius r_* implying $\mathcal{F}_d = const.$ and $v_d^\varphi = 0$. The radial velocity then reduces to:

$${v_d^r}^2 = c^2 - \frac{c^2}{{\gamma_{d,tr}}^2} \frac{\alpha^2}{{\alpha_{tr}}^2} \mathcal{F}_{d,*} \left(1 - \frac{{v_{d,tr}^\varphi}^2}{c^2} \right)^{-2} . \qquad (4.60)$$

[2]Note: In the Newtonian limit we have

$$\partial_r \ln \mathcal{F} \approx \frac{5 \partial_r {v^\varphi}^2}{c^2 - {v^\varphi}^2} \quad \Rightarrow \quad \mathcal{F} \approx \left(\frac{1 - {v_0^\varphi}^2/c^2}{1 - {v^\varphi}^2/c^2} \right)^5 \approx \left(\frac{1 - {y_0}^{-4}}{1 - y^{-2}{y_0}^{-2}} \right)^5 . \qquad (4.55)$$

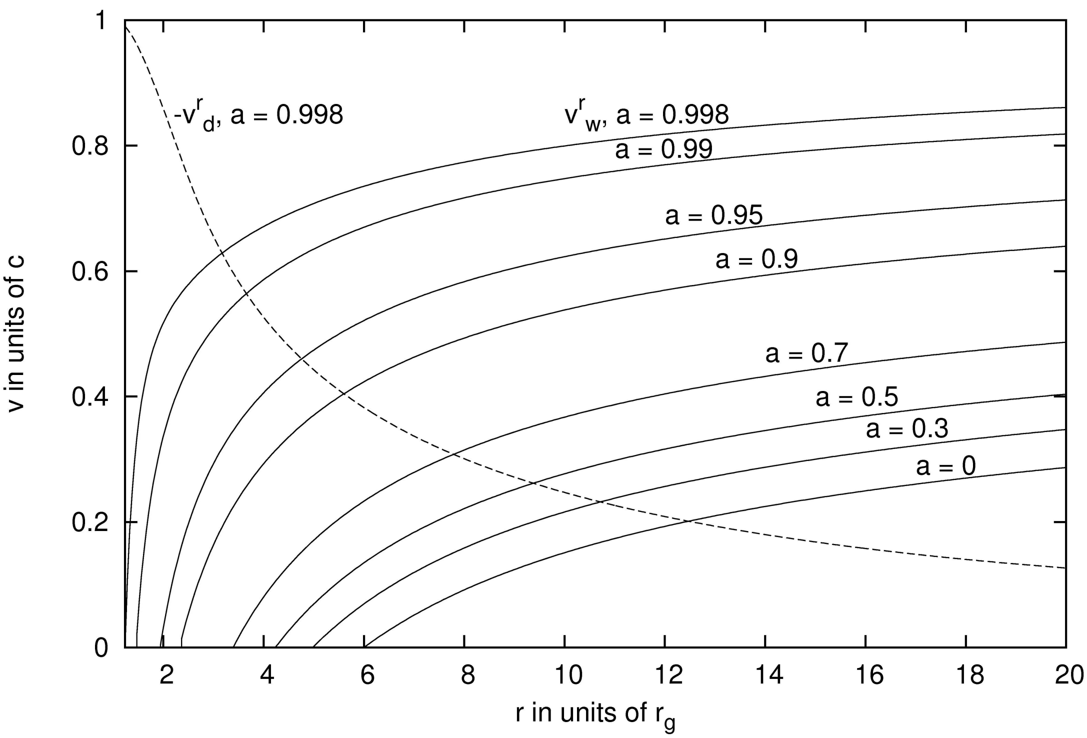

Figure 4.6: Profile of the radial velocity in the disk and in the TL

The radial velocity has been plotted for $r_{tr} = 40\,r_g$ and $r_B = r_{ms}$. In the disk the profile changes only very weakly with a except for the fact that, due to the decreasing event horizon, smaller radii can be reached. In the TL, on the other hand, the profile strongly depends on a since it determines the maximal depth of the potential well that matter can escape from.

4.3.2 Conservation of Mass and Angular Momentum

In the last subsection we have obtained profiles for the radial velocity in the disk and TL, respectively. These can now be used to derive the profiles of density and toroidal magnetic field from the continuity- and angular momentum equation, respectively. The former reads:

$$\frac{1}{r^2}\partial_r\left(r\rho\sqrt{\Delta}\gamma v^r\right) + \frac{1}{r}\partial_\theta\left(\rho\gamma v^\theta\right) = 0. \tag{4.61}$$

Acting with $\int_{\frac{\pi}{2}-\theta_d}^{\frac{\pi}{2}+\theta_d} d\theta\, r^2$ yields:

$$\partial_r\left(\Sigma_d < \gamma v^r >_d \sqrt{\Delta}\right) = -2r\rho\gamma v^\theta\Big|_{\theta=\frac{\pi}{2}+\theta_d} \approx -2r\rho_d\gamma_d v^\theta, \tag{4.62}$$

where we have approximated ρ and γ by their the disk-average. In this equation and in the following, v^θ corresponds to the vertical drift velocity at the disk surfaces, i.e. $\theta = \pi/2 \pm \theta_d$. By means of (4.13) and (4.14) we can write:

$$-\partial_r \dot{M}_d = 2\partial_r \dot{M}_w = -4\pi r \rho_d \gamma_d v_d^\theta. \tag{4.63}$$

Let us turn to the angular momentum equation for a moment:

$$\rho\gamma v^r \frac{\sqrt{\Delta}}{r}\partial_r l = \frac{\varpi}{\mu_0 r}\left(B^r \partial_r \sqrt{\Delta} + B^\theta \partial_\theta\right) B^\varphi. \tag{4.64}$$

l is the angular momentum per mass which is given by:

$$l = \dot{x}_\varphi = \varpi\gamma v^\varphi = \gamma\frac{\varpi^2}{\alpha}\tilde{\Omega}. \tag{4.65}$$

B^r is neglected since the dominant term on the right-hand side of (4.64) is the one containing B^θ (see Sections 4.1 and 4.3.1). Acting with $\int_{\frac{\pi}{2}-\theta_d}^{\frac{\pi}{2}+\theta_d} d\theta\, r^2$ yields:

$$-\frac{\dot{M}_d}{2\pi r}\partial_r l_d = \frac{2\varpi}{\mu_0}B^\theta B^\varphi. \tag{4.66}$$

We have made use of the fact that, within the disk, B^θ is nearly independent of θ on the right-hand side. In this equation and in the following, B^φ corresponds to the value of the toroidal field at the disk surfaces, i.e. $\theta = \pi/2 \pm \theta_d$ (we assume that B^φ is already very strong at this latitude). The solution for B^φ is:

$$\begin{aligned}
B^\varphi &= -\frac{3\mu_0}{16\pi}\frac{\dot{M}_d}{r^2\varpi}\frac{l_d}{B^\theta}\mathcal{L} = -\frac{3\mu_0}{16\pi}\frac{\dot{M}_d}{r^2}\frac{\gamma_d v_d^\varphi}{B^\theta}\mathcal{L}, && (4.67)\\
\mathcal{L} &= \frac{4}{3}\frac{1}{1-\frac{v_d^{\varphi 2}}{c^2}}\cdot\left[4\frac{r^2-\frac{r_g^3}{r}a^2}{\varpi^2} - 2\frac{r^2-rr_g}{\Delta} + \right.\\
&\left. +\tilde{\Omega}_d^{-1}\left(\omega\frac{3r^2+r_g^2a^2}{\varpi^2}\left(1+\frac{v_d^{\varphi 2}}{c^2}\right) - \frac{5}{4}r_{tr}{}^{\frac{1}{4}}r^{\frac{5}{4}}\frac{\Omega_d{}^2}{\sqrt{r_g}c}\right)\right]. && (4.68)
\end{aligned}$$

The next targets are the mass density in the disk, ρ_d, and in the transition layer, ρ_w. In the case of ρ_d we just have to rearrange (4.14) to obtain:

$$\rho_d = -\frac{\dot{M}_d}{4\pi H_d\sqrt{\Delta}\gamma_d v_d^r}. \tag{4.69}$$

For the density in the TL one can invoke the stationarity condition for the toroidal magnetic field:

$$\gamma_A v_A^\varphi = \frac{B_d^\varphi}{\sqrt{\mu_0\rho_w}} = \gamma_w v_w^\varphi \quad \Leftrightarrow \quad \rho_w = \frac{1}{\mu_0}\left(\frac{B_d^\varphi}{\gamma_w v_w^\varphi}\right)^2 \tag{4.70}$$

We can also provide another expression for ρ_w using (4.15): Integration over (4.63) from r_B to r and using $v_w^r(r_B) = 0$ yields:

$$\dot{M}_w = -\frac{1}{2}\left(\dot{M}_d - \dot{M}_d(r_B)\right). \tag{4.71}$$

Substituting into (4.15), our result for ρ_w becomes:

$$\rho_w = \frac{\dot{M}_d - \dot{M}_d(r_B)}{4\pi H_w\sqrt{\Delta}\gamma_w v_w^r}. \tag{4.72}$$

The next quantity that we want to analyze is the vertical drift velocity v^θ. Using (4.13), (4.14), (4.15) and (4.63) we obtain:

$$\begin{aligned} 2\pi r\rho_d\gamma_d v^\theta &= -\partial_r\dot{M}_w \\ &\approx -\frac{\dot{M}_w}{r} \\ &= 2\pi\frac{H_w}{r}\sqrt{\Delta}\rho_w\gamma_w v_w^r \\ \Leftrightarrow \quad v^\theta &= \frac{H_w}{r}\frac{\sqrt{\Delta}}{r}\frac{\rho_w}{\rho_d}\frac{\gamma_w v_w^r}{\gamma_d}. \end{aligned} \tag{4.73}$$

Furthermore we can use (4.69) and (4.72) to substitute ρ_d and $\dot{M}_d$, respectively, to obtain:

$$v^\theta = -\frac{H_d}{r}\frac{\sqrt{\Delta}}{r}v_d^r\frac{4\pi H_w\sqrt{\Delta}\rho_w\gamma_w v_w^r}{\dot{M}_d(r_B) + 4\pi H_w\sqrt{\Delta}\rho_w\gamma_w v_w^r}. \tag{4.74}$$

4.3.3 The Vertical Structure of the Transition Layer

In this subsection we will focus on the TL, where the plasma is subject to extensive centrifugal forces. Now we want to investigate what kind of forces are opposing this collapse and how we can determine the geometrical thickness of the TL form this. The vertical momentum equation contains all forces that let the TL collapse or blow up:

$$\begin{aligned} 0 \;=\;& -\partial_\theta P + \theta\gamma^2\rho\left(\frac{r_g^2 a^2}{r^2}v^{r\,2} - \frac{v^{\varphi 2}}{\mathcal{S}^2}\right) - \frac{B^\varphi}{\mu_0}\partial_\theta B^\varphi + \frac{B^r}{\mu_0}\partial_\theta\left(\frac{\omega\varpi}{\alpha c^2}E^\theta - B^r\right) + \\ & + \frac{\varpi}{\mu_0 r}B^r\partial_r\left(\frac{r\omega\varpi}{c^2}E^r + \frac{r}{\alpha}B^\theta\right) + \\ & + \frac{1}{\mu_0 c^2}\left(E^\theta - \frac{\omega\varpi}{\alpha}B^r\right)\left(\frac{\alpha}{r}\partial_r(r\varpi E^r) + \partial_\theta E^\theta\right), \end{aligned} \tag{4.75}$$

where the variable $\mathcal{S}$ was defined in (3.67). Looking at (4.75) reveals several forces that could possibly oppose collapse:

1. gas pressure $-\partial_\theta P_g/\rho$
2. turbulent pressure $-\partial_\theta P_{tur}/\rho$
3. magnetic pressure due to the toroidal magnetic field $-B^\varphi \partial_\theta \left(B^\varphi\right)/(\mu_0 \rho)$
4. pressure and tension due to the poloidal electromagnetic field

The gas pressure-term is of order ${c_S}^2$ and thus can be neglected compared to the centrifugal term that is of order $v_w^{\varphi 2}$: Already in the accretion disk the matter is supersonic, hence there is no chance that gas pressure could oppose the collapse of the super Keplerian transition layer.
B^φ is the most dominant electromagnetic field component in the TL (see Section 4.3.1). We neglect all other electromagnetic terms. Further, we can drop the v^{r2}-term compared to $v^{\varphi 2}$. v^r can become highly relativistic at several gravitational radii but the term is damped by a factor of order r^{-2} while $\mathcal{S} = O(1)$. Approximating ∂_θ by $-r/H_w$ and $\theta \approx H_w/r$, we rewrite (3.57) as:

$$\left(\frac{r}{H_w}\right)^2 \left(\frac{P_{tur}}{\rho_w} + \frac{B^{\varphi 2}}{2\mu_0 \rho_w}\right) = \gamma_w^2 \frac{v_w^{\varphi 2}}{\mathcal{S}^2}. \tag{4.76}$$

Of the two remaining terms on the left-hand side, P_{tur} is most likely responsible for opposing collapse. This is due to the fact that the toroidal magnetic field has a turning point in the TL and to the high reconnection rate that we expect to have there (Hujeirat, 2004). Writing $P_{tur}/\rho_w = {\gamma_w}^2 {v_{tur}}^2$, we then conclude that:

$$\frac{H_w}{r} = \frac{v_{tur}}{v_w^\varphi}\mathcal{S}. \tag{4.77}$$

This indicates that the TL is geometrically thin since it is unlikely that turbulent motion exceeds the Keplerian velocity. For the TL to be stationary, the amplification time scale t_{adv} has to equal the dissipation time scale t_{diss} due to reconnection. Inspecting (3.63) yields:

$$t_{amp} = \frac{H_w}{\alpha v_w^\varphi}\frac{B^\varphi}{B^\theta} \tag{4.78}$$

$$t_{diss} = {H_w}^2 \frac{\gamma_w}{\alpha \eta_M}. \tag{4.79}$$

Setting $t_{amp} = t_{diss}$ we obtain the following relation:

$$\frac{B^\theta}{B^\varphi} = \frac{\eta_M}{H_w \gamma_w v_w^\varphi}. \tag{4.80}$$

The magnetic diffusivity η_M, on the other hand, can be written as:

$$\eta_M = H_w v_{tur} \text{ (Newton)} \quad \rightarrow \quad H_w \gamma_w v_{tur} \text{ (General Relativity)}. \tag{4.81}$$

$$\overset{(4.77}{\Rightarrow} \eta_M = \frac{{H_w}^2}{r\mathcal{S}} \gamma_w v_w^\varphi. \tag{4.82}$$

Combining (4.80) and (4.82) yields:

$$\frac{B^\theta}{B^\varphi} = \frac{H_w}{r\mathcal{S}} \tag{4.83}$$

Thus we have connected the fraction B^θ/B^φ directly to the thickness of the TL. Since $B^\theta/B^\varphi \ll 1$, as can be estimated by comparing the Alfv́en velocities (see Section 4.3.1, page 71), we see that the TL is geometrically thin.

4.3.4 The Internal Energy

In this subsection we will derive the temperature profiles in the disk and TL from the energy equation. It has been stated by Hujeirat (2004) that electrons and ions have to be treated as a two-temperature flow in the TL. Due to the low density, the time scale for energy exchange is slow compared to the dynamical time scale. In the disk, on the other hand, the density is much higher implying effective energy exchange between electrons and ions. Hence, we will use a one-temperature description in the disk. The two equations of internal energy, (3.59) and (3.60), are replaced by one single equation:

$$\rho_d \gamma_d v_d^r \frac{\sqrt{\Delta}}{r} \partial_r \mathcal{E}_d = -\frac{P_d}{r^2} \partial_r \left(r\sqrt{\Delta}\gamma_d v_d^r \right) + \Lambda_{con} - \Lambda_{syn} - \Lambda_B - \Lambda_C. \tag{4.84}$$

The contribution of ohmic heating, Λ_{Ohm}, has been dropped since the plasma is non-resistive in the disk. The main heating sources are adiabatic compression and heat conduction. The electrons cool mainly by synchrotron emission. Due to the Coulomb coupling this will also cool the ions in the disk. We assume that heat conduction from the hot ions in the TL suffices to cover this loss of heat, i.e.

$$\Lambda_{con} - \Lambda_{syn} - \Lambda_B - \Lambda_C \approx -\Lambda_{con} + \Lambda_{syn} \approx 0. \tag{4.85}$$

Then the only remaining source of heat is adiabatic compression. We rewrite the internal energy per mass and pressure, respectively, as

$$\mathcal{E}_d = C_V T_d \tag{4.86}$$

$$P_d = (\Gamma - 1)\,\rho_d \mathcal{E}_d = (\Gamma - 1)\,\rho_d C_V T_d, \tag{4.87}$$

where Γ, C_V, T_d correspond to adiabatic index, specific heat per mass and disk temperature, respectively. Hence, we arrive at the differential equation:

$$\frac{\partial_r T_d}{T_d} = -\left(\Gamma - 1\right) \frac{\partial_r \left(r\sqrt{\Delta}\gamma_d v_d^r \right)}{r\sqrt{\Delta}\gamma_d . v_d^r} \tag{4.88}$$

Integrating (4.88) from r_{tr} to r leaves us with:

$$T_d = T_d(r_{tr}) \left(\sqrt{\frac{\Delta}{\Delta(r_{tr})}} \frac{r}{r_{tr}} \left| \frac{\gamma_d v_d^r}{\gamma_{d,tr} v_{d,tr}^r} \right| \right)^{1-\Gamma}. \tag{4.89}$$

Now we turn to the transition layer. The most dominant heating process there is ohmic heating due to the large magnetic diffusivity. Electrons cool very effectively by synchrotron emission. We will therefore equalize the corresponding heating and cooling rates and neglect all other terms:

$$0 = \Lambda_{Ohm} - \Lambda_{syn}. \tag{4.90}$$

Novikov and Thorne (1973) have derived a relativistic expression for the cooling rate by synchrotron emission:

$$\Lambda_{syn} = \Upsilon \frac{f_e \rho}{m_p} \left(\frac{kT}{m_e c^2} \right)^2 \frac{B^2}{m_e^2}, \tag{4.91}$$

where we have defined the constant $\Upsilon = 32\pi {\alpha_f}^2 \hbar^2/(\mu_0 c)$. α_f is the fine-structure constant and f_e is the fraction of unbound electrons to baryons. B is approximated by B^φ, the most dominant component of the magnetic field in the TL. The relativistic expression for the heating rate Λ_{Ohm} is given by (see Section 3.2):

$$\Lambda_{Ohm} = \mu_0 \eta_M j^\rho j_\rho. \tag{4.92}$$

Regarding the estimates we have made in Section 4.3.1 we can determine the dominant contributions to Λ_{Ohm} from equations (3.49) to (3.52). Using (4.36) and (4.37) we make the approximation:

$$\mu_0 j^t \approx \frac{1}{\alpha} \frac{v_w^r}{c} \frac{B^\varphi}{H_w} \tag{4.93}$$

$$\mu_0 j^r \approx \frac{\sqrt{\Delta}}{r} \frac{B^\varphi}{H_w} \tag{4.94}$$

$$\mu_0 j^\theta \approx -\frac{\sqrt{\Delta}}{r} \frac{B^\varphi}{r^2} \tag{4.95}$$

$$\mu_0 j^\varphi \approx \frac{1}{\alpha} \frac{\omega}{c} \frac{v_w^r}{c} \frac{B^\varphi}{H_w}. \tag{4.96}$$

Regarding that $H_w/r \ll 1$ the square ${\mu_0}^2 j^2$ becomes:

$$\begin{aligned} {\mu_0}^2 j^2 &= {\mu_0}^2 \left(g_{tt} {j^t}^2 + 2 g_{t\varphi} j^t j^\varphi + g_{\varphi\varphi} {j^\varphi}^2 + g_{rr} {j^r}^2 + g_{\theta\theta} {j^\theta}^2 \right) \\ &\approx \left(-\frac{{v_w^r}^2}{c^2} + 1 + \frac{\Delta}{r^2} \frac{{H_w}^2}{r^2} \right) \frac{B^{\varphi 2}}{{H_w}^2} \\ &\approx \left(1 - \frac{{v_w^r}^2}{c^2} \right) \frac{B^{\varphi 2}}{{H_w}^2}. \end{aligned} \tag{4.97}$$

Inserting (4.97) and (4.82) in (4.92) yields:

$$\Lambda_{Ohm} = \eta_M \left(1 - \frac{{v_w^r}^2}{c^2} \right) \frac{B^{\varphi 2}}{\mu_0 {H_w}^2} = \gamma_w v_w^\varphi \left(1 - \frac{{v_w^r}^2}{c^2} \right) \frac{B^{\varphi 2}}{\mu_0 r \mathcal{S}}. \tag{4.98}$$

This leads to the energy equation:

$$\gamma_w v_w^\varphi \left(1 - \frac{v_w^{r\,2}}{c^2}\right) \frac{B^{\varphi 2}}{\mu_0 r \mathcal{S}} = \Upsilon f_e \frac{\rho_w}{m_p} \left(\frac{kT_{e,w}}{m_e c^2}\right)^2 \left(\frac{B^\varphi}{m_e}\right)^2 \quad (4.99)$$

$$\Leftrightarrow \quad T_{e,w} = \frac{m_e c^2}{k} \sqrt{\frac{m_p m_e^2}{\Upsilon} \frac{1}{f_e} \frac{1}{r\mathcal{S}} \frac{{\gamma_w}^3 v_w^{\varphi 3}}{B^{\varphi 2}} \left(1 - \frac{v_w^{r\,2}}{c^2}\right)}. \quad (4.100)$$

Turbulent dissipation heats the ions and electrons equally (Hujeirat, 2004). In order to maintain stationarity, however, the toroidal magnetic field B^φ has to be advected on the same time scale it is dissipated into heat by reconnection. Writing the internal energy of the ions as

$$\mathcal{E}_i = C_V T_{i,w}, \quad (4.101)$$

we can now obtain typical heating time scales by setting $t_{heat} = \rho\mathcal{E}/\Lambda$. In the case of reconnection this yields:

$$t_{heat} = \frac{C_V \rho_w T_{i,w}}{\Lambda_{Ohm}}. \quad (4.102)$$

The advection time scale can be read off of (3.63):

$$t_{adv} = \frac{H_w}{\alpha v_w^\varphi} \frac{B^\varphi}{B^\theta}. \quad (4.103)$$

Inserting (4.83) into this equation yields:

$$t_{adv} = \frac{r\mathcal{S}}{\alpha v_w^\varphi}. \quad (4.104)$$

The ion temperature is then determined by:

$$t_{heat} = t_{adv} \quad \Leftrightarrow \quad \frac{C_V \rho_w T_{i,w}}{\Lambda_{Ohm}} = \frac{r\mathcal{S}}{\alpha v_w^\varphi}. \quad (4.105)$$

Substituting Λ_{Ohm} and rearranging yields:

$$T_{i,w} = \frac{{\gamma_w}^3 v_w^{\varphi 2}}{C_V \alpha} \left(1 - \frac{v_w^{r\,2}}{c^2}\right). \quad (4.106)$$

Now we have accomplished the aim of this chapter. In the last sections, we derived profiles for the ten variables ρ_d, ρ_w, v_d^r, v_w^r, v^θ, B^φ, η_M, T_d, $T_{e,w}$ and $T_{i,w}$. In the next chapter we will recapitulate the results, we have just obtained, and bring them into a form that is more convenient for later use. We will give a discussion of the properties of this solution and apply it to the μQuasar GRS1915+105.

Chapter 5

Discussion of the Model and Application to GRS1915+105

In the previous chapter we have introduced the model and presented a possible, approximative solution to the GRMHD equations. In this chapter we will bring the profiles in a more convenient form and apply the model to the μQuasar GRS1915+105. Based on observational data we will try to further constrain our parameter regime, namely the transition radius, the black hole spin and the accretion rate. In turn we can make some estimates on the mass ejected in outflows and jets.

5.1 Discussion of the Solution to the Model

Before we proceed to the discussion of the solution, we rewrite the results. The form we have worked with is very compact but it is necessary to display the magnitude of the corresponding variable and its dependence on the parameters explicitly.
For completion we quote the results again in the form we have worked with so far:

$$\Omega_d = \begin{cases} \sqrt{GM}\left(r^{\frac{5}{4}} r_{tr}^{\frac{1}{4}} + r_g^{\frac{3}{2}} a\right)^{-1} & , \; r \in [r_*, r_{tr}] \\ \omega & , \; r < r_* \end{cases} \tag{5.1}$$

$$\Omega_w = \sqrt{GM}\left(r^{\frac{5}{4}} r_B^{\frac{1}{4}} + r_g^{\frac{3}{2}} a\right)^{-1} \tag{5.2}$$

$$v_d^{\varphi} = \begin{cases} \frac{\varpi}{\alpha}\left(\Omega_d - \omega\right) & , \; r \in [r_*, r_{tr}] \\ 0 & , \; r < r_* \end{cases} \tag{5.3}$$

$$v_w^{\varphi} = \frac{\varpi}{\alpha}\left(\Omega_w - \omega\right) \tag{5.4}$$

$$
\begin{aligned}
v_d^r &= -\sqrt{c^2 - v_d^{\varphi 2} - \frac{c^2}{\gamma_{d,tr}^2}\frac{\alpha^2}{\alpha_{tr}^2}\mathcal{F}_d\left(\frac{c^2 - v_d^{\varphi 2}}{c^2 - v_{K,tr}^{\varphi}{}^2}\right)^2} && (5.5)\\
\gamma_d &= \gamma_{d,tr}\frac{\alpha_{tr}}{\alpha}\frac{1}{\sqrt{\mathcal{F}_d}}\frac{c^2 - v_{K,tr}^{\varphi}{}^2}{c^2 - v_d^{\varphi 2}} && (5.6)\\
v_w^r &= \sqrt{c^2 - v_w^{\varphi 2} - \frac{c^2}{\gamma_{w,B}^2}\frac{\alpha^2}{\alpha_B^2}\mathcal{F}_w\left(\frac{c^2 - v_w^{\varphi 2}}{c^2 - v_{K,B}^{\varphi}{}^2}\right)^2} && (5.7)\\
\gamma_w &= \gamma_{w,B}\frac{\alpha_B}{\alpha}\frac{1}{\sqrt{\mathcal{F}_w}}\frac{c^2 - v_{K,B}^{\varphi}{}^2}{c^2 - v_w^{\varphi 2}} && (5.8)\\
v^\theta &= \frac{H_w}{r}\frac{\sqrt{\Delta}}{r}\frac{\rho_w}{\rho_d}\frac{\gamma_w v_w^r}{\gamma_d} && (5.9)\\
\dot{\mathcal{M}} &= 2\frac{|\dot{M}_w|}{\dot{M}_d} = \frac{3}{4}\frac{\sqrt{\Delta}}{r}\mathcal{L}\mathcal{S}\frac{\gamma_d}{\gamma_w}\frac{v_d^\varphi}{v_w^\varphi}\frac{v_w^r}{v_w^\varphi} && (5.10)\\
B^\theta &= \frac{\mathcal{B}_0}{\varpi\gamma_d v_d^r} && (5.11)\\
B^\varphi &= -\frac{3\mu_0}{16\pi}\frac{\dot{M}_d}{r^2}\frac{\gamma_d v_d^\varphi}{B^\theta}\mathcal{L} && (5.12)\\
H_w &= \frac{B^\theta}{B^\varphi} r\mathcal{S} && (5.13)\\
\eta_M &= \frac{H_w^2}{r\mathcal{S}}\gamma_w v_w^\varphi && (5.14)\\
\rho_d &= -\frac{\dot{M}_d}{4\pi H_d\sqrt{\Delta}\gamma_d v_d^r} && (5.15)\\
\rho_w &= \frac{1}{\mu_0}\left(\frac{B^\varphi}{\gamma_w v_w^\varphi}\right)^2 && (5.16)\\
T_d &= T_d(r_{tr})\left(\sqrt{\frac{\Delta}{\Delta(r_{tr})}}\frac{r}{r_{tr}}\left|\frac{\gamma_d v_d^r}{\gamma_{d,tr} v_{d,tr}^r}\right|\right)^{1-\Gamma} && (5.17)\\
T_{e,w} &= \frac{m_e c^2}{k}\sqrt{\frac{m_p m_e^2}{\Upsilon}\frac{1}{f_e}\frac{1}{r\mathcal{S}}\frac{\gamma_w{}^3 v_w^{\varphi 3}}{B^{\varphi 2}}\left(1 - \frac{v_w^{r\,2}}{c^2}\right)} && (5.18)\\
T_{i,w} &= \frac{\gamma_w{}^3 v_w^{\varphi 2}}{C_V\alpha}\left(1 - \frac{v_w^{r\,2}}{c^2}\right) && (5.19)
\end{aligned}
$$

In these expressions we have used the auxiliary function $\mathcal{F}_{d/w}, \mathcal{S}$ and $\mathcal{L}$. They were defined in (4.56), (4.57), (3.67) and (4.68), respectively, and will be reformulated below. We have left out the profiles of the electric fields since they are of no further interest for the following discussion. They can be derived by means of (3.64) and (3.65). The quantities depend on the six parameters: $\dot{M}_d$, M, a, r, r_{tr}, r_B. In order to reformulate these profiles we introduce the non-dimensional, scaled variables:

$$x = \frac{r}{r_g}\,, \quad m = \frac{M}{6\,M_\odot}\,, \quad \dot{m} = \frac{\dot{M}_d}{10^{17}\,g\,s^{-1}}, \tag{5.20}$$

where $10^{17}\,g\,s^{-1} = O(0.1\,L_{Edd}/c^2)$ is a typical accretion rate of stellar mass black holes. Further, we define the constants and auxiliary functions:

$$\mathcal{B}_{0,2} = \frac{\mathcal{B}_0}{10^6\,G \cdot c r_g} \quad (= O(1-10) \;\text{ for stellar systems}) \tag{5.21}$$

$$\mathcal{D} = 1 - \frac{2}{x} + \frac{a^2}{x^2} \tag{5.22}$$

$$\mathcal{F}_d = \begin{cases} \text{given by (4.56) and (4.57) for} & \\ a = 0 \text{ and } a > 0, \text{ respectively} & r \geq r_* \\ & \\ \mathcal{F}_{d,*} & r < r_* \end{cases} \tag{5.23}$$

$$\mathcal{F}_w = \begin{cases} \text{given by (4.56) and (4.57) for} \\ a = 0 \text{ and } a > 0, \text{ respectively} \end{cases} \tag{5.24}$$

$$\mathcal{G}_{d/w} = \mathcal{F}_{d/w}\,{\gamma_{tr/B}}^{-2}{\alpha_{tr/B}}^{-2}\left(1 - \frac{{v^{\varphi}_{K,tr/B}}^{2}}{c^2}\right)^{-2} \tag{5.25}$$

$$\mathcal{H}_2 = 10^2 \cdot \frac{H_{sd,tr}}{r_{tr}} \tag{5.26}$$

$$\mathcal{L} = \frac{4}{3} \cdot {\mathcal{V}_d}^{-1} \cdot \left[4\left(1 - \frac{a^2}{x^3}\right)\mathcal{W}^{-1} - 2\left(1 - \frac{1}{x}\right)\mathcal{D}^{-1} - \right. \tag{5.27}$$

$$\left. - \frac{5}{24} m^{-1}\, {x_{tr}}^{\frac{1}{4}} {\mathcal{O}_d}^{-1}\mathcal{W}{\mathcal{T}_d}^{-1} + 2ax^{-\frac{7}{4}}\mathcal{O}_d{\mathcal{T}_d}^{-1}\mathcal{W}^{-1}\left(3 + \frac{a^2}{x^2}\right)(2 - \mathcal{V}_d)^{-1}\right]$$

$$\mathcal{O}_{d/w} = {x_{tr/B}}^{\frac{1}{4}} + ax^{-\frac{5}{4}} \tag{5.28}$$

$$\mathcal{Q}_{d,1} = 10 \cdot \gamma_d \frac{v^r_d}{c} = 10 \cdot \left({\mathcal{G}_d}^{-1}\mathcal{D}^{-1}\mathcal{W}{\mathcal{V}_d}^{-1} - 1\right)^{\frac{1}{2}} \tag{5.29}$$

$$\mathcal{S} = \left[1 + \frac{2a^2}{x^3}\mathcal{W}^{-1}\left(\left(1 + \frac{a^2}{x^2}\right)\left(1 + (1 - \mathcal{V}_w)^{-1}\right) - \frac{2a}{x}\mathcal{D}^{\frac{1}{2}}(1 - \mathcal{V}_w)^{-\frac{1}{2}}\right)\right]^{-\frac{1}{2}} \tag{5.30}$$

$$\mathcal{T}_0 = \frac{T_{sd}(r_{tr})}{10^7 K} \tag{5.31}$$

$$\mathcal{T}_{d/w} = 1 - 2ax_{tr/B}{}^{\frac{1}{4}}x^{-\frac{7}{4}} + \frac{a^2}{x^2} \tag{5.32}$$

$$\mathcal{V}_{d/w} = 1 - \frac{{v^{\varphi}_{d/w}}^2}{c^2} = 1 - \frac{1}{36}m^{-2}\,x^{-\frac{1}{2}}\,{\mathcal{O}_{d,w}}^{-2}\,\mathcal{D}^{-1}\,{\mathcal{T}_{d,w}}^2 \tag{5.33}$$

$$\mathcal{W} = 1 + \frac{a^2}{x^2} + \frac{2a^2}{x^3} \tag{5.34}$$

In terms of these variables, the solution can be reformulated to yield:

$$\Omega_d = \begin{cases} 3.4\cdot 10^4 s^{-1}\cdot m^{-1}\,x^{-\frac{5}{4}}\,{\mathcal{O}_d}^{-1} & ,\ r\in[r_*, r_{tr}] \\ 6.8\cdot 10^4 s^{-1}\cdot m^{-1}\,a\,x^{-3}\,\mathcal{W}^{-1} & ,\ r<r_* \end{cases} \tag{5.35}$$

$$\Omega_w = 3.4\cdot 10^4 s^{-1}\cdot m^{-1}\,x^{-\frac{5}{4}}\,{\mathcal{O}_w}^{-1} \tag{5.36}$$

$$\frac{v^{\varphi 2}_d}{c^2} = \begin{cases} 2.8\cdot 10^{-2}\cdot m^{-2}\,x^{-\frac{1}{2}}\,\mathcal{D}^{-1}\,{\mathcal{O}_d}^{-2}\,\mathcal{T}_d^2 & ,\ r\in[r_*, r_{tr}] \\ 0 & ,\ r<r_* \end{cases} \tag{5.37}$$

$$\frac{v^{\varphi 2}_w}{c^2} = 2.8\cdot 10^{-2}\cdot m^{-2}\,x^{-\frac{1}{2}}\,\mathcal{D}^{-1}\,{\mathcal{O}_w}^{-2}\,{\mathcal{T}_w}^2 \tag{5.38}$$

$$\frac{v^{r2}_d}{c^2} = \mathcal{V}_d - \mathcal{G}_d\,\mathcal{D}\,\mathcal{W}^{-1}\,{\mathcal{V}_d}^2 \tag{5.39}$$

$$\gamma_d = {\mathcal{G}_d}^{-\frac{1}{2}}\,\mathcal{D}^{-\frac{1}{2}}\,\mathcal{W}^{\frac{1}{2}}\,{\mathcal{V}_d}^{-1} \tag{5.40}$$

$$\frac{{v^r_w}^2}{c^2} = \mathcal{V}_w - \mathcal{G}_w\,\mathcal{D}\,\mathcal{W}^{-1}\,{\mathcal{V}_w}^2 \tag{5.41}$$

$$\gamma_w = {\mathcal{G}_w}^{-\frac{1}{2}}\,\mathcal{D}^{-\frac{1}{2}}\,\mathcal{W}^{\frac{1}{2}}\,{\mathcal{V}_w}^{-1} \tag{5.42}$$

$$\frac{v^\theta}{c} = 10^{-2}\cdot\mathcal{H}_2\,\mathcal{D}\,\dot{\mathcal{M}}\left(\mathcal{V}_d - \mathcal{G}_d\mathcal{D}\mathcal{W}^{-1}{\mathcal{V}_d}^2\right)^{\frac{1}{2}} \tag{5.43}$$

$$\begin{aligned}\dot{\mathcal{M}} = {}& 4.5\cdot m\,x^{\frac{1}{4}}\,\mathcal{S}\,\mathcal{L}\,\mathcal{D}^{\frac{3}{2}}\,{\mathcal{O}_d}^{-1}\,{\mathcal{O}_w}^2\,\mathcal{T}_d\,{\mathcal{T}_w}^{-2}\cdot \\ &\cdot{\mathcal{G}_d}^{-\frac{1}{2}}{\mathcal{G}_w}^{\frac{1}{2}}{\mathcal{V}_d}^{-1}\mathcal{V}_w\left(\mathcal{V}_w - \mathcal{G}_w\mathcal{D}\mathcal{W}^{-1}{\mathcal{V}_w}^2\right)^{\frac{1}{2}}\end{aligned} \tag{5.44}$$

$$B^\theta = -10^7\,G\cdot\mathcal{B}_{0,2}\,x^{-1}\,\mathcal{W}^{-\frac{1}{2}}{Q_{d,1}}^{-1} \tag{5.45}$$

$$\begin{aligned}B^\varphi = {}& 4.6\cdot 10^7\,G\cdot{\mathcal{B}_{0,2}}^{-1}\,\dot{m}\,m^{-3}\,x^{-\frac{5}{4}}\,\mathcal{L}\,\mathcal{W}\,\mathcal{D}^{-1}\,{\mathcal{O}_d}^{-1}\,\mathcal{T}_d\cdot \\ &\cdot{\mathcal{G}_d}^{-\frac{1}{2}}{\mathcal{V}_d}^{-1}\mathcal{Q}_{d,1}\end{aligned} \tag{5.46}$$

$$\begin{aligned}H_w = {}& 2.2\cdot 10^{-1}\,r_g\cdot{\mathcal{B}_{0,2}}^2\,\dot{m}^{-1}\,m^3\,x^{\frac{5}{4}}\,\mathcal{S}\,\mathcal{L}^{-1}\,\mathcal{W}^{-\frac{3}{2}}\,\mathcal{D}\,\mathcal{O}_d\,{\mathcal{T}_d}^{-1}\cdot \\ &\cdot{\mathcal{G}_d}^{\frac{1}{2}}\mathcal{V}_d{\mathcal{Q}_{d,1}}^{-2}\end{aligned} \tag{5.47}$$

$$\begin{aligned}
\eta_M &= 2.1 \cdot 10^{14} \frac{cm^2}{s} \cdot \mathcal{B}_{0,2}{}^4\, \dot{m}^{-2}\, m^6\, x^{\frac{5}{4}}\, \mathcal{S}\, \mathcal{L}^{-2}\, \mathcal{W}^{-\frac{5}{2}}\, \mathcal{D}\, \mathcal{O}_d{}^2\, \mathcal{O}_w{}^{-1} \cdot \\
&\quad \cdot \mathcal{T}_d{}^{-2}\, \mathcal{T}_w\, \mathcal{G}_d\, \mathcal{G}_w{}^{-\frac{1}{2}}\, \mathcal{V}_d{}^2\, \mathcal{V}_w{}^{-1} \mathcal{Q}_{d,1}{}^{-4}
\end{aligned} \tag{5.48}$$

$$\begin{aligned}
\rho_d &= 6.7 \cdot 10^{-4} \frac{g}{cm^3} \cdot \mathcal{H}_2{}^{-1} \cdot \dot{m}\, m^{-2} x^{-2} \mathcal{D}^{-\frac{1}{2}}\, \mathcal{Q}_{d,1}{}^{-1} \\
\rho_w &= 6.9 \cdot 10^{-6} \frac{g}{cm^3} \cdot \mathcal{B}_{0,2}{}^{-2}\, \dot{m}^2\, m^{-4}\, x^{-2}\, \mathcal{L}^2\, \mathcal{W}\, \mathcal{O}_d{}^{-2}\, \mathcal{O}_w{}^2\, \mathcal{T}_d^2\, \mathcal{T}_w{}^{-2} \cdot \\
&\quad \cdot \mathcal{G}_d{}^{-1}\, \mathcal{G}_w \mathcal{V}_d{}^{-2} \mathcal{V}_w{}^2 \mathcal{Q}_{d,1}{}^2
\end{aligned} \tag{5.49}$$

$$T_d = 10^7 K \cdot \mathcal{T}_0 \cdot \left(\left(\frac{\mathcal{D}}{\mathcal{D}_{tr}} \right)^{\frac{1}{2}} \left(\frac{x}{x_{tr}} \right)^2 \mathcal{Q}_{d,1} \frac{0.01 \cdot c}{-\gamma_{d,tr} v^r_{d,tr}} \right)^{1-\Gamma} \tag{5.50}$$

$$\begin{aligned}
T_{e,w} &= 3.4 \cdot 10^8 K \cdot \mathcal{B}_{0,2}\, \dot{m}^{-1}\, m\, x^{\frac{3}{8}}\, \mathcal{S}^{-\frac{1}{2}}\, \mathcal{L}^{-1}\, \mathcal{D}^{-\frac{1}{2}}\, \mathcal{W}^{-\frac{1}{4}}\, \mathcal{O}_d\, \mathcal{O}_w{}^{-\frac{3}{2}} \cdot \\
&\quad \cdot \mathcal{T}_d{}^{-1}\, \mathcal{T}_w{}^{\frac{3}{2}}\, \mathcal{G}_d{}^{\frac{1}{2}}\, \mathcal{G}_w{}^{-\frac{3}{4}}\, \mathcal{V}_d\, \mathcal{V}_w{}^{-\frac{3}{2}} \cdot \mathcal{Q}_{d,1}{}^{-1} \cdot \left(1 - \mathcal{V}_w + \mathcal{G}_w \mathcal{D} \mathcal{W}^{-1} \mathcal{V}_w{}^2\right)
\end{aligned} \tag{5.51}$$

$$\begin{aligned}
T_{i,w} &= 1.0 \cdot 10^{11} K \cdot m^{-2}\, x^{-\frac{1}{2}}\, \mathcal{D}^{-3}\, \mathcal{W}^2\, \mathcal{O}_w{}^{-2}\, \mathcal{T}_w{}^2\, \mathcal{G}_w{}^{-\frac{3}{2}}\, \mathcal{V}_w{}^{-3} \cdot \\
&\quad \cdot \left(1 - \mathcal{V}_w + \mathcal{G}_w \mathcal{D} \mathcal{W}^{-1} \mathcal{V}_w{}^2\right)
\end{aligned} \tag{5.52}$$

In the derivation of this solution we have made use of several assumptions. First we assumed that the vertical drift v^θ is negligible as compared to the other velocity components and second that the TL is geometrically thin, i.e. $H_w/r < 1$. Further, we neglected magnetic fields in the radial momentum equation assuming that the accretion disk is dominated by the gravitational pull of the central black hole. Therefore we also have to verify that $\gamma_d v^\varphi_d \gg B^\theta/\sqrt{\mu_0 \rho_d}$. Since v^φ_d is sub-Keplerian this guarantees that gravitational forces are dominant as well. In Section 4.3.4 we have shown that the temperature of the electrons and the ions in the TL may differ considerably. This was due to the fact that the time scale for energy exchange is much longer than the dynamical time scale in the TL. We justify this procedure by comparing $T_{e,w}$ and $T_{i,w}$. These assumptions are checked considering several combinations that reasonably cover the parameter regime:

$$\begin{aligned}
a &= 0, 0.7, 0.998 \\
M &= 3\, M_\odot, 3 \cdot 10^8 M_\odot \\
\dot{M} &= 0.02, 0.95\, L_{Edd}/c^2 \\
r_{tr} &= 20\, r_g, 100\, r_g.
\end{aligned} \tag{5.53}$$

H_w/r depends weakly on a but strongly on M and $\dot{M}$ as can be seen from (5.47). Maximal values of H_w/r are obtained for low values of these three parameters. For $a = 0$ the accretion rate has to be greater than $\approx 0.03\, L_{Edd}/c^2$ if $r_{tr} = 20\, r_g$ and greater than $\approx 0.25\, L_{Edd}/c^2$ if $r_{tr} = 100\, r_g$ to obtain $H_w/r < 1$ everywhere. This indicates that r_{tr} is unlikely to exceed $100\, r_g$ in typical situations since the model becomes inconsistent for most parameter values in this case. For the other combinations of M and $\dot{M}$ the maximum value attained is around $H_w/r \approx 10^{-1} - 10^{-2}$. v^θ depends on $\dot{M}$ via the boundary condition $H_{sd,tr}$ (see Section 2.2). However, even for $\dot{M} \approx L_{Edd}/c^2$ the ratios v^θ/v^φ and v^θ/v^r achieve $10^{-2} - 10^{-3}$ maximum. The ratio of Alfvén velocity to orbital velocity satisfies

$$\frac{B^\theta/\sqrt{\mu_0\rho_d}}{\gamma_d v_d^\varphi} \approx 10^{-2} - 10^{-3} \tag{5.54}$$

for all combinations. The ratio of the electron- to ion temperature in the TL satisfies $T_{e,w}/T_{i,w} < 10^{-1}$ for all combinations. It decreases strongly with decreasing radius. This is surprising since the two temperature flow in the TL was justified by the magnitude of the energy exchange time scale. The ladder is much longer in the TL since the density is much lower than in the disk. In the vicinity of the central black hole, however, ρ_w increases strongly even exceeding ρ_d for high accretion rates. This means that the plasma might not be tenuous throughout the whole TL but the two-temperature description still remains valid.
We conclude that the model is self-consistent for reasonable values of $a, M, \dot{M}$ and r_{tr} well below $100\, r_g$.

Finally, we plot of the profiles, presented in this section. We have chosen the following values for the parameters:

$$\begin{aligned} M &= 6\, M_\odot \\ \dot{M}_d &= 10^{17} g\, s^{-1} \approx 0.1\, L_{Edd}/c^2 \\ a &= 0.95 \\ r_B &= r_{ms} \\ r_{tr} &= 40\, r_g. \end{aligned} \tag{5.55}$$

The boundary values have been chosen to be:

$$\begin{aligned} v_d^r(r_{tr})/c &= -1.28 \cdot 10^{-1} \\ H_d(r_{tr})/r_{tr} &= 1.79 \cdot 10^{-3} \\ \rho_d(r_{tr}) &= 9.24 \cdot 10^{-7} g\, cm^{-3} \\ T_d(r_{tr}) &= 1.36 \cdot 10^7 K. \end{aligned} \tag{5.56}$$

The one-dimensional profiles correspond to $\theta = \pi/2$ for the variables in the disk and $\theta = \pi/2 + \theta_d + \delta\theta/2$ or $\theta = \pi/2 + \theta_d$ in the TL (depending on the variable), respectively. Plots of two-dimensional distributions are presented as well in order to get a better understanding of the model. In this case we have changed from the coordinate θ to $z = r\cos\theta$. The distributions in the vertical direction have been chosen mainly such that they are appropriate for illustration purposes. In the case of the standard disk we had hydrostatic equilibrium in the vertical direction implying a Gaussian distribution. Hydrostatic equilibrium seems problematic in the inner region. It might be applicable to the disk but surely not to the TL. Hence, the detailed distributions will probably deviate from a Gaussian distribution. Still it will suffice for illustration purposes since we expect it to capture the qualitative behavior at least roughly. Correspondingly, the functions are of the kind

$$e^{-\frac{1}{2}\frac{z^2}{H_d^2}} \quad \text{or} \quad e^{-\frac{1}{2}\frac{(z-H_d-H_w/2)^2}{(H_w/2)^2}}. \tag{5.57}$$

These functions will be modulated and normalized depending on the variable. In the case of the two-dimensional distribution of velocity and density, depicted in Fig. 5.7, we have chosen the vertical profiles:

$$\begin{aligned}
\rho_d(r,z) &= \begin{cases} \rho_d(r) & \text{for} \quad z=0 \\ 0 & \text{for} \quad |z| \geq H_d \end{cases} && (5.58)\\
\rho_w(r,z) &= \begin{cases} \rho_w(r) & \text{for} \quad |z| = H_d + H_w/2 \\ 0 & \text{for} \quad |z| \notin [H_d, H_d+H_w] \end{cases} && (5.59)\\
v^r_{d/w}(r,z) &\;\; \ldots \;\; \text{the same as density} && (5.60)\\
v^\theta(r,z) &= \begin{cases} \pm v^\theta(r) & \text{for} \quad z = \pm H_d \\ 0 & \text{for} \quad |z| \leq 2H_d \end{cases} && (5.61)\\
\tilde{\Omega}(r,z) &= \begin{cases} \tilde{\Omega}_d(r) & \text{for} \quad z=0 \\ \tilde{\Omega}_w(r) & \text{for} \quad |z| = H_d + H_w/2 \\ 0 & \text{for} \quad |z| \geq H_d + H_w. \end{cases} && (5.62)
\end{aligned}$$

The distributions of the magnetic field components (depicted in Fig. 5.8) emerge from the ideal MHD equations together with the distributions of v_d^r and $\tilde{\Omega}$. In the case of B^θ the cutoff has been removed from (5.60) to prevent singular behavior. B^r is given by (4.23). The vertical distribution of B^φ corresponds to $B^\varphi \propto \partial_\theta \Omega$ (see (3.63)). The magnetic field components read:

$$\begin{aligned}
B^r(r,z) &= \frac{z}{H_d^2}\left(\frac{r^2}{\sqrt{\Delta}} - \frac{r_{tr}^2}{\sqrt{\Delta(r_{tr})}}\frac{\gamma_d v_d^r}{\gamma_{d,tr} v_{d,tr}^r}\right) B^\theta(r,z) && (5.63)\\
B^\theta(r,z) &= B^\theta(r)\, e^{\frac{1}{2}\frac{z^2}{H_d^2}} && (5.64)\\
B^\varphi(r,z) &\propto \partial_z\left(e^{-\frac{1}{2}\left(\frac{z-H_d}{H_w/2}-1\right)^2} + e^{-\frac{1}{2}\left(\frac{z+H_d}{H_w/2}+1\right)^2}\right) && (5.65)\\
B^\varphi(r,\pm H_d) &= \pm B^\varphi(r). && (5.66)
\end{aligned}$$

At a given radius the poloidal field strongly increases with increasing $|z|$ (exponentially in this case since $B^\theta \propto 1/v^r$). This is due to the assumption of stationarity together with ideal MHD. In a time dependent case where the poloidal field is homogeneous and vertical in the beginning, $\vec{B}_p(t_0) = (0, B_0^\theta)$, the infall of matter drags the magnetic field lines towards the center. A radial component emerges and the magnetic field lines approach each other increasingly with increasing time thus amplifying the magnetic field. Clearly this distribution becomes unphysical for $|z| \gg H_d$ but we limit ourselves to $|z| = O(H_d)$. Additionally we have not included magnetic reconnection in the poloidal component. Of course, if we did, the poloidal field would be weakened in the TL.

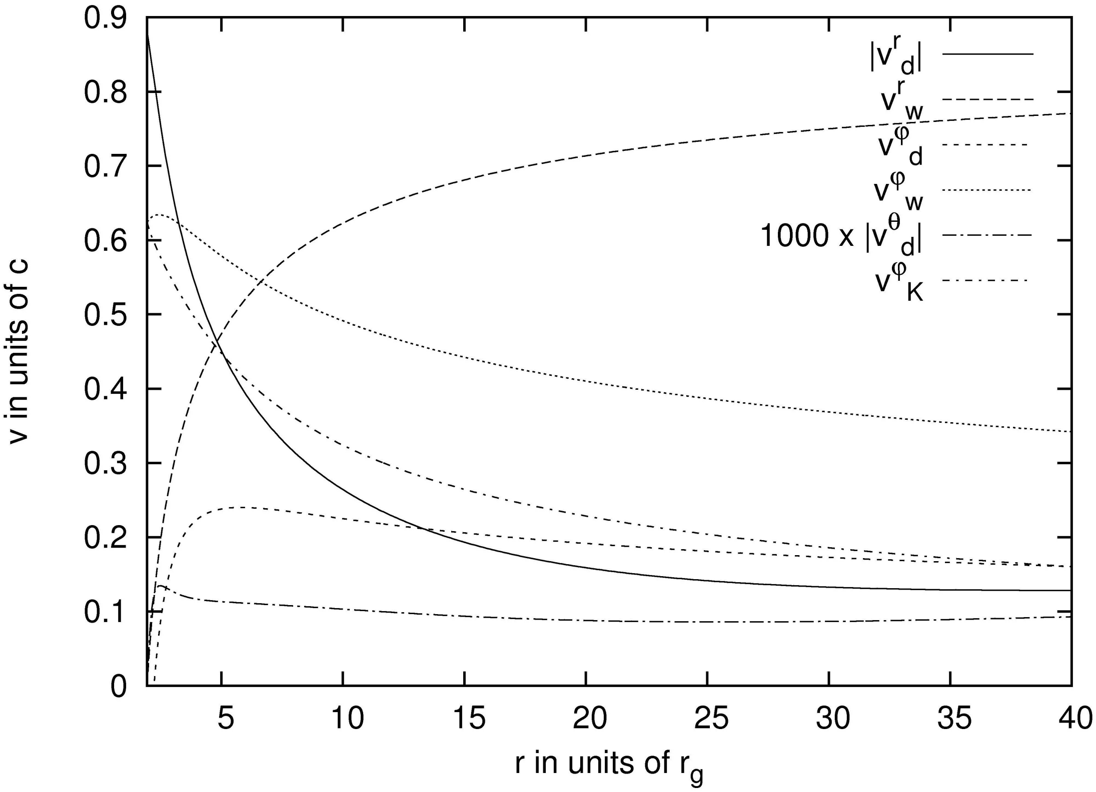

Figure 5.1: The velocity components in the disk and transition layer

This plot shows the radial profiles of v_d^r, v_w^r, v_d^φ, v_w^φ, v_K^φ and v^θ, corresponding to the radial- and orbital velocity in the disk and TL and the Keplerian- and vertical velocity, respectively. The ladder has been magnified 1000 times. Obviously v^θ is much smaller than all other velocity components.

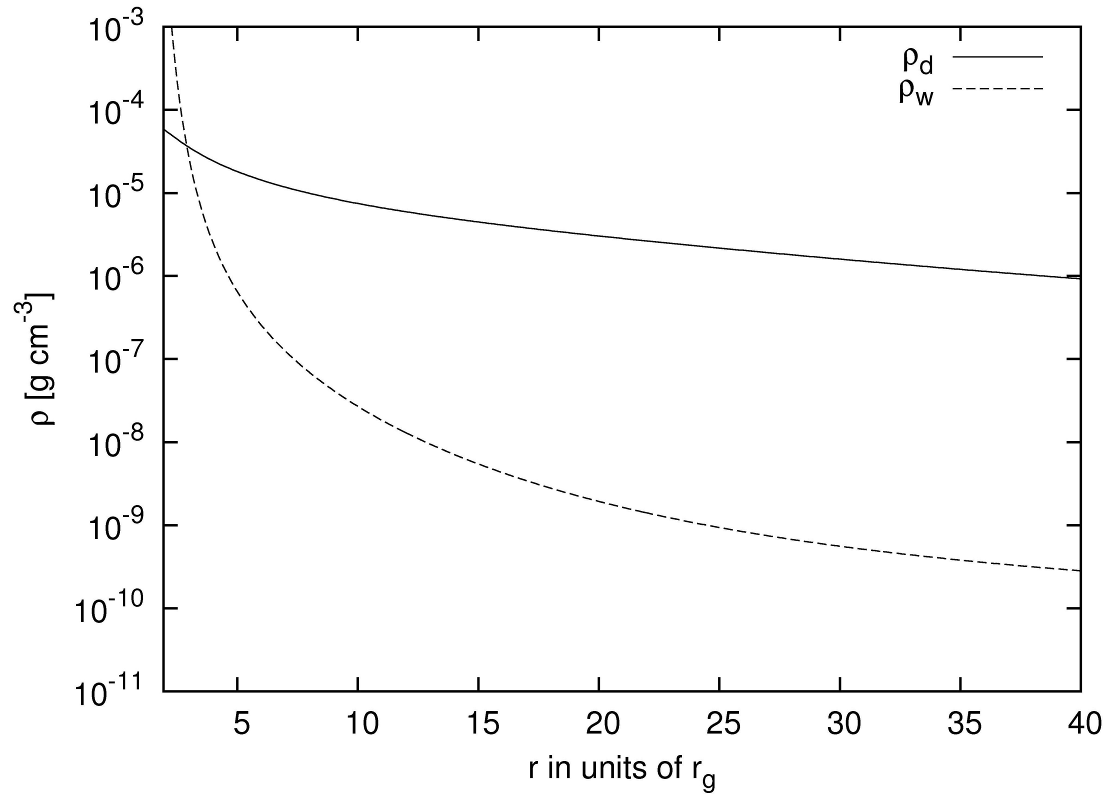

Figure 5.2: The density in the disk and transition layer

The density profiles ρ_d and ρ_w are displayed. Clearly the density in the TL is much lower than in the disk. Hence, only a small percentage of matter is ejected in the jet. Approaching the marginally stable orbit, ρ_w strongly increases. This is due to the strong increase of B^{φ} for $r \rightarrow r_{ms}$. It is plausible, though, that most of the matter in this region is pushed into the black hole. This is suggested by the proximity to the marginally stable orbit and the fact that the TL is extremely thin in this region. Thus the incoming matter will be pushed towards the center. Furthermore, the radial velocity is extremely low the innermost part of the in the TL (see Fig. 5.1). As a consequence the high density in this region will not effect to total massload of the jet.

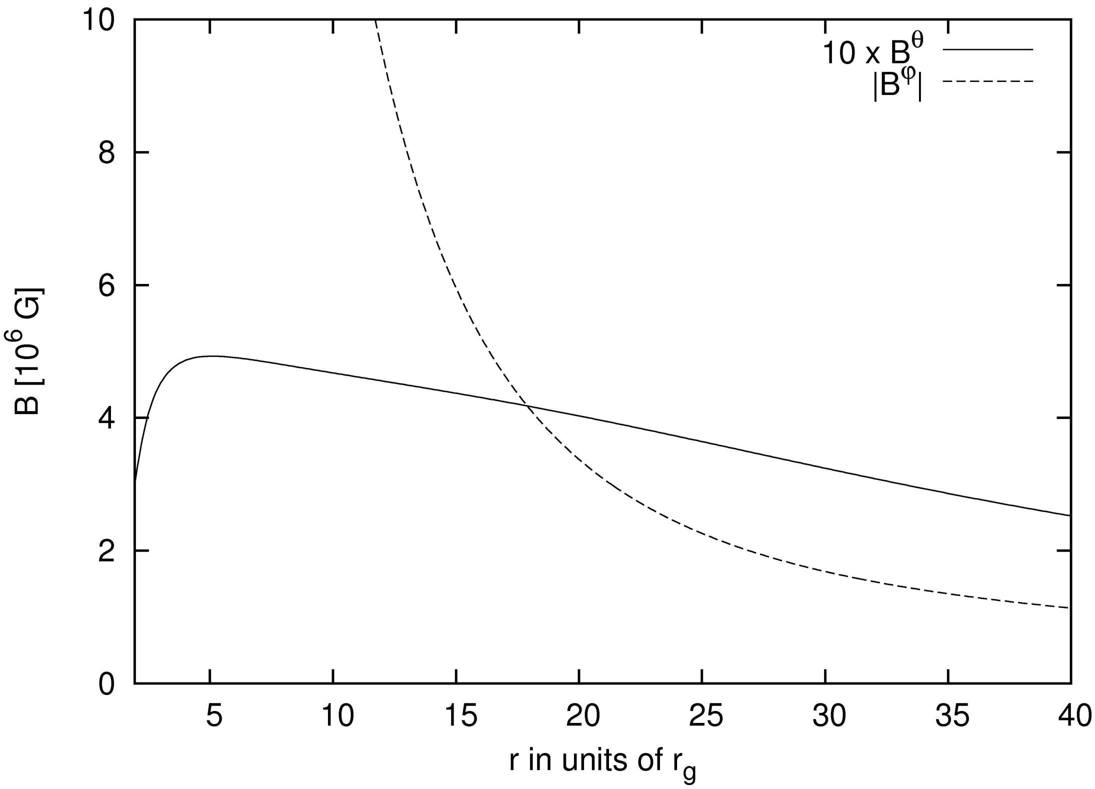

Figure 5.3: The vertical and toroidal magnetic field in the disk and transition layer

$-B^\varphi$ and B^θ are plotted. The ladder has been magnified 30 times. One can see that $B^\theta \ll -B^\varphi$ implying that the TL is geometrically thin, according to the previous assumption.

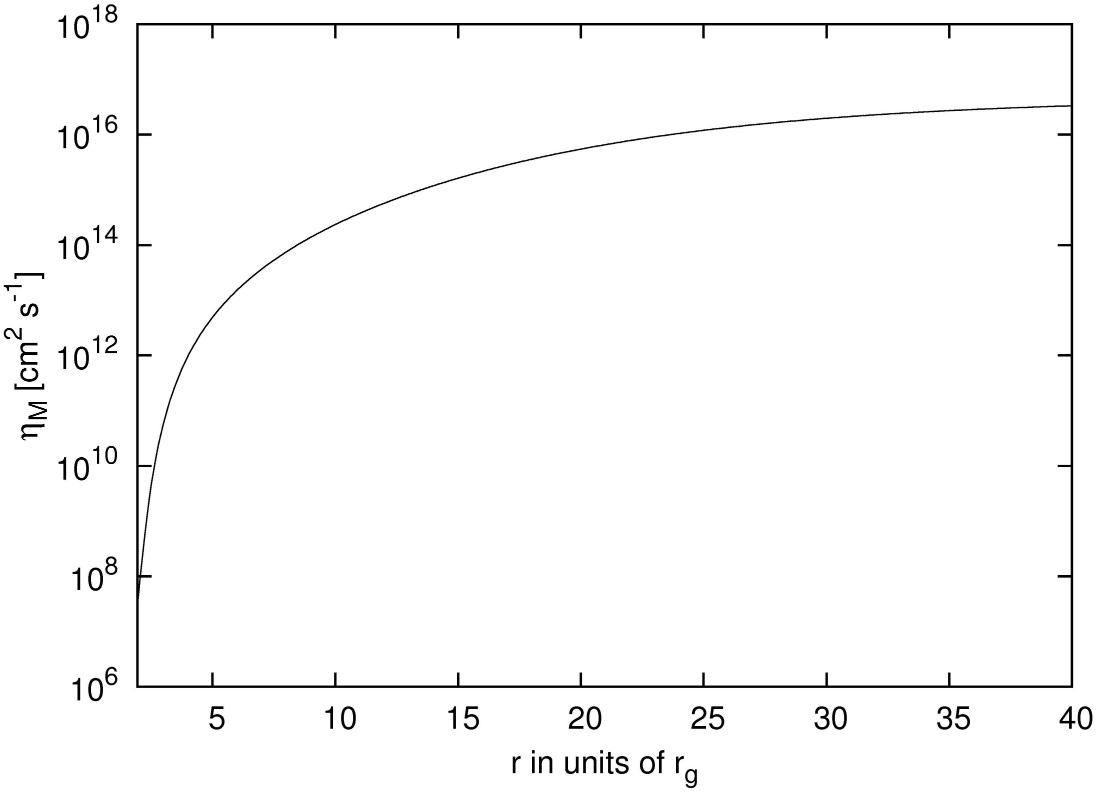

Figure 5.4: The magnetic diffusivity in the transition layer

The magnetic diffusivity in the TL gives rise to reconnection thus heating the matter. In the disk, on the other hand, ideal MHD is assumed.

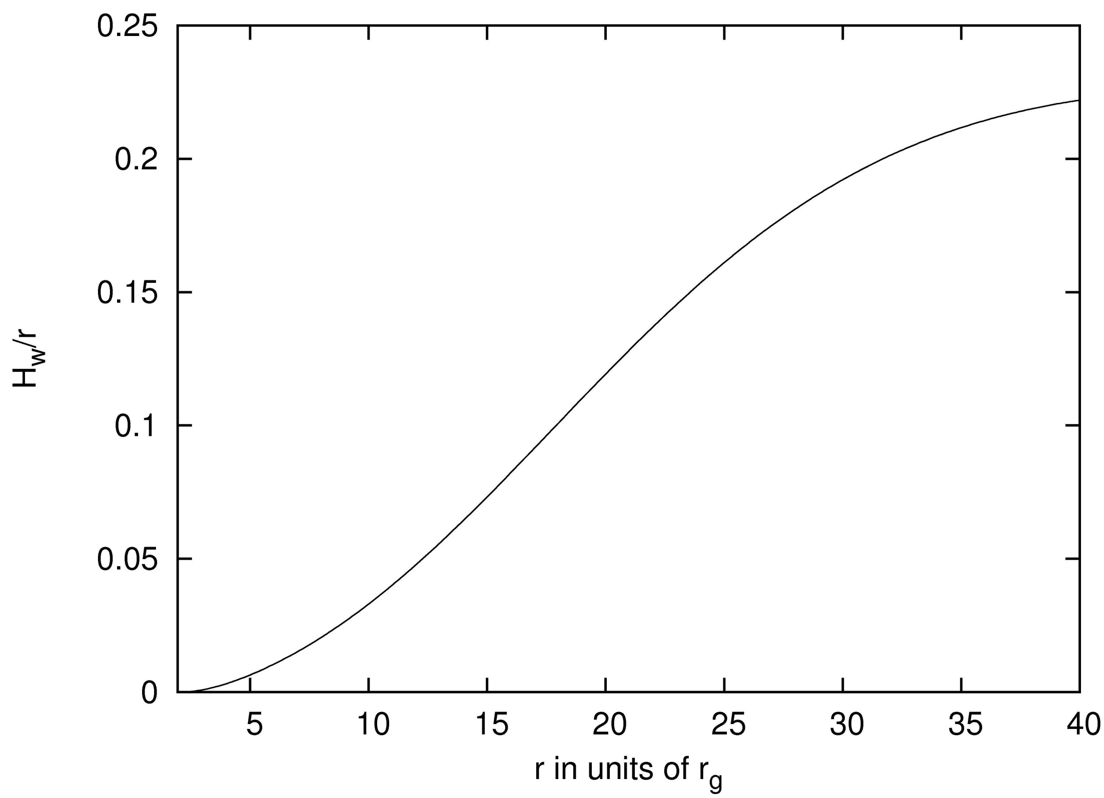

Figure 5.5: The relative thickness of the transition layer

H_w/r is plotted. On can see that the transition layer blows up with increasing radius but remains geometrically thin in the inner region. For $r > r_{tr}$ the model can not be applied since there is no transport of angular momentum from the disk. Reconnection ceases and a different description of the flow is necessary.

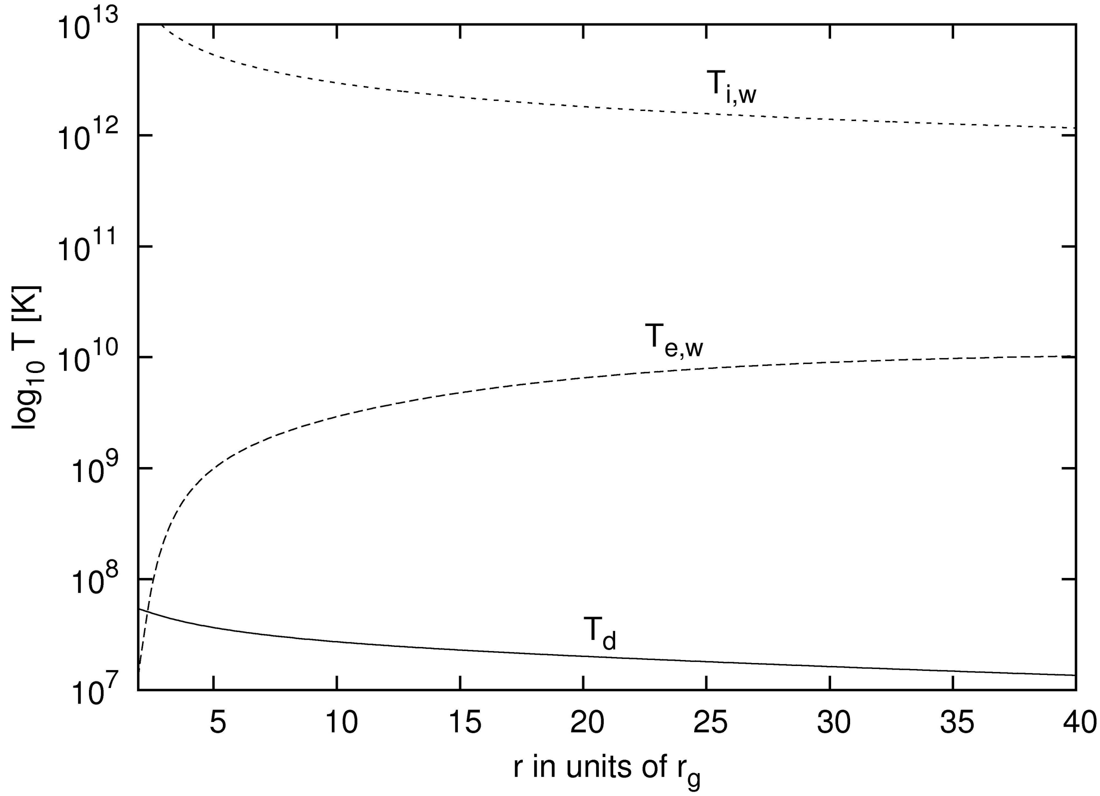

Figure 5.6: The temperature profiles in the disk and transition layer

The logarithmic profiles of the temperature in the disk and electron/ion temperatures in the TL are plotted. Clearly the TL is much hotter than the disk since it is intensively heated by reconnection. Electrons and ions have very different temperatures in the inner region. At larger radii the matter is supposed to cool thus settling to a one temperature flow.

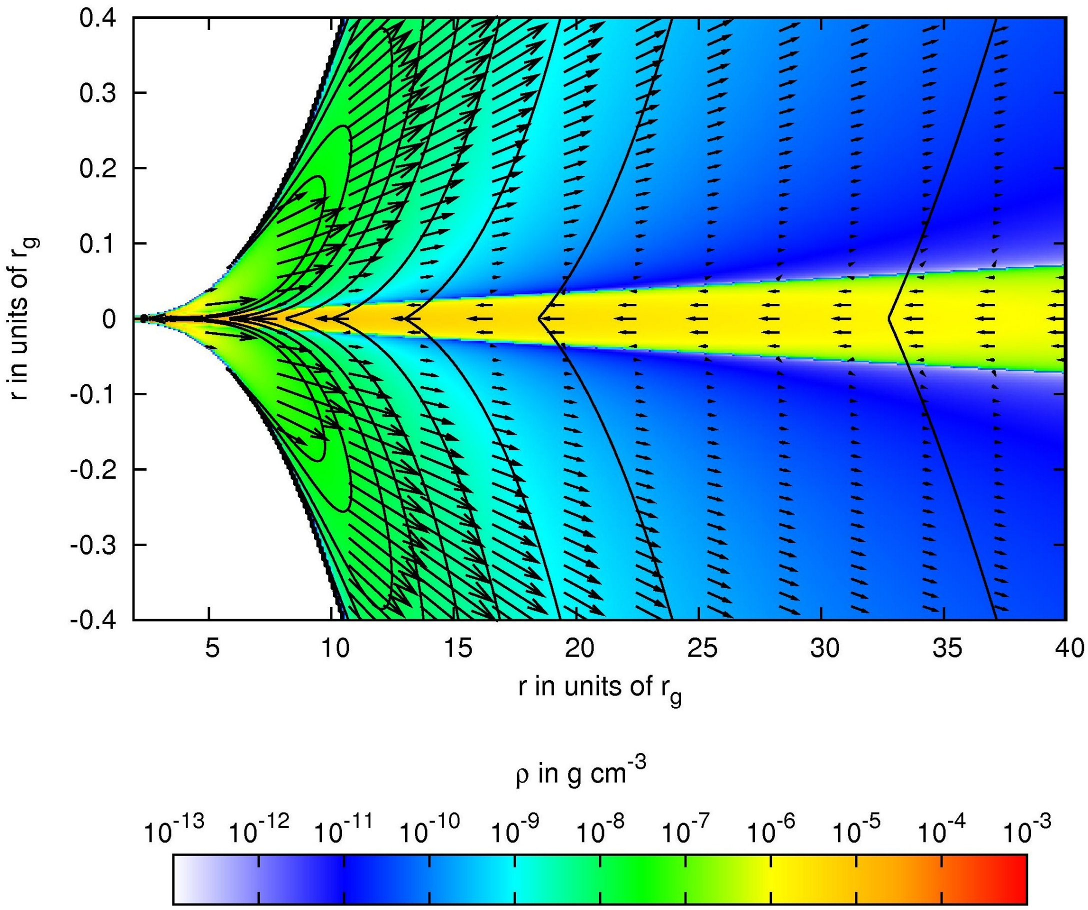

Figure 5.7: Two-dimensional distribution of the density, poloidal- and angular velocity

This graphic shows the velocity distribution plotted over the color coded density distribution. Solid isolines of $\tilde{\Omega}$ are drawn but the actual values have been omitted so the graphic will not become overloaded. The poloidal velocity distribution (v^r, v^θ) is drawn with arrows, given in units of c but magnified by a factor of 5. One can clearly see that $\tilde{\Omega}$ achieves higher values in the TL than in the disk for a given radius. The outflowing wind is very tenuous compared to the disk while its velocity becomes comparable to the speed of light very fast, rendering the matter highly energetic.

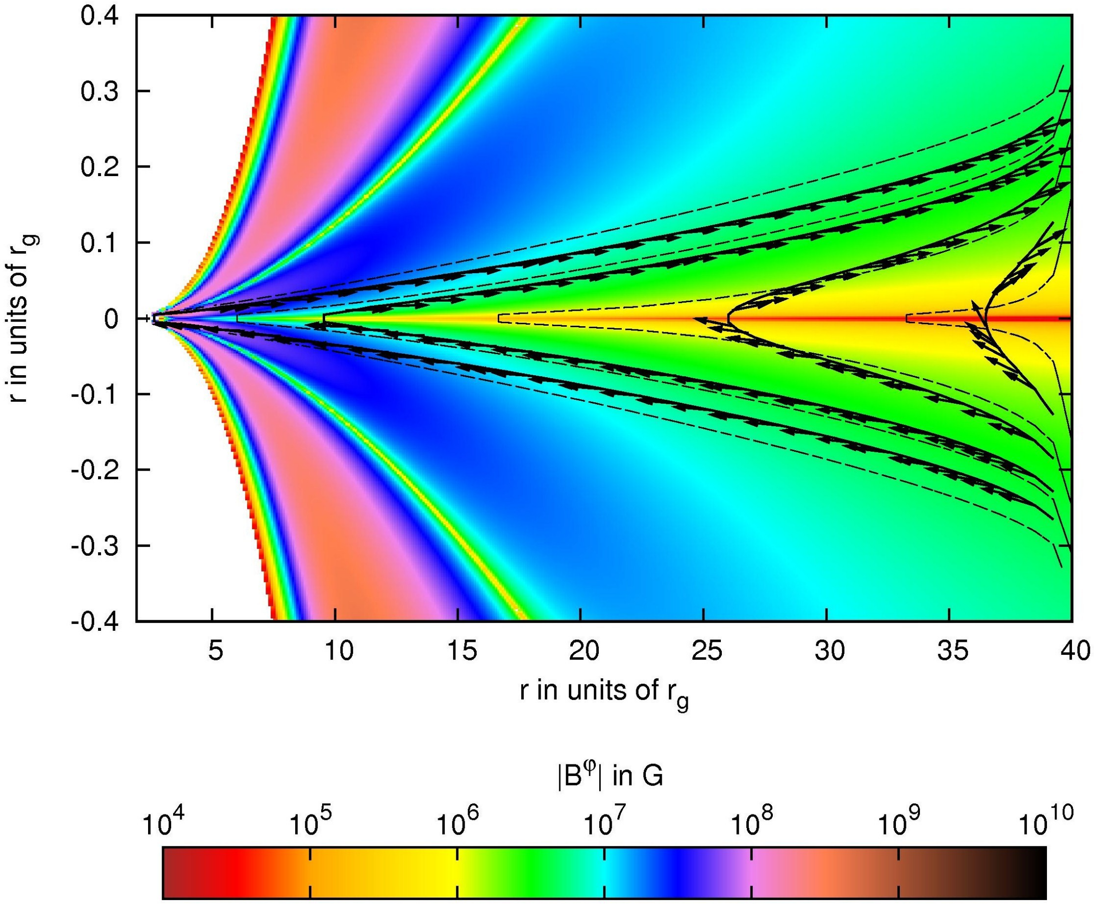

Figure 5.8: Two-dimensional distribution of the poloidal- and toroidal magnetic field

This plot shows the distribution of the magnetic field components. The direction of the poloidal field lines is indicated by normalized arrows along solid lines of constant A^3, where $A = A^a e_a$ is the four-vector potential. Dashed lines mark curves of constant $|\vec{B}_p|$, i.e. constant strength of the total poloidal field $\vec{B}_p = (B^r, B^\theta)$. One should notice that the poloidal field changes from being predominantly vertical to radial with decreasing radius. Within the equatorial plane, though, $B^r = 0$ provided that there has been no radial component to begin with (which is assumed). The toroidal field B^φ is color coded. It varies strongly with z, especially in the immediate vicinity of the black hole.

5.2 Application of the model to GRS1915+105

In this section we discuss the application of the new model to the μQuasar GRS1915+105 which was already introduced in Section 1.3. Now we can combine observational data with the parameters of the model and make in turn some estimates on the parameters of the system.
In this section we discuss three points:

- the magnitude of the transition radius r_{tr}
- the spin of the black hole in GRS1915+105
- the predicted outflow rate during flaring states (A $\leftrightarrow$ C)

The magnitude of r_{tr} can be estimated by means of the light curves obtained from GRS1915+105. We adopt an interpretation similar to that of Belloni et al. (2000), namely that during state A and B the accretion disk is well described by a standard α-disk all the way down to the marginally stable orbit. During state C, however, the accretion disk is only well described by an α-disk for $r > r_{tr}$. Interior to r_{tr} the disk can be described by the model proposed in this work. This means that the disk is threaded by large-scale, super equipartition, poloidal magnetic fields in this region. The magnetic fields suppress the generation of turbulence and subsequently prevent viscous dissipation. Therefore the innermost region is much fainter than the α-disk model predicts. As a consequence the disk appears to be truncated. This is analogous to sunspots that appear to be black compared to their bright surrounding.
This assumption allows us to make an estimate on the magnitude of r_{tr}. There are phases where GRS1915+105 displays oscillations between state A and C (class θ of Belloni et al. (2000)). A sample of the corresponding light curve is shown in Fig. 5.9. We assume that the region dominated by large-scale, poloidal magnetic fields reaches up to a maximum radius $r_{tr,max}$ during the low state. When the intensity is rising, r_{tr} starts decreasing, eventually reaching the radius of marginal stability r_{ms}. The whole flow is described by the standard α-disk in this case. Dynamo action in the α-disk in combination with the strong gravitational field then produces large-scale magnetic fields that significantly change the dynamics of the flow as mentioned above and the α-disk becomes truncated at $r_{tr,max}$ again. The extension of the α-disk region happens by a viscous flow that starts spiraling inwards from $r_{tr,max}$ on the time scale:

$$t_{vis} = \frac{r^2}{\nu}. \tag{5.67}$$

Since the concerned region lies in the vicinity of a black hole, we apply the relativistic generalization of the profiles obtained in Section 2.2. Changing to the

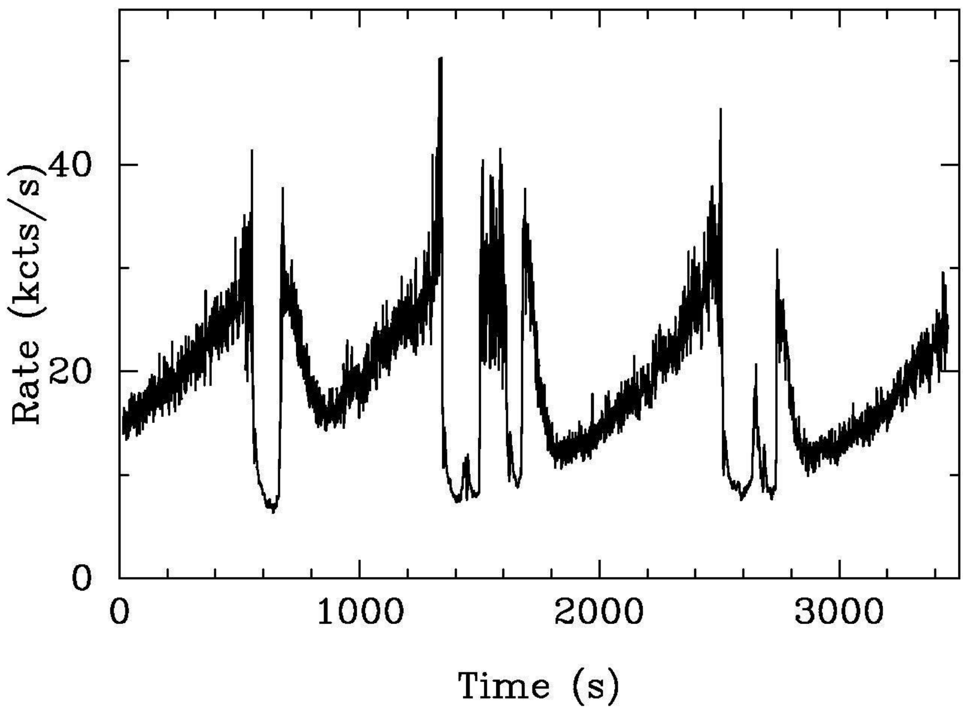

Figure 5.9: Class θ light curve of GRS1915+105

GRS1915+105 remains in state C for $\approx 120\,s$ (low luminosity). Then follows a phase that lasts for $\approx 800\,s$ where the source makes a transition into state A: the luminosity has a sharp peak and then rises towards a maximum.
Credits: Image Belloni et al. (2000), data from observations with RXTE

variables $x, m, \dot{m}$, inserting $t_{vis} \approx 800\,s$, $m = 14$, $\dot{m} \approx 11$ (accretion rate during quiescence, see 1.3, page 27) and rearranging yields:

$$x^{\frac{7}{2}} \frac{\mathcal{B}_{NT}{}^7 \mathcal{D}_{NT}{}^2 \mathcal{E}_{NT}{}^2}{\mathcal{A}_{NT}{}^4 \mathcal{Q}_{NT}{}^2} = 8.3 \cdot 10^6\,\alpha. \tag{5.68}$$

The auxiliary functions on the left-hand side were defined in Novikov and Thorne (1973) and are quoted in appendix A. The solution of this equation is presented as a function of α and a in Table 5.1. If $\alpha < 10^{-4}$ then r_{tr} would take values around or even below the marginally stable orbit. Therefore we have taken $\alpha \in [0.0001, 1]$. Since r_{tr} extends up to $\approx 100\,r_g$ we also have to check whether the inner solution of the standard disk applies indeed. The radii r_{m-i} where the transition between the middle- and inner region occurs are solutions of the equation:

$$x \cdot \left(\frac{\mathcal{B}_{NT}{}^{36} \mathcal{D}_{NT}{}^8 \mathcal{E}_{NT}{}^{10}}{\mathcal{A}_{NT}{}^{20} \mathcal{Q}_{NT}{}^{16}} \right)^{\frac{1}{21}} = 102.7 \cdot \alpha^{\frac{2}{21}}. \tag{5.69}$$

	r_{tr}/r_g			r_{m-i}/r_g		
α	$a = 0$	$a = 0.7$	$a = 0.998$	$a = 0$	$a = 0.7$	$a = 0.998$
0.0001	$< r_{ms}$	4.3	5.3	40	40	41
0.0005	10	8.7	9.3	47	47	48
0.001	11	11	12	50	51	51
0.005	18	19	19	59	59	60
0.01	23	24	24	63	64	64
0.05	38	38	39	74	75	75
0.1	47	47	48	79	80	81
0.5	75	76	76	93	94	94
1	92	93	93	100	100	101

Table 5.1: r_{tr}/r_g and r_{m-i}/r_g as a function of α and a

r_{tr} and r_{m-i} depend only weakly on a and remain below $\approx 100\, r_g$ provided that $\alpha < 1$. If α were even smaller than 10^{-4}, then r_{tr} would be around or even below the marginally stable orbit r_{ms}. One can see that in every case r_{m-i} is larger than r_{tr}. This justifies the application of the inner standard disk solution.

The results are presented in Table 5.1 as well. The solutions to equations (5.68) and (5.69) are insensitive to the black hole spin. Based on these results we can infer that $r_{tr} < 100\, r_g$ (in agreement with what we have found in Section 5.1). It should be noted that our interpretation of the light curves uses a sample from a different class than that used by Belloni et al. (1997a).
Now we can turn to the question of the black hole spin. In our model the wind's velocity, temperature and strength of the advected, toroidal magnetic field depend on a and r_{tr}. The spin a determines the maximum depth of the potential well that plasma can escape from. This is because the minimal radius r_B of the inner boundary of the TL is given by r_{ms} which is a decreasing function of a. r_{tr}, on the other hand, determines how much rotational energy the wind is supplied with. In the TL the plasma has the total energy per mass:

$$E = E_{therm} + E_{kin} + E_{mag}, \tag{5.70}$$

where $E_{therm}, E_{kin}, E_{mag}$ correspond to the thermal-, bulk kinetic- and magnetic energy per mass, respectively. $E(r_{tr}) = E_{tr}$ is the energy per mass inherent in an annulus of plasma at r_{tr} that is carried out of the inner region - possibly to infinity. However, the energy of such an annulus of plasma is not necessarily conserved during its propagation. It might well be that a fraction of the energy is dissipated due to processes that collimate the wind into a jet on larger length scales. Other sources of dissipation might be internal shocks or interaction within the jet-plasma and with the surrounding medium. However, we do not want to go into the details of jet propagation but limit ourselves to a rough estimate. Therefore we assume that the total energy of the plasma is indeed conserved exterior to r_{tr}:

$$E_{tr} = E_\infty. \tag{5.71}$$

E_{therm} is dominated by virial-hot ions. Ions are poor radiators and cool mainly by adiabatic expansion. Hence we expect the thermal energy to be roughly conserved by itself: $E_{therm,tr} \approx E_{therm,\infty}$. In this case (5.71) reduces to:

$$E_{kin,tr} + E_{mag,tr} = E_{kin,\infty} + E_{mag,\infty}. \tag{5.72}$$

The expressions for the bulk-kinetic- and magnetic energy per mass in the TL are:

$$E_{kin} = -\dot{x}_{t,w}c = -g_{tt}\dot{t}_w c^2 - g_{t\varphi}\dot{\varphi}_w c = \gamma_w \alpha c^2 + \omega l_w \tag{5.73}$$

$$E_{mag} = \frac{{B_w}^2}{2\mu_0\rho_w} \approx \frac{B^{\varphi 2}}{2\mu_0\rho_w} = \frac{1}{2}{\gamma_w}^2 v_w^{\varphi 2}, \tag{5.74}$$

where we have approximated the magnetic field in the TL by its most dominant component B^φ. Only a part of the toroidal field is dissipated in the TL while the rest is advected outwards, i.e. $B^\varphi = B^\varphi_{diss} + B^\varphi_{adv}$. Their ratio is given by:

$$\frac{B^\varphi_{diss}}{B^\varphi_{adv}} = \frac{t_{adv}}{t_{diss}} = \frac{r}{\sqrt{\Delta}}\frac{1}{\mathcal{S}}\frac{v^\varphi_w}{v^r_w}, \tag{5.75}$$

where the time scales t_{diss}, t_{adv} can be inferred from (3.63). Hence the bulk kinetic- and magnetic energy per mass that is actually advected in the wind becomes:

$$E_w = \gamma_w \alpha c^2 + \omega l_w + \frac{\frac{1}{2}{\gamma_w}^2 v_w^{\varphi 2}}{1 + \frac{r}{\sqrt{\Delta}}\frac{1}{\mathcal{S}}\frac{v^\varphi_w}{v^r_w}}, \tag{5.76}$$

where $l = \dot{x}_\varphi = \varpi^2\tilde{\Omega}/\alpha$ is the angular momentum per unit mass that we already worked with.

According to Greiner (2001) the ejecta of GRS1915+105 propagate with $v_{bulk} = 0.92\,c$. Fender et al. (1999); Dhawan et al. (2000) have derived a velocity of $0.98\,c$. Yet, it is unclear whether the higher value is due to actual faster propagation of the jet or to misinterpretation of the measurement. The motion of the ejecta is consistent with a ballistic propagation.

Mirabel et al. (1998) reported on the ejection of plasma clouds in 1997 September 9. The clouds expand with $\approx 0.2\,c$, i.e. after $15\,min$ (the time of observation) they have dimension $L \approx 5 \cdot 10^{12} cm$. The magnetic field strength is estimated to $B_{cl} = 16\,G$ corresponding to equipartition with $5 \cdot 10^{39} erg$ energy in relativistic electrons assuming a representative Lorentz factor of about 10^3. The bulk kinetic- and magnetic energy per mass of a typical plasma cloud are then of the order:

$$E_{cl} = \gamma_{bulk} c^2 + \frac{{B_{cl}}^2}{2\mu_0} \cdot \frac{\frac{4\pi}{3}L^3}{M_{cl}} \approx \begin{cases} 3.0 \cdot 10^{21}\, erg\, g^{-1} & , \quad v_{bulk} = 0.92\,c \\ 5.2 \cdot 10^{21}\, erg\, g^{-1} & , \quad v_{bulk} = 0.98\,c. \end{cases} \tag{5.77}$$

r_{tr}/r_g	a	$\dot{\mathcal{M}}_{0,tr}$ in %	r_{tr}/r_g	a	$\dot{\mathcal{M}}_{0,tr}$ in %
3	0.9987	4.6	14.5	0.9930	8.6
3.5	0.9982	5.3	17	0.9926	8.8
4	0.9977	5.8	20	0.9921	8.9
4.5	0.9973	6.2	30	0.9912	9.1
5	0.9969	6.5	40	0.9906	9.1
6.25	0.9960	7.2	50	0.9902	9.1
7.5	0.9953	7.6	60	0.9899	9.1
8.75	0.9947	7.9	70	0.9897	9.1
10	0.9942	8.1	80	0.9896	9.1
12	0.9936	8.4	90	0.9894	9.1

Table 5.2: a and $\dot{\mathcal{M}}_{0,tr}$ for $v_{bulk} = 0.92\,c$.

This table displays combinations of a, r_{tr} that satisfy $E_w = E_{cl}$ and $r_{tr} < 100\,r_g$. Additionally, the relative outflow rate $\dot{\mathcal{M}}_0$ is given. It is obvious that only a rapidly rotating black hole is consistent with observations. $r_{tr} < 3.5\,r_g$ implies $a > 0.9982$ which is the maximum black hole spin derived by Thorne (1974).

Setting $r_B = r_{ms}$ we can find a suitable combination of a and r_{tr} that satisfies $E_{cl} = E_w$. The results are displayed in Table 5.2. They are only consistent with a nearly maximally rotating black hole ($a > 0.989$), unless r_{tr} greatly exceeds $100\,r_g$ implying $\alpha \gg 1$. This is in agreement with the very small value of the minimal inner disk radius of $\approx 20\,km$. If we let $r_{tr} < 300\,km \approx 14.5\,r_g$ as indicated by observational data (Belloni et al., 1997a) we even obtain $a > 0.9930$.
In appendix B we present additional data for $v_{bulk} = 0.94, 0.96, 0.98\,c$. This should account for the possibility that the ejecta are indeed propagating with $v_{bulk} > 0.92\,c$. One can observe that, if r_{tr} decreases, a has to increase in order to obtain the observed velocity. Thus if r_{tr} drops below a certain value, a has to be larger than 0.9982. It should be noted at this point that the matter and radiation that a black hole swallows from its surrounding accretion disk should spin it up until it eventually rotates at maximum rate. Thorne (1974) showed, however, that the radiation from the disk exerts a counter-torque which prevents the black hole from reaching $a = 1$. In the limiting state it spins with $a = 0.9982$. It is not clear whether this upper limit on the Kerr-parameter applies strictly to GRS1915+105. The system spends a large fraction of its time in a state where the inner disk radiates very poorly. On the other hand, in our model the accreted disk matter has lost a large fraction of its rotational energy when it passes the last stable orbit and magnetic fields exert an additional counter-torque on the black hole through frame-dragging. If the limit derived by Thorne (1974) is to be taken seriously, we can put a lower limit to r_{tr}: $v_{bulk}/c = (0.92, 0.94, 0.96, 0.98)$ yields $r_{tr}/r_g \geq (3.5, 4.5, 5, 17)$, respectively. Since $14.5\,r_g$ is the maximum value

observed for r_{tr} this excludes propagation with $0.98\,c$.
We turn to the outflow rate of GRS1915+105. In our model the outflow of relativistic mass is given by (4.15). One can see from (4.10)-(4.12) that the flow of rest-mass is approximately given by:

$$\dot{M}_0 \approx \dot{M} \cdot \frac{\alpha}{\gamma}. \tag{5.78}$$

Hence, we modify (4.15) by:

$$\begin{aligned} |\dot{M}_{0,w}| &\approx \frac{\alpha}{\gamma_w} \cdot 2\pi\sqrt{\Delta} H_w \rho_w \gamma_w v_w^r & (5.79)\\ \Rightarrow \dot{\mathcal{M}}_0 &= \frac{\alpha}{\gamma_w}\dot{\mathcal{M}} = 2\frac{|\dot{M}_{0,w}|}{\dot{M}_d}, & (5.80) \end{aligned}$$

where the factor of 2 in (5.80) accounts for the fact that the ejections are two-sided. $|\dot{\mathcal{M}}_0(r_{tr}) \cdot \dot{M}_d|$ corresponds to the amount of rest-mass per unit coordinate time that exits the TL above and below the accretion disk and contributes to the detected ejecta.
Mirabel et al. (1998) derived a minimum mass of $M_{cl} = 10^{19} g$ for the plasma clouds provided that they consist of equal numbers of electrons and protons. The ejection events last for $\approx 10\,min$. Taking into account that two clouds are ejected in opposite directions, this corresponds to $2\,\dot{M}_{cl} \approx 3.3 \cdot 10^{16} g\, s^{-1}$ or $\approx 3\%$ of the accretion rate ($\dot{M}_d \approx 1.1 \cdot 10^{18} g\, s^{-1}$, see Belloni et al., 1997b). From Table 5.2 we can see that the outflow rate, consistent with observation, ranges from $5.3-8.6\%$ corresponding to a mass of $1.7-2.8 \cdot 10^{19} g$ for the clouds. This is in good agreement with the order of magnitude estimate based on observational data.

We summarize the results of this section as follows:

$$\begin{array}{rcccl} 0.9930 & \le & a & \le & 0.9982 \\ 3.5\,r_g & \le & r_{tr} & \le & 14.5\,r_g \\ 5.3\% & \le & \dot{\mathcal{M}}_0 & \le & 8.6\% \end{array} \tag{5.81}$$

The proceeding in this section and the results we have obtained show that the model fits to observational data and allows for estimates that fall in the correct order of magnitude.

It should be noted that the steady jets of GRS1915+105 would have been the ideal object for an application of the model. These are expected to occur during the long periods where the source remains solely in state C. Unfortunately there is not enough observational data on steady jets, so we had to settle for the mini ejections during flaring states. The latter occur on timescales of $10\,min$ which is much longer than any relevant time scale in the TL ($t_{dyn}, t_{adv}, t_{amp}, t_{diss}$). As a consequence, the stationarity approximation is still valid during the mini ejections.

Summary and Conclusions

In this diploma thesis a new model for the formation and acceleration of ultra-relativistic jets has been presented, in which black hole-disk-jet interactions within the context of general relativity and in combination with the two-temperature plasma-description are taken into account.
In order to make the reader familiar with the physics of accretion, the Newtonian MHD equations and the standard α-disk model have been introduced. Subsequently the model has been derived from the GRMHD equations governing stationary, axisymmetric flows. The self-consistency of the model has been verified and the results visualized. It has been found that the geometrical thinness of the transition layer is not necessarily given for all parameter values which puts restrictions on the validity of the model. Further it was found that electrons and ions have indeed very different temperatures in the transition layer which justifies the two temperature description. This was even found to be valid when the flow in the transition layer is not tenuous.
Thereafter the model has been applied to the μQuasar GRS1915+105. Observational data and interpretation of the light curves have put restrictions on the free parameters of the model. According to the model, the black hole in GRS1915+105 has been found to be nearly in maximal rotation ($a \geq 0.9930$). Further, the predicted outflow rate in the transition layer yields the right order of magnitude for the mass of the ejecta.
For several decades the formation and acceleration of jets has been among the great unresolved problems in astrophysics. The model presented in this work appears to be the answer to many questions concerned with astrophysical jets. Its application to GRS1915+105 has shown that it is capable of reproducing observational data and is thus a serious candidate to explain the formation of jets around compact objects. The model allows for a deeper understanding of the subject and its future application might yield even further insights.

In the future we intend to modify the model to include time-dependent and sophisticated radiative magnetohydrodynamic effects, relevant for studying the very fast quasi-periodic oscillations considered to be connected to the accretion of matter as it crosses the event horizon of accreting black holes or as it shocks the surface of neutron stars. However, regarding the complexity of the problem a pure analytical treatment seems inappropriate and numerical assistance will be needed. Simulations of this kind have been performed by e.g. Hujeirat and Camenzind (2000b); Hujeirat et al. (2002) and have led to the formulation of the TDAT model which in turn led to the formulation of this model. The large variety of time scales in accretion flows around compact objects is a great obstacle for standard GRMHD codes, though. The implicit solver GR-I-RMHD (see e.g. Hujeirat et al., 2008, 2009) is certainly the optimal solver for this purpose, due to its remarkable robustness and unconditional numerical stability in addition to its capability of dealing with multi-temperature and dissipative plasmas.

Appendix A

Auxiliary Functions of the relativistic Standard Disk

We quote the auxiliary functions that we used in Section 5.2. They were defined by Novikov and Thorne (1973); Page and Thorne (1974) as:

$$\mathcal{A}_{NT} = 1 + \frac{a^2}{y^4} + \frac{2a^2}{y^6} \tag{A.1}$$

$$\mathcal{B}_{NT} = 1 + \frac{a}{y^3} \tag{A.2}$$

$$\mathcal{C}_{NT} = 1 - \frac{3}{y^2} + \frac{2a}{y^3} \tag{A.3}$$

$$\mathcal{D}_{NT} = 1 - \frac{2}{y} + \frac{a^2}{y^2} \tag{A.4}$$

$$\mathcal{E}_{NT} = 1 + \frac{4a^2}{y^2} - \frac{4a^2}{y^3} + \frac{3a^4}{y^4} \tag{A.5}$$

$$\begin{aligned} \mathcal{Q}_{NT} = \; & \frac{\mathcal{B}_{NT}}{\mathcal{C}_{NT}{}^{\frac{1}{2}} y} \cdot \left(y - y_{ms} + \frac{3}{2} \log \frac{y}{y_{ms}} - \frac{3(y-a)^2}{y_1(y_1-y_2)(y_1-y_3)} \cdot \right. \\ & \cdot \log \frac{y-y_1}{y_{ms}-y_1} - \frac{3(y_2-a)^2}{y_2(y_2-y_1)(y_2-y_3)} \log \frac{y-y_2}{y_{ms}-y_2} - \\ & \left. - \frac{3(y_3-a)^2}{y_3(y_3-y_1)(y_3-y_2)} \log \frac{y-y_3}{y_{ms}-y_3} \right), \end{aligned} \tag{A.6}$$

where a is the non-dimensional Kerr-parameter and

$$y = \sqrt{\frac{r}{r_g}} \tag{A.7}$$

$$y_{ms} = \sqrt{\frac{r_{ms}}{r_g}} \tag{A.8}$$

$$y_1 = 2\cos\left(\frac{1}{3}\arccos(a) - \frac{\pi}{3}\right) \tag{A.9}$$

$$y_2 = 2\cos\left(\frac{1}{3}\arccos(a) + \frac{\pi}{3}\right) \tag{A.10}$$

$$y_3 = -2\cos\left(\frac{1}{3}\arccos(a)\right). \tag{A.11}$$

r_{ms} and r_g correspond to the radius of the marginally stable orbit and the gravitational radius, respectively. y_1, y_2, y_3 are the roots of the equation

$$y^3 - 3y + 2a = 0. \tag{A.12}$$

Appendix B

Additional Data for GRS1915+105

We present further results for a, r_{tr} and $\mathcal{M}_{0,tr}$ that satisfy $E_w = E_{cl}$. Here we have taken the bulk velocity of the ejecta to be $0.94, 0.96$ and $0.98\,c$, respectively. See Section 5.2 for details.

r_{tr}/r_g	a	$\mathcal{M}_{0,tr}$ in %	r_{tr}/r_g	a	$\mathcal{M}_{0,tr}$ in %
3	0.9990	2.4	14.5	0.9948	6.1
3.5	0.9986	2.9	17	0.9945	6.2
4	0.9983	3.3	20	0.9941	6.4
4.5	0.9979	3.7	30	0.9935	6.7
5	0.9976	3.9	40	0.9931	6.8
6.25	0.9970	4.5	50	0.9928	6.9
7.5	0.9964	4.9	60	0.9926	7.0
8.75	0.9960	5.2	70	0.9925	7.0
10	0.9957	5.5	80	0.9924	7.0
12	0.9952	5.8	90	0.9923	7.0

Table B.1: a and $\mathcal{M}_{0,tr}$ for $v_{bulk} = 0.94\,c$.

r_{tr}/r_g	a	$\mathcal{M}_{0,tr}$ in %	r_{tr}/r_g	a	$\mathcal{M}_{0,tr}$ in %
3	0.9993	1.9	14.5	0.9966	4.6
3.5	0.9991	2.3	17	0.9963	4.8
4	0.9988	2.6	20	0.9961	4.9
4.5	0.9986	2.9	30	0.9957	5.1
5	0.9984	3.1	40	0.9955	5.2
6.25	0.9980	3.5	50	0.9953	5.2
7.5	0.9976	3.8	60	0.9952	5.2
8.75	0.9973	4.1	70	0.9952	5.2
10	0.9971	4.3	80	0.9951	5.2
12	0.9968	4.5	90	0.9950	5.2

Table B.2: a and $\mathcal{M}_{0,tr}$ for $v_{bulk} = 0.96\,c$.

r_{tr}/r_g	a	$\mathcal{M}_{0,tr}$ in %	r_{tr}/r_g	a	$\mathcal{M}_{0,tr}$ in %
3	0.9997	1.3	14.5	0.9983	2.9
3.5	0.9995	1.5	17	0.9982	3.0
4	0.9994	1.7	20	0.9981	3.0
4.5	0.9993	1.9	30	0.9979	3.1
5	0.9992	2.0	40	0.9978	3.1
6.25	0.9990	2.3	50	0.9978	3.1
7.5	0.9988	2.5	60	0.9977	3.1
8.75	0.9987	2.6	70	0.9977	3.1
10	0.9985	2.7	80	0.9977	3.1
12	0.9984	2.8	90	0.9977	3.1

Table B.3: a and $\mathcal{M}_{0,tr}$ for $v_{bulk} = 0.98\,c$.

Appendix C

Synchrotron Emission

Relativistic jets are usually detected by their radio emission which is generally interpreted as synchrotron radiation. This indicates the importance of magnetic fields in the physics of the formation, collimation and propagation of jets. Synchrotron emission is the main cooling process of the electrons in our model. Hence, it is useful to have some basic knowledge about it. Here we give just a very short review (see e.g. Novikov and Thorne, 1973, for a more detailed treatment).
Consider an electron in motion relative to an external magnetic field. The four-acceleration is given by the Lorentz force per mass:

$$(a^\nu) = \begin{pmatrix} a^t \\ \vec{a} \end{pmatrix} = \frac{d^2}{d\tau^2} \begin{pmatrix} ct \\ \vec{x} \end{pmatrix} = \begin{pmatrix} 0 \\ -\frac{e}{m_e}\gamma\frac{d\vec{x}}{dt} \times \vec{B} \end{pmatrix} = -\frac{e}{m_e}\left(\dot{x}_\mu F^{\mu\nu}\right), \tag{C.1}$$

where $e, m_e, \tau, \gamma = dt/d\tau = \sqrt{1 - \vec{v}^2/c^2}^{-1}$ are the proton charge, electron mass, proper time and Lorentz factor, respectively. The zeroth component of the four-acceleration equals zero since there are no electric fields involved. One obtains the radiated power by deriving the electromagnetic field of a moved charge then setting:

$$dP = \vec{R}^2 \vec{n}\vec{S} d\Omega, \tag{C.2}$$

where $S^i = T^{ti} = F^{i\rho}F^t{}_\rho$ is the Poynting vector, $\vec{R}$ the distance vector from the particle to the observer and $\vec{n} = \vec{R}/|\vec{R}|$. The leading term is the Lorentz-invariant expression (Novikov and Thorne, 1973):

$$P = \frac{2}{3}\frac{\alpha\hbar}{c^2} a_\mu a^\mu, \tag{C.3}$$

where $\alpha = e^2/(4\pi\varepsilon_0\hbar c)$ is the fine structure constant. In this case the radiated power becomes:

$$P = \frac{8\pi}{3}\frac{\alpha^2\hbar^2}{\mu_0 c}\left(\gamma\frac{v_\perp}{c}\right)^2 \frac{B^2}{{m_e}^2} = 1.59 \cdot 10^{-7} erg\, s^{-1} \cdot \gamma^2 \left(\frac{v_\perp}{c}\right)^2 B^2, \tag{C.4}$$

where $v_\perp$ is the velocity component perpendicular to B. One will be interested in the radiated power per mass or emissivity ϵ:

$$\epsilon = \frac{f_e}{m_p} \langle P \rangle , \tag{C.5}$$

where f_e and m_p correspond to the fraction of unbound electrons to baryons and the proton mass, respectively. $\langle (\cdot) \rangle$ denotes the Maxwell-Boltzmann average. It is defined by:

$$\langle (\cdot) \rangle = \frac{\int d^3p \, (\cdot) \, e^{-E/kT}}{\int d^3p \, e^{-E/kT}}. \tag{C.6}$$

In the nonrelativistic limit and in the ultrarelativistic limit, we obtain

$$\epsilon \;=\; 8\pi \frac{\alpha^2 \hbar^2}{\mu_0 c} \frac{f_e}{m_p} \frac{kT}{m_e c^2} \frac{B^2}{{m_e}^2} = 4.80 \cdot 10^{-7} \, erg \, s^{-1} \, g^{-1} \cdot f_e T B^2 \tag{C.7}$$

$$\epsilon \;=\; 32\pi \frac{\alpha^2 \hbar^2}{\mu_0 c} \frac{f_e}{m_p} \left(\frac{kT}{m_e c^2} \right)^2 \frac{B^2}{{m_e}^2} = 3.24 \cdot 10^{4} \, erg \, s^{-1} \, g^{-1} \cdot f_e {T_{10}}^2 B^2, \tag{C.8}$$

respectively, where $T_{10} = T/10^{10}K$. In the nonrelativistic case, cyclotron radiation, the spectrum is ideally monochromatic. In reality, though, it will be smeared around a maximum at the cyclotron frequency:

$$\nu_{cyc} = \frac{eB}{2\pi m_e} = 2.79 \cdot 10^{10} Hz \cdot B. \tag{C.9}$$

In the ultrarelativistic limit, synchrotron radiation, the spectrum is rather broad and peaks at:

$$\nu_{peak} \approx 4 \frac{eB}{m_e} \left(\frac{kT}{m_e c^2} \right)^2 = 2.00 \cdot 10^{12} Hz \cdot {T_{10}}^2 B. \tag{C.10}$$

List of Figures

List of Tables

Bibliography

S. A. Balbus and J. F. Hawley. A powerful local shear instability in weakly magnetized disks. I - Linear analysis. II - Nonlinear evolution. *ApJ*, 376:214–233, July 1991. doi: 10.1086/170270.

T. Belloni, M. Mendez, A. R. King, M. van der Klis, and J. van Paradijs. An Unstable Central Disk in the Superluminal Black Hole X-Ray Binary GRS 1915+105. *ApJ*, 479:L145+, April 1997a. doi: 10.1086/310595.

T. Belloni, M. Mendez, A. R. King, M. van der Klis, and J. van Paradijs. A Unified Model for the Spectral Variability in GRS 1915+105. *ApJ*, 488:L109+, October 1997b. doi: 10.1086/310944.

T. Belloni, M. Klein-Wolt, M. Méndez, M. van der Klis, and J. van Paradijs. A model-independent analysis of the variability of GRS 1915+105. *A&A*, 355: 271–290, March 2000.

R. D. Blandford and M. C. Begelman. On the fate of gas accreting at a low rate on to a black hole. *MNRAS*, 303:L1–L5, February 1999. doi: 10.1046/j.1365-8711.1999.02358.x.

R. D. Blandford and A. Konigl. Relativistic jets as compact radio sources. *ApJ*, 232:34–48, August 1979. doi: 10.1086/157262.

R. D. Blandford and D. G. Payne. Hydromagnetic flows from accretion discs and the production of radio jets. *MNRAS*, 199:883–903, June 1982.

R. D. Blandford and R. L. Znajek. Electromagnetic extraction of energy from Kerr black holes. *MNRAS*, 179:433–456, May 1977.

C. J. Burrows, K. R. Stapelfeldt, A. M. Watson, J. E. Krist, G. E. Ballester, J. T. Clarke, D. Crisp, J. S. Gallagher, III, R. E. Griffiths, J. J. Hester, J. G. Hoessel, J. A. Holtzman, J. R. Mould, P. A. Scowen, J. T. Trauger, and J. A. Westphal. Hubble Space Telescope Observations of the Disk and Jet of HH 30. *ApJ*, 473:437–+, December 1996. doi: 10.1086/178156.

M. Camenzind. *Compact objects in astrophysics : white dwarfs, neutron stars, and black holes.* 2007.

M. Camenzind and A. Mueller. Relativistic emission lines from accreting black holes. The effect of disk truncation on line profiles. *A&A*, 413:861–878, January 2004. doi: 10.1051/0004-6361:20031522.

H. D. Curtis. Descriptions of 762 Nebulae and Clusters Photographed with the Crossley Reflector. *Publications of Lick Observatory*, 13:9–42, 1918.

V. Dhawan, I. F. Mirabel, and L. F. Rodríguez. AU-Scale Synchrotron Jets and Superluminal Ejecta in GRS 1915+105. *ApJ*, 543:373–385, November 2000. doi: 10.1086/317088.

R. P. Fender, S. T. Garrington, D. J. McKay, T. W. B. Muxlow, G. G. Pooley, R. E. Spencer, A. M. Stirling, and E. B. Waltman. MERLIN observations of relativistic ejections from GRS 1915+105. *MNRAS*, 304:865–876, April 1999. doi: 10.1046/j.1365-8711.1999.02364.x.

J. Frank, A. King, and D. Raine. *Accretion power in astrophysics.* 1992.

M. Gedalin. Linear waves in relativistic anisotropic magnetohydrodynamics. *Phys. Rev. E*, 47(6):4354–4357, Jun 1993. doi: 10.1103/PhysRevE.47.4354.

J. Greiner. GRS 1915+105. *ArXiv Astrophysics e-prints*, November 2001.

J. Greiner, E. H. Morgan, and R. A. Remillard. RXTE observations of GRS 1915+105. *ArXiv Astrophysics e-prints*, October 1996a.

J. Greiner, E. H. Morgan, and R. A. Remillard. Rossi X-Ray Timing Explorer Observations of GRS 1915+105. *ApJ*, 473:L107+, December 1996b. doi: 10.1086/310402.

B. A. Harmon, S. N. Zhang, C. A. Wilson, B. C. Rubin, G. J. Fishman, and W. S. Paciesas. BATSE observations of transient hard X-ray sources. In C. E. Fichtel, N. Gehrels, & J. P. Norris, editor, *American Institute of Physics Conference Series*, volume 304 of *American Institute of Physics Conference Series*, pages 210–219, 1994.

A. Hujeirat. Jet-formation in accreting black hole systems and in GRB. *ArXiv Astrophysics e-prints*, February 2003.

A. Hujeirat. A model for electromagnetic extraction of rotational energy and formation of accretion-powered jets in radio galaxies. *A&A*, 416:423–435, March 2004. doi: 10.1051/0004-6361:20034089.

A. Hujeirat and M. Camenzind. Truncated disks - advective tori; new solutions of accretion flows around black holes. *A&A*, 361:L53–L56, September 2000a.

A. Hujeirat and M. Camenzind. Truncated disks - advective tori solutions around BHs. I. The effects of conduction and enhanced Coulomb coupling. *A&A*, 362: L41–L44, October 2000b.

A. Hujeirat, M. Camenzind, and M. Livio. Ion-dominated plasma and the origin of jets in quasars. *A&A*, 394:L9–L13, October 2002. doi: 10.1051/0004-6361: 20021282.

A. Hujeirat, M. Livio, M. Camenzind, and A. Burkert. A model for the jet-disk connection in BH accreting systems. *A&A*, 408:415–430, September 2003. doi: 10.1051/0004-6361:20031040.

A. Hujeirat, M. Camenzind, and B. W. Keil. An implicit numerical algorithm for solving the general relativistic hydrodynamical equations around accreting compact objects. *New Astronomy*, 13:436–450, August 2008. doi: 10.1016/j. newast.2007.12.004.

A. A. Hujeirat, B. W. Keil, and P. P. Hilscher. An implicit advection scheme for modeling relativistic shocks with high Lorentz factors. *ArXiv e-prints*, March 2009.

R. S. Klessen. Script Theoretical Astrophysics. 2008. URL `http://www.ita.uni-heidelberg.de/research/klessen/people/klessen/lectures/past_semesters.shtml`.

M. Livio. Astrophysical jets: a phenomenological examination of acceleration and collimation. *Phys. Rep.*, 311:225–245, April 1999. doi: 10.1016/S0370-1573(98) 00102-1.

M. Livio, G. I. Ogilvie, and J. E. Pringle. Extracting Energy from Black Holes: The Relative Importance of the Blandford-Znajek Mechanism. *ApJ*, 512:100–104, February 1999. doi: 10.1086/306777.

M. Livio, J. E. Pringle, and A. R. King. The Disk-Jet Connection in Microquasars and Active Galactic Nuclei. *ApJ*, 593:184–188, August 2003. doi: 10.1086/375872.

D. L. Meier. Ohm's Law in the Fast Lane: General Relativistic Charge Dynamics. *ApJ*, 605:340–349, April 2004. doi: 10.1086/382201.

I. F. Mirabel and L. F. Rodríguez. A superluminal source in the Galaxy. *Nature*, 371:46–48, September 1994. doi: 10.1038/371046a0.

I. F. Mirabel and L. F. Rodríguez. Sources of Relativistic Jets in the Galaxy. *ARA&A*, 37:409–443, 1999. doi: 10.1146/annurev.astro.37.1.409.

I. F. Mirabel, V. Dhawan, S. Chaty, L. F. Rodriguez, J. Marti, C. R. Robinson, J. Swank, and T. Geballe. Accretion instabilities and jet formation in GRS 1915+105. *A&A*, 330:L9–L12, February 1998.

C. W. Misner, K. S. Thorne, and J. A. Wheeler. *Gravitation*. 1973.

E. H. Morgan, R. A. Remillard, and J. Greiner. RXTE Observations of QPOs in the Black Hole Candidate GRS 1915+105. *ApJ*, 482:993–+, June 1997. doi: 10.1086/304191.

R. Narayan and I. Yi. Advection-dominated accretion: Self-similarity and bipolar outflows. *ApJ*, 444:231–243, May 1995. doi: 10.1086/175599.

I. D. Novikov and K. S. Thorne. Astrophysics of black holes. In *Black Holes (Les Astres Occlus)*, pages 343–450, 1973.

G. I. Ogilvie and M. Livio. Launching of Jets and the Vertical Structure of Accretion Disks. *ApJ*, 553:158–173, May 2001. doi: 10.1086/320637.

D. N. Page and K. S. Thorne. Disk-Accretion onto a Black Hole. Time-Averaged Structure of Accretion Disk. *ApJ*, 191:499–506, July 1974. doi: 10.1086/152990.

J. C. B. Papaloizou and J. E. Pringle. On the narrowness of transition fronts in accretion discs. *MNRAS*, 217:387–390, November 1985.

A. Rau and J. Greiner. Comptonization and reflection of X-ray radiation and the X-ray-radio correlation in the chi -states of GRS 1915+105. *A&A*, 397: 711–722, January 2003. doi: 10.1051/0004-6361:20021079.

I. Robson. *Active galactic nuclei*. 1996.

L. F. Rodríguez and I. F. Mirabel. Repeated Relativistic Ejections in GRS 1915+105. *ApJ*, 511:398–404, January 1999. doi: 10.1086/306642.

B. J. Sams, A. Eckart, and R. Sunyaev. Near-infrared jets in the Galactic micro-quasar GRS1915+105. *Nature*, 382:47–49, July 1996. doi: 10.1038/382047a0.

N. I. Shakura and R. A. Sunyaev. Black holes in binary systems. Observational appearance. *A&A*, 24:337–355, 1973.

F. Shu, J. Najita, E. Ostriker, F. Wilkin, S. Ruden, and S. Lizano. Magneto-centrifugally driven flows from young stars and disks. 1: A generalized model. *ApJ*, 429:781–796, July 1994. doi: 10.1086/174363.

K. S. Thorne. Disk-Accretion onto a Black Hole. II. Evolution of the Hole. *ApJ*, 191:507–520, July 1974. doi: 10.1086/152991.

A. Unsöld and B. Baschek. *Der neue Kosmos. Einführung in die Astronomie und Astrophysik*. 2002.

J.-H. Woo and C. M. Urry. Active Galactic Nucleus Black Hole Masses and Bolometric Luminosities. *ApJ*, 579:530–544, November 2002. doi: 10.1086/342878.

F. Yuan, S. Markoff, and H. Falcke. A Jet-ADAF model for Sgr A*. *A&A*, 383:854–863, March 2002. doi: 10.1051/0004-6361:20011709.

S. N. Zhang, W. Cui, and W. Chen. Black Hole Spin in X-Ray Binaries: Observational Consequences. *ApJ*, 482:L155+, June 1997. doi: 10.1086/310705.

Erklärung:

Ich versichere, dass ich diese Arbeit selbständig verfasst und keine anderen als die angegebenen Quellen und Hilfsmittel benutzt habe.

Heidelberg, July 11, 2010

....
(Unterschrift)